



COHERENT LIGHT-MATTER INTERACTIONS WITH POTASSIUM ATOMS

by

Andreas Lampis

A thesis submitted to
The University of Birmingham
for the degree of
DOCTOR OF PHILOSOPHY

Midlands Ultracold Atom Research Centre
University of Birmingham
School of Physics and Astronomy
College of Engineering and Physical Sciences

September 2017

UNIVERSITY OF
BIRMINGHAM

University of Birmingham Research Archive

e-theses repository

This unpublished thesis/dissertation is copyright of the author and/or third parties. The intellectual property rights of the author or third parties in respect of this work are as defined by The Copyright Designs and Patents Act 1988 or as modified by any successor legislation.

Any use made of information contained in this thesis/dissertation must be in accordance with that legislation and must be properly acknowledged. Further distribution or reproduction in any format is prohibited without the permission of the copyright holder.

Abstract

This thesis presents experimental work undertaken towards realising a system composed of magneto-optically-trapped potassium-39 atoms (^{39}K MOT) enclosed in a ring cavity. The length of the cavity is 9.51(5) cm and consequently its volume is big compared to cavities used for cavity quantum electrodynamics experiments, operating in the single-atom regime. As such, in order to enter a regime where the light-matter interactions are strong, thousands of atoms have to collectively interact with the mode of the cavity. We achieve strong interactions with potassium atoms for the first time, after $4.36(3) \times 10^4$ atoms were overlapped with the cavity mode. The signature of our system lying in the collective strong coupling regime was the observation of the splitting and avoided crossing of the normal modes, revealing a coupling strength constant $G = 2\pi \times 19.1(1.6)$ MHz.

The thesis also discusses the application of the electromagnetically-induced transparency (EIT) technique to control the group index of refraction (n_g) of atomic ensembles. We firstly apply EIT, in the Λ configuration, in a heated vapour cell of potassium. This helped us to better understand the underlying fundamentals of the technique, before ultimately applying it in the (main) cold atoms experiment. Deeply sub-natural EIT features have been achieved, for which we calculate n_g as high as 6330(160). Furthermore, by performing a novel measurement of the circular dichroism (and thus birefringence), we observed greater anisotropy when the weak probe and strong coupling beams, which participate in the formation of the EIT system, have $\text{lin}||\text{lin}$ rather than $\text{lin}\perp\text{lin}$ polarisation.

By optimising the temperature and optical depth of the ^{39}K MOT, EIT investigations were made possible with the cold atoms. While a splitting of the absorption line was observed at high coupling beam powers, no EIT resonances were observed when the coupling power was reduced. Our measurements imply that the EIT signal is compromised by decoherence factors, such as the inhomogeneity of the magnetic field across the atomic cloud. Eliminating decoherence and achieving EIT in the strongly interacting atom-cavity system will enable studies with applications in metrology and sensing.

Acknowledgements

Many people have contributed to making this four-year experience of experimenting in the “skinny” lab even more exciting. The first person I would like to thank is Jon Goldwin, for giving me the opportunity to work in his “ring cavity” team, for his excellent supervision and guidance, and for always having his door open for questions and advice.

A very special thank you should also go to my labmate and friend Rob (Dr. Robert Culver now), who has been a true role model for me. Rob has restlessly worked to build this experiment and has been there for me whenever I had a physics or English related question. Even after graduating, he has very kindly provided feedback on my thesis. Rob, I wish you the best in the future.

Balázs, I hope you enjoy your final year as a PhD student. Time flies and very soon you will also be writing your thesis. Graeme, I am confident that together with Balázs, you will make the experiment work and generate new and fascinating results. I would also like to thank you both for providing feedback on my thesis.

Komal and Lawrence, already three years since you have left the experiment and I can assure you that all your hard work has not been for nothing. The experiment is still alive!

Also, to the rest of the people in the Cold Atoms group, I would like to say that it was a pleasure getting to know you all. Thank you for making this experience even more fantastic.

Last, and by no means least, I would like to thank my parents for their love and support since the first day I was born, and Lelia who has stood by me after difficult days in the lab without complaining and always trying to cheer me up by cooking a delicious dinner and planning our next holidays together.

To my family

Contents

Abstract	i
Acknowledgements	ii
1 Introduction	1
1.1 Outline	6
2 Theory	8
2.1 Atoms enclosed in optical cavities	8
2.1.1 Jaynes-Cummings model for a closed system	8
2.1.2 Jaynes-Cummings model for an open system	12
2.1.3 Probing the cavity	14
2.1.4 Cooperativity	16
2.1.5 Collective strong coupling regime	17
2.2 Controlling the group index of refraction of atomic media	19
2.2.1 Velocities of light, refractive index and susceptibility	19
2.2.2 Electromagnetically induced transparency in three-level atoms	22
2.2.3 Electromagnetically induced transparency in an atom-cavity system	31

3	Experimental apparatus	35
3.1	Vacuum	36
3.2	Laser systems	38
3.2.1	Atom cooling and trapping	39
3.2.2	Probing the atom-cavity system	42
3.3	Ring cavity	46
3.3.1	Design and assembly	46
3.3.2	Parameters	48
3.4	Magnetic field	52
3.4.1	2D-MOT field	52
3.4.2	3D-MOT field	53
4	Electromagnetically induced transparency in an atomic vapour	57
4.1	EIT in potassium	58
4.2	Experimental setup	59
4.3	Transparency linewidth, absorption coefficient and group index	61
4.4	Magneto-optical anisotropy	67
4.4.1	Theory model	74
4.5	Discussion and conclusion	77
5	Magneto-optically trapping ^{39}K	78
5.1	Magneto-optical trap	78
5.1.1	Historical notes	79
5.1.2	Doppler cooling–optical molasses	79
5.1.3	Confining the atoms	82

5.1.4	Cold cloud of potassium atoms	84
5.2	Determining the atomic cloud parameters	86
5.2.1	Temperature	86
5.2.2	Atom number and optical depth	89
5.3	Cloud optimisations	90
5.3.1	Temperature	91
5.3.2	Atom number and optical depth	98
5.4	Conclusion	102
6	Strong light-matter interactions	103
6.1	Experimental procedure	103
6.2	Parameters	105
6.3	Results	106
6.4	Discussion and conclusion	107
7	Towards controllable dispersion with cold in-cavity atoms	110
7.1	Setting the scene	110
7.2	Probing the cold cloud of atoms	111
7.2.1	Experimental details	111
7.2.2	Results and discussion	114
7.3	Getting to EIT with cold in-cavity atoms	118
8	Conclusions and outlook	120
A	Derivations	123
A.1	Unitary transformation	124

A.2 Schrödinger equation in the rotating basis	125
B Calculations	126
B.1 Transit-time broadening	126
B.2 Number density	127
Bibliography	127

List of Tables

3.1	Measured cavity parameters at 770.1 nm. Letters f and c in the parentheses stand for flat and curved mirrors, respectively. The indicated mode volume is for the TEM ₀₀ mode and the linewidth specified here is for s-polarised light. All errors are standard deviations.	49
-----	--	----

List of Figures

1.1	A simple illustration showing the basic components of the experiment, i.e. the ring cavity, the cold atomic cloud, the probe and the coupling beams. The cavity mode is not to scale and the direction of propagation of the probe field has not been specified. Also, the angle of the coupling beam with respect to the cavity mode is arbitrarily chosen here.	5
2.1	Combining the bare atom with the empty cavity. a) Shows the energy levels of the bare atom and b) of the empty cavity. c) The combined system is shown, while the cavity-atom coupling is kept zero ($g = 0$). The degeneracy is only lifted due to the cavity-atom detuning δ (<0 here). d) Here, $\delta = 0$ and $g > 0$. The states are non-degenerate and split by $2g\sqrt{n}$	13
2.2	Theory plots generated by using the transmission equation 2.21 with parameters $g, \gamma, \kappa=2\pi\times(10, 3, 1)$ MHz. a) Cavity transmission for a number of cavity-atom detunings. Spectra have been shifted vertically for clarity. b) By generating many spectra similar to those shown in a), and tracking the centre frequencies of the peaks, the avoided crossing of the normal modes is plotted.	15

- 2.3 Atom number effect on the normal-mode splitting. The spectra are for $\delta = 0$, and were generated by using equation 2.21 and replacing g by G . For the five spectra shown (purple, blue, red, cyan and green), the parameters are: $g, \gamma, \kappa = 2\pi \times (0.1, 3, 1)$ MHz and $N = 0, 200, 500, 1000, 10000$ (respectively). 18
- 2.4 Energy level diagram for the EIT Λ system under consideration. 24
- 2.5 Reduced susceptibility plotted for various values of Ω_c , using equation 2.70. The parameters here for the three curves are $(\gamma_{31}, \gamma_{21}, \Delta_c) = (2\pi \times 3 \text{ MHz}, \gamma_{31}/1000, 0)$ and $\Omega_c = (0.5, 1, 2) \times \gamma_{31}$, for the blue, red and purple curve respectively. a) Imaginary part of susceptibility is shown. Near resonance, this goes to zero, meaning there is no absorption. b) Real part of susceptibility. The positive slope around zero frequency gets less steep as Ω_c is being increased. 30
- 2.6 Reduced susceptibility, plotted for various γ_{21} , using equation 2.70. The parameters here for the three curves are $(\gamma_{31}, \Omega_c, \Delta_c) = (2\pi \times 3 \text{ MHz}, 1 \times \gamma_{31}, 0)$ and $\gamma_{21} = (0.01, 0.5, 2) \times \gamma_{31}$, for the blue, red and purple curve respectively. a) Imaginary part of susceptibility is shown. Near resonance, this goes to zero as long as γ_{31} is kept low. b) Real part of susceptibility. The positive slope around zero frequency gets less steep and even changes sign as γ_{21} is being increased. 31
- 2.7 Normalised cavity transmission. The parameters here are $(G, \kappa, \gamma_{13}) = 2\pi \times (10, 1, 3)$ MHz, and $(\xi, \gamma_{23}) = (\kappa, \gamma_{13})/1000$. For the green curve, $\gamma_{21}, \Omega_c = 0$. For the purple, blue and red curves, $\Omega_c = 2\pi \times 10$ MHz, and $\gamma_{21} = 2\pi \times (0.0, 0.1, 0.5)$ MHz, respectively. The cavity transmission without atoms is in grey. An increase in the normal-mode splitting when $\Omega_c > 0$ is noticeable. Figure a) is same as b), just for a different detuning range. 34

- 3.1 A CAD drawing of the vacuum system as viewed from the side, with its different parts and the coils we use to make our 2D- and 3D-MOT, shown. 37
- 3.2 The MOT laser system. a) Saturated absorption spectroscopy on the D₂ potassium line, indicating the approximate frequency of the different beams involved in the atom cooling and trapping system. The repump-push frequencies should approximately be identical; they have only been shifted in frequency for better visualisation of the system. The frequency splitting between $F = 1 \rightarrow F' = 0, 1, 2$ and $F = 2 \rightarrow F' = 1, 2, 3$ corresponds to the ground-state hyperfine splitting and is 461.7 MHz. The transmission dip at the centre of the spectrum corresponds to the crossover between the ground states. The locking sequence is described in the text. b) An overview of the laser system responsible for making the MOTs. The colour coding used here does not relate to a). Most of the optics and other components have been omitted here. Numbers in circles represent locks feeding back to the lasers. M: mirror; (N)PBS: (non-)polarising beam splitter; BB: beam block; AOM: acousto-optic modulator; (B)PD: (balanced) photodetector; TA: tapered amplifier; RP: repump; CL: cooling; QWP: quarter-wave plate; PB: push beam; MIDL: magnetically-induced dichroism; BOL: beat offset lock. 40

- 3.3 The atom-cavity system. a) Saturated absorption spectroscopy on the D_1 potassium line, indicating the frequencies associated with the potassium laser. Note that in comparison to the D_2 line spectroscopy, here the different transitions are easier to identify. b) The parts that compose the atom-cavity probing laser system are presented. Note that the colour coding used here does not relate to a). Dichroic filters, which are used to separate the two wavelengths at different places, have been omitted as well as most of the other optical components of the system. All the AOMs except from AOM₃ are in a double-pass configuration. M: mirror; PBS: polarising beam splitter; AOM: acousto-optic modulator; (A)PD: (avalanche) photodiode; FMS: frequency modulation spectroscopy; PDH: Pound-Drever-Hall; FP_{cav}: Fabry-Pérot cavity. 43
- 3.4 Photograph of the ring cavity under vacuum from a MOT beam window. The tube connecting the 2D-MOT chamber with the science chamber is visible on the right. 46
- 3.5 The ring cavity assembly. a) The cavity frame with all mirrors glued on it. The hole in the frame which allows the atoms to enter the cavity mode is also visible. b) The 45° tilting block. c) Zooming in on the flex mount with the piezo and ceramics that isolate it from the frame on the focus. d) The fully assembled cavity on the mounting flange. Note how the piezo wires are clamped and connected to the electrical feedthrough. 47
- 3.6 Example cavity transmission spectrum. Cavity transmission is in blue, and a Lorentzian fit to it is in red. The fit reveals $\kappa = 0.92(2)$ MHz where the number in the parenthesis is the standard error from the fit. The fit assumes that the two sidebands are at the same absolute frequency from the central cavity transmission peak. The modulation frequency here is 17.273 MHz. 51

- 3.7 Cavity ring-down spectrum. The normalised cavity transmission curve is in blue, and the fit to the curve in red. Light begins to shut-off at $0.4 \mu\text{s}$ 52
- 3.8 Photograph of the elongated MOT ($\sim 5:1$ aspect ratio) inside the old-generation cavity. Scattered MOT light from the top-bottom viewports blurs the photo. Bottom viewport is labelled. 54
- 3.9 Coils' shut-off effect on the cavity. Cavity transmission and probe frequency ramp are in blue and red, respectively. The cavity is "locked" during the measurement. a) Current runs through the coils during the probe frequency scan. b) Coils are completely shut off when the probe frequency scan starts. Their shut-off is linear and takes $150 \mu\text{s}$. By the end of the probe scan, the coils are switched on again. c) Same events as in b), different timescale. Mechanical disturbances in the cavity remain for a long time after the coils are completely off. 55
- 4.1 a) Simplified energy level diagram of the D_1 hyperfine transitions of ^{39}K used in this experiment. The coupling beam field E_c (red) is detuned by Δ from the $F' = 2$ excited state manifold, and the probe (E_p , blue) is detuned by Δ_p from Raman resonance. The $F' = 1$ state here has been omitted for clarity and the ground state hyperfine splitting is taken from . b) Saturated absorption spectrum i.e. with no coupling beam present. The Doppler profile and transitions that take place in a) are shown. Furthermore, the partially resolved features that are visible include the excited state crossover resonances whereas the dips in the transmitted signal, indicating increased absorption, are due to ground state crossovers. c) The experimental layout, which is described in detail in the text. M: mirror; HWP: half-wave plate, QWP: quarter-wave plate; PBS: polarising beam splitter; AOM: acousto-optic modulator; BB: beam block; PMF: polarisation-maintaining fibre; PD: photodiode. 58

- 4.2 Doppler shift effect on the detunings of the probe (Δ_p) and the coupling beam (Δ_c). In a) the two beams are counter-propagating and the beams' frequencies are shifted by a different amount. Hence, not all the velocity classes of atoms contribute to the resulting EIT signal. b) The probe and coupling beams co-propagate, and their Doppler shifts cancel. Atoms from all different velocity classes do contribute to the EIT signal in this case. Similar explanation has been given by 60
- 4.3 a) Example EIT feature, showing the fractional transmission through the cell at a temperature of 74 °C. The coupling (probe) beam power is at 700 (50) μ W at the entrance of the cell. Data are shown in blue and the red curve shows a Lorentzian fit, which gives a HWHM of $2\pi \times 76.9$ kHz. b) EIT linewidth (HWHM) for varying coupling beam power. Points are fits from the data such as in a) and averaged over six traces for each power. For the red (blue) data, the heaters were turned off (on) during the measurement. The straight lines are a fit to equation 4.1. The fit gives a dephasing rate of $2\pi \times 43(1)$ kHz and $2\pi \times 64(2)$ kHz for the red and blue data, respectively. Error bars here show standard deviations. 62
- 4.4 Determination of the group index from a transmission spectrum. a) Fractional transmission spectrum $T(\omega_p)$ for coupling (probe) power of 300 (50) μ W and a cell temperature of 84 °C. b) Real (blue) and imaginary (red) parts of susceptibility, obtained from spectrum a) and as described in the text. c) The group index of refraction n_g of the gas as obtained by the numerical derivative of $[1 + \chi(\omega_p)]^{1/2}$. The analysis for these conditions gives a peak group index of 6330(160), averaged over three spectra. 64

- 4.5 Absorption and group index. a) Fractional transmission spectra $T(\omega_p)$ for coupling (probe) power of 300 (50) μW and a cell temperature of 84 $^\circ\text{C}$. The background absorption coefficient is varied by coarse tuning of the laser. The linewidth of the three example EIT features are $2\pi \times (86, 88, 62)$ kHz and the amplitude (16, 3, 8) %, for the traces A, B and C, respectively. b) The effect of optical depth on the group index. For each different cell temperature, the group index is measured by varying the detuning Δ_c . This leads to varying background probe absorption (i.e. just outside the EIT resonance). The upper branches correspond to probing on the blue sides of the Doppler profile near the $F_p \rightarrow F'$ transition, and the bottom halves on the red side near $F_c \rightarrow F'$. The black dashed line shows the linear dependence expected for simple EIT. 66
- 4.6 Effect of the added longitudinal magnetic field. a) The EIT resonance is split into three components. The central one is always centred at zero probe detuning ($\Delta_p = 0$) and the side peaks shift with effective magnetic moments of ± 1 Bohr magneton. Spectra have been shifted vertically for clarity. b) Left (red) and right (blue) peaks' centre frequency plotted with respect to the added magnetic field. 67
- 4.7 The width of the central and side EIT peaks as a function of the added longitudinal magnetic field. The central peak (purple) gets narrower as the field is being increased while the left (red) and right (blue) side peaks get broader due to the inhomogeneous field produced by the solenoid. Error bars here represent standard deviations. 68
- 4.8 EIT signals for the $\text{lin}\parallel\text{lin}$ (blue) and $\text{lin}\perp\text{lin}$ (red) configurations for different applied magnetic fields. 69

- 4.9 Simplified schematic for heterodyne measurements of optical anisotropy. The quarter-wave plate (QWP) and polarising beam splitter (PBS) act together as a circularly polarising beam splitter according to equation 4.4. The probe (E_p) and coupling (E_c) beam components interfere at the fast photodiodes A and B, and the resulting beat notes are used as inputs to a gain/phase detecting circuit (EVAL) as described in the text. 71
- 4.10 Heterodyne spectra of magneto-optically induced anisotropy. Red (blue) traces show the results for $\text{lin}\|\text{lin}$ ($\text{lin}\perp\text{lin}$) polarisations. The figures show the differential absorption coefficient $\Delta\alpha$, the phase difference $\Delta\phi$ (obtained by Hilbert transformation of $\Delta\alpha$), and the group index difference Δn_g (obtained by numerical differentiation of $\Delta\phi$ and then smoothed with the *sgolayfilt* filter in Matlab) as a function of the probe detuning. 73
- 4.11 Theoretical spectra as calculated by using equation 4.14, and 4.17. Parameters are $\Delta_c = 0$, $\Omega_c = 2\pi \times 10$ MHz, $\gamma_{21} = 2\pi \times 0.18$ MHz, and $\mathcal{N} = 1.5 \times 10^{11} \text{ cm}^{-3}$ (for our temperature we expect $\mathcal{N} = 1.65 \times 10^{11} \text{ cm}^{-3}$ – see Appendix B.2). 76
- 5.1 Doppler cooling force acting on atoms of different velocity classes. Dotted lines (blue and red) represent the force by each one of the counterpropagating beams involved in the interaction. Purple solid line is the total force, given by equation 5.2, for $\epsilon = 2$, $\delta = -\Gamma$ 81

- 5.2 Simple illustration of the operating mechanism of a MOT with an atom with $F = 0$ and $F' = 1$ states. Here, ω_0 represents the unshifted resonant frequency of the atomic transition and ω_L stands for the frequency of the laser. The magnetic field is position dependent and varies linearly with the distance from the centre of the trap. The σ^\pm beams are absorbed and scattered by atoms at a rate which depends on their detuning ($\omega_0 - \omega_L$), which side of x they are, and their distance from the centre of the trap (and their intensity). The Zeeman shifts shown here at either side of x are for the same absolute distance from the centre of the trap ($x = 0$). 83
- 5.3 Energy level diagram showing the D_2 line of ^{39}K . The two laser beams, cooling and repump, required for efficient optical cooling of potassium are shown in blue and red colour, respectively. The cooling beam was detuned from resonance by $\Delta_C = -27$ MHz and the repump beam by $\Delta_R = -18$ MHz. The detunings were specifically chosen in order to optimise the atom number in the trap. 85
- 5.4 MOT images taken at multiple times, t . Here, t is successively increased from a) \rightarrow h). For a) $t = 0.2$ ms and for h) $t = 1.5$ ms. 88
- 5.5 Typical time-of-flight measurement (without temperature optimisation). By fitting the data using equation 5.4, the temperature along the x and y axes were determined, giving $T_x = 1.49(12)$ mK and $T_y = 1.30(8)$ mK, respectively. Points here represent single shots and errors are just standard errors from the fits. 88
- 5.6 Simple schematic of the cooling procedure and the different parameters that can be varied in order to achieve a colder atomic cloud. 92

- 5.7 Scattering force versus atomic velocity curves as calculated by [136]. The three sub-figures (1-3) correspond to the calculated curve for different detuning ranges. Specifically, the force for a detuning within range 1 ($\Delta_C/\Gamma = 0 \rightarrow -2.2$) provides Doppler and sub-Doppler cooling. For range 2 ($\Delta_C/\Gamma = -2.2 \rightarrow -3.2$) it provides sub-Doppler cooling, and for range 3 ($\Delta_C/\Gamma = -3.2 \rightarrow -3.5$) it provides heating. 94
- 5.8 MOT temperature versus cooling detuning, Δ_C . Blue circles represent measurements of the cloud temperature using the TOF technique, whereas red circles represent the fraction of atoms left in the atomic cloud at the end of the cooling stage. Horizontal dashed black straight line indicates the Doppler limited temperature for ^{39}K . The figure has been split in a) and b) because of the big difference in the scale of the temperature axis between the two sub-figures, and also in order to give emphasis on the events happening in range 1-3. a) Shows how temperature and atomic fraction vary for Δ_C covering the frequency range between $F' = 2$ to $F' = 0$. b) Same measurement, for when Δ_C is somewhere between $F' = 3$ and $F' = 2$. The three ranges shown in Figure 5.7 are also indicated by dashed vertical lines and different colour coding. The temperature of the cloud is initially above the Doppler temperature in range 1 and becomes sub-Doppler as enters range 2. In range 3, the cloud completely disappears. 95
- 5.9 Total MOT beams' peak intensity effect on temperature and atomic fraction (deduced by single TOF measurements) of the cloud after the cooling stage. Dashed line indicates the Doppler temperature. 96
- 5.10 Temperature of the atomic cloud (deduced by single TOF measurements) as a function of the cooling stage time. Dashed line shows the Doppler temperature. 97

- 5.11 Typical time-of-flight measurement, after a cooling stage period of 2 ms. For this measurement, the total MOT peak intensity was halved to 15 mW/cm^2 , and $\Delta_C/\Gamma \sim -2$. The temperature along x was found to be $130(5) \mu\text{K}$ and $116(10) \mu\text{K}$ along the y -axis. Points here represent single shots and errors are just standard errors from the fits. 98
- 5.12 Ion pump current reading for various dispenser currents. 100
- 5.13 3D-MOT atom number for different temperatures of the 2D-MOT chamber. Error bars represent standard deviations from eight different MOT pictures. 101
- 6.1 Photograph of the cavity and the MOT. By optimising the overlap between the cavity mode and the MOT it was possible to observe large normal-mode splitting. 104
- 6.2 Normal-mode splitting for various effective atom number and $\delta = 0$. Spectra here are averaged 32 times before storage. a) Cavity transmission spectrum when no atoms are in the cavity mode. Red line is a Lorentzian fit to the data. b-d) The normal-mode of the cavity splits. Data are fitted to the transmission equation (equation 2.21, with g replaced by G), revealing $G = 2\pi \times [4.2(4), 6.9(1.3), 10.7(5.9)] \text{ MHz}$ for b), c) and d) respectively. Uncertainties here represent standard error from the fits. 106
- 6.3 Avoided crossing of the normal modes. a) Several transmission spectra are shown for increasing cavity-atom detunings. Actual and filtered data, and Lorentzian fits to the filtered data (*sgolayfilt* was used to smooth out the data), are in blue, cyan and red, respectively. b) Blue circles represent the normal-mode resonance frequencies whereas black curves are fits to equation 6.1, showing that $G = 2\pi \times 19.1(1.6) \text{ MHz}$. Number in brackets here represents standard error arising from fits to the data. Red circles show data without atoms. 108

7.1	<p>Λ sub-systems for different probe-coupling polarisation configurations. a) The probe and coupling beams both have π polarisation. b) The probe and coupling have π and σ_{\pm} polarisation, respectively; green(red) arrows indicate $\sigma_{+}(\sigma_{-})$ polarisation.</p>	114
7.2	<p>Absorption line splitting. a) Probe transmission spectra. As the coupling power increases from i) to v) a peak (or splitting of the absorption line) at zero probe detuning becomes more pronounced. Data are fitted using a function which is the sum of two Lorentzians. The square root of coupling power for spectra i), to v) is (0, 1.4, 2.0, 2.4, 2.8) $\text{mW}^{1/2}$, respectively. b) Absorption peaks' separation as a function of the square root of coupling power. Each blue circle represents the average of three fitted spectra, at a certain coupling power. Error bars here represent standard deviation. Dashed black line is a linear fit with intercept forced as 0 to the blue data giving a slope of 3.22(3) $\text{MHz}/\text{mW}^{1/2}$, where the number in the parenthesis is the standard error from the fit.</p>	115

Chapter 1

Introduction

This thesis presents studies of strong light-matter interaction, combined with steep dispersion, in a system composed of magneto-optically trapped potassium-39 atoms (^{39}K MOT) and a ring cavity. An overview of why these studies are important will be given with particular emphasis on the unique features of our experiment.

Enhancing light-matter interactions

In free space a single atom spontaneously emits individual photons with random phases, polarisations, and propagation directions, so that a vanishing fraction of the emission populates any single mode of the light field [1]. Absorption of a single photon can be imagined as time-reversed emission [2, 3], from which it is clear that one needs to create an incident light field exactly matching the (typically dipole) radiation pattern of a single mode in both the far and near fields [4, 5]. As experiments have shown this is not easily achievable [6], with the current state-of-the-art around 70 % absorption for single atoms and photons [7].

A couple of alternative strategies exist and can in fact significantly enhance light-matter interactions. First, one can consider enclosing atoms in optical cavities. This particular area of studies is called cavity quantum electrodynamics (cQED) and has found

numerous applications in many areas of physics [8], for instance in quantum information [9]. In cavities with small mode volume (V), the strength of the single atom-photon coupling (g), which determines the strength of the interactions, can be large because g is inversely proportional to \sqrt{V} [10, 11]. Furthermore, cavities enhance the effective interaction time by an amount which is proportional to the finesse. A second option to increase the interaction strength is to probe ensembles with very high atomic densities. For instance, one may use vapour cells, whose atomic density can be greatly increased by controlling their temperature.

The cQED experiment described in this thesis operates in a regime where the coherent single-atom single-photon interactions are one order of magnitude smaller than the rate at which photons escape from the cavity (determined by the cavity linewidth κ), and are also significantly smaller than the atomic decay rate ($\gamma \sim 3\kappa$). Fortunately, when atomic ensembles are placed in cavities, they act collectively and coherently, as Dicke's studies revealed [12]. This has the implication that when N atoms interact with the cavity mode, then $g \rightarrow g\sqrt{N}$, as Tavis and Cummings later proved [13]. Therefore, it is still possible to enter a regime in which the coherent interactions dominate over those causing decoherence, even when $g \ll \kappa, \gamma$. When this is the case, absorbed photons can be re-emitted into the cavity mode instead of irreversibly escaping into the environment. This cyclic process happens at the well-known Rabi frequency. In our experiment, we enter this regime once $N \gtrsim 1000$ are overlapped with the cavity mode (as will be shown in Chapter 6). This is called the collective strong coupling regime and its signature is the observation of normal-mode splitting in the cavity transmission spectrum of a weak probe laser.

Since its first experimental demonstration [14] in 1989, collective strong coupling has drawn the attention of the scientific community as it has enabled studies of long range atom-atom interactions [15, 16], the control of the linewidth of cavities [17], cQED with multiple cavity modes [18] and atomic states [19], to name but a few.

Controlling the group index of refraction of atomic media in free-space and inside a cavity

Further to the strong light-matter coupling, our experiment also aims to control the group index of refraction of the cold atomic medium inside the cavity. In order to do that, the electromagnetically induced transparency (EIT) technique is employed.

Electromagnetically induced transparency occurs when two mutually coherent light beams, commonly referred to as the probe and coupling beams, simultaneously address different transitions in three-level atoms. The beams share a common state, and usually the probe is much weaker (below atomic saturation) than the coupling. With the coupling beam turned-off, a dip in the transmission spectrum is observed when the probe propagates through an atomic medium. However, once the coupling beam is turned on, the properties of the medium are modified, the probe transmission is attained back and a sharp feature with sub-natural linewidth appears in the spectrum. The attained transparency is not a very interesting or useful phenomenon on its own; the probe also sees the medium as transparent when it is not resonant with it. Most importantly, the EIT transparency is accompanied with sharp dispersion, which can significantly modify the group index of refraction n_g of the atoms and lead to the generation of slow ($n_g > 1$) or even fast ($n_g < 1$) light as the group velocity $v_g = c_0/n_g$ (where c_0 is the vacuum speed of light)¹.

EIT has been investigated in hot vapours, cold atoms, and has also been applied in experiments with cavities. The first EIT demonstration was in a strontium vapour [22], in 1990. Since then, light propagating with a $v_g = 17$ m/s has been observed in a Bose-Einstein condensate experiment [23], and $v_g = 8$ m/s in an antirelaxation coated atomic vapour cell [24]. EIT has also been investigated in single-atom cavity experiments [25, 26],

¹This thesis mainly considers cases that the probe and coupling beams are near resonance, in which case $n_g > 1$. But, it should be noted that fast light (i.e. when $n_g < 1$) is also of interest for us, in the long-term, and for this reason we discuss it in the introduction. Fast light can be generated if we employ the EIT technique with the coupling beam detuned from resonance [20], or by using a Raman gain doublet [21].

for applications relevant to quantum information [27]. Experiments working in the fast light regime have also been demonstrated, for example the one described in [28], where $v_g < -300$ m/s was measured in a caesium vapour cell. Slow and fast light have found a wide range of applications, for example in interferometry [29]. Slow light was proved to narrow the linewidth of cavities [30], and enhance the sensitivity of spectrometers [31]². Fast light, on the other hand, has been predicted to enhance the sensitivity of rotation sensors, such as laser gyroscopes [33].

In our experiment we have investigated EIT in a heated potassium vapour cell, and as will be shown in Chapter 4, narrow transparency features were generated, with a calculated $n_g > 6000$. The next short-term goal of our experiment is to control the properties of the cold in-cavity atom cloud using EIT and examine the photon lifetime in the cavity. Further investigations will involve not only the modification of n_g but also the addition of gain to the system and investigation for example of the aforementioned sensitivity enhancement prediction of a ring laser gyroscope.

The ring cavity

We enclose the ³⁹K MOT in a ring (right-angled triangular) cavity, as shown in Figure 1.1. As can be understood, for a given mirror size, a cavity of this type cannot be made as short as a Fabry-Pérot cavity, and so will have a bigger mode volume. Therefore (since $g \propto 1/\sqrt{V}$), entering the strong coupling regime with a ring cavity is usually only possible when atomic ensembles are considered, as is the case for our experiment. At the same time, a ring cavity geometry offers the possibility to make a MOT inside the cavity, instead of, for example, firstly trapping the atoms above the cavity and then translating them inside the cavity mode using a 1D-optical lattice [34], or dropping the MOT above microtoroids (in this case the atoms interact with the evanescent field of the resonator) [35]. Furthermore, ring cavities support travelling waves and can be probed simultaneously

²An enhancement that should ideally be proportional to n_g but in practice is limited due to the interplay between absorption (gain) and n_g [32].

by opposite directions, meaning that counter-propagating wave modes can co-exist inside the cavity.

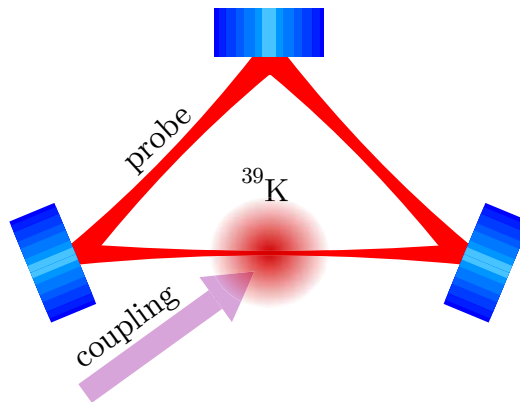


Figure 1.1: A simple illustration showing the basic components of the experiment, i.e. the ring cavity, the cold atomic cloud, the probe and the coupling beams. The cavity mode is not to scale and the direction of propagation of the probe field has not been specified. Also, the angle of the coupling beam with respect to the cavity mode is arbitrarily chosen here.

Ring cavities were proven to enhance the efficiency of atom-based quantum memories [36], and generate narrow spectral features when employed for studies with atomic media with controllable n_g (for example, EIT media) [37, 38]. Ring cavities can be used for the study and development of the aforementioned ultra-sensitive ring laser gyroscope [39–41]. Additionally, taking advantage of our ring cavity we could build the first bi-directional laser with a linewidth below the Schawlow-Townes limit [42], which until today has only been demonstrated in Fabry-Pérot cavities [43–46].

Potassium-39 atoms

Using ^{39}K is not the most common choice for a cold atom, cQED and/or EIT experiment. In fact, as it will be presented in the following chapters, we have been the first to demonstrate strong coupling between light and potassium [47] and one of a few experiments implementing the EIT technique in that species [48–50]. Therefore, as can be understood, studying a system with potassium atoms is already interesting on its own. Furthermore, potassium offers the possibility to create an isotopic Bose-Bose and Bose-Fermi mixture

[51] as ^{39}K (boson), ^{40}K (fermion) and ^{41}K (boson) are all stable. Lastly, since ^{39}K has relatively small hyperfine level splitting (Δ), it can also be used to study multilevel cQED, once $g\sqrt{N}$ becomes of the order of Δ [19, 52].

1.1 Outline

The thesis begins with the theory chapter (Chapter 2) that aims to familiarise the reader with the fundamentals of cQED and EIT. Then, it proceeds with Chapter 3 which describes the main components of the experiment, such as the vacuum system, the laser systems and the ring cavity. It also explains the reasons that led us to the particular cavity and vacuum design.

In Chapter 4, an EIT experiment in a heated potassium vapour cell is discussed. This experiment was done with an eye towards gaining enough experience on the EIT technique before ultimately applying it to the main, cold atoms experiment. The experiment generated very interesting results, such as a difference in the magneto-optical anisotropy of the EIT medium, depending on the relative polarisation of the probe and the coupling beams.

Chapter 5 is focused on the cold atoms part of the experiment. The ^{39}K MOT is discussed and optimisations related to the temperature, atom number and optical depth of the cloud are presented.

In Chapter 6, experimental results demonstrating that our atom-cavity system lies in the collective strong coupling regime are shown. Measurements implying that tens of thousands of atoms were overlapped with the mode of the ring cavity are presented.

Chapter 7 discusses work towards the implementation of the EIT technique in the cold in-cavity atoms. Results suggesting that decoherence is limiting the EIT signal are shown and improvements needed in order to achieve our goal are discussed.

The thesis closes with Chapter 8 which provides a summary of the overall work pre-

sented, and briefly discusses the next, short-term goal of the experiment.

Chapter 2

Theory

This chapter introduces the reader to the background theory necessary to understand light-atom interaction in optical cavities and explains how the electromagnetically induced transparency technique can be used in order to modify the group index of refraction of atomic media.

2.1 Atoms enclosed in optical cavities

In this section, a simple model for studying the interaction between light enclosed in a cavity and atoms will be provided. At first, a closed system will be considered and following this, the model will be extended to also include losses. An equation for the cavity transmission spectrum will be derived and the characterisation of the interaction strength will be discussed.

2.1.1 Jaynes-Cummings model for a closed system

In 1963, Jaynes and Cummings proposed a model explaining the dynamics of a system consisting of a stationary two-level atom coupled to a cavity with a single mode¹. At the

¹By single mode here we mean that only one of the resonant cavity modes is close to the atomic resonance [53]. This is justified in our experiment by the fact that the cavity longitudinal mode spacing

heart of the model, lies the Jaynes-Cummings (JC) Hamiltonian² [54]:

$$H_{JC} = H_C + H_A + H_I \quad , \quad (2.1)$$

where $H_{C,A,I}$ stand for the empty cavity, free atom, and cavity-atom interaction Hamiltonians, respectively.

Starting with the cavity³,

$$H_C = \hbar\omega_c P \quad , \quad (2.2)$$

where P stands for the photon number operator, related to the creation (a^\dagger) and annihilation (a) field operators by $P = a^\dagger a$. Applying these operators to a number (also known as Fock) state gives [55]:

$$P |n\rangle = n |n\rangle \quad (2.3a)$$

$$a^\dagger |n\rangle = \sqrt{n+1} |n+1\rangle \quad (2.3b)$$

$$a |n\rangle = \sqrt{n} |n-1\rangle \quad . \quad (2.3c)$$

The Hamiltonian for an atom with ground state $|g\rangle$ and excited state $|e\rangle$ can be expressed as [56]:

$$H_A = \frac{1}{2}\hbar\omega_a\sigma_z = \hbar\omega_a\sigma^+\sigma^- \quad , \quad (2.4)$$

where $\hbar\omega_a$ is the energy difference between $|g\rangle$ and $|e\rangle$, and $\sigma_z = [\sigma^+, \sigma^-]$ is the atomic state inversion operator. Furthermore, $\sigma^+ = |e\rangle\langle g|$ and $\sigma^- = |g\rangle\langle e|$ are the raising and lowering operators, respectively⁴.

H_I is written as [57]:

$$H_I = -\mathbf{d} \cdot \mathbf{E} \quad , \quad (2.5)$$

where \mathbf{d} is the dipole moment operator and \mathbf{E} the electric field operator for the cavity

is three orders of magnitude greater than the cavity and atomic linewidths, and two orders greater than any interaction/coupling strengths.

²Hats denoting operators have been skipped throughout the thesis for simplicity

³Zero-point energy equal to $\frac{1}{2}\hbar\omega_c$ is omitted here, as any other constant through the derivation of the Hamiltonian.

⁴In order to get from $\frac{1}{2}\hbar\omega_a\sigma_z$ to $\hbar\omega_a\sigma^+\sigma^-$, we have used the completeness of the basis relation (and omitted a factor of $-\frac{1}{2}\hbar\omega_a$).

mode under consideration.

The dipole operator can be written as,

$$\mathbf{d} = \mathbf{d}_{eg}\sigma^+ + \mathbf{d}_{ge}\sigma^- \quad , \quad (2.6)$$

where $\mathbf{d}_{eg} = \langle e | \mathbf{d} | g \rangle = \mathbf{d}_{ge}^*$, and $\mathbf{d}_{gg} = \mathbf{d}_{ee} = 0$, as the spherical symmetry of the atoms and parity considerations⁵ imply.

The electric field operator of a single mode cavity is of the following form,

$$\mathbf{E} = \mathbf{e} \sqrt{\frac{\hbar\omega_c}{2\epsilon_0 V}} \left(a e^{i(\mathbf{k}_c \cdot \mathbf{r} - \omega_c t)} + a^\dagger e^{-i(\mathbf{k}_c \cdot \mathbf{r} - \omega_c t)} \right) \quad (2.7)$$

$$= \mathbf{e} \sqrt{\frac{\hbar\omega_c}{2\epsilon_0 V}} \left(a e^{-i\omega_c t} + a^\dagger e^{i\omega_c t} \right) \quad , \quad (2.8)$$

with \mathbf{e} being the polarisation vector of the field, and ϵ_0 and V the vacuum permittivity and volume of the cavity mode, respectively. Additionally, \mathbf{k}_c is the wavevector of the cavity field and \mathbf{r} is the position vector. The field operator can be written in the equation 2.8 form since we are making use of the dipole approximation⁶.

Substituting equations 2.6 and 2.8 into 2.5, we arrive at,

$$H_I = -\hbar g (\sigma^+ + \sigma^-) (a e^{-i\omega_c t} + a^\dagger e^{i\omega_c t}) \quad . \quad (2.9)$$

Here, we have defined the cavity-atom interaction strength (also known as the coupling constant) $g = d \sqrt{\frac{\omega_c}{2\hbar\epsilon_0 V}}$, and $d = \langle e | \mathbf{d} \cdot \mathbf{e} | g \rangle$. We also have considered d to be real, without loss of generality.

By making a couple of unitary transformations ($H \rightarrow U^\dagger H U$, where $U^\dagger U = I$ and I is the identity matrix), the interaction Hamiltonian can be written in a more simplified form.

For the first transformation, we let $U = e^{-iH_A t/\hbar} = |e\rangle \langle e| e^{-i\omega_a t} + |g\rangle \langle g|$ (Appendix A.1

⁵ \mathbf{d} has odd parity. Thus, if the wavefunctions (which are parity eigenstates with parity $(-1)^l$ for angular momentum l) corresponding to the states under evaluation are the same, when $\langle e(g) | \mathbf{d} | e(g) \rangle$ is evaluated it results to zero.

⁶The dipole approximation assumes that the wavelength of the radiation interacting with the atom is much longer than the atom itself, hence the field is uniform across the atom. By comparing λ with r , where r is of the same order as the Bohr radius, we see that $\lambda \gg r$. Hence, $\mathbf{k}_c \cdot \mathbf{r} \ll 1$, and we can write \mathbf{E} in the form shown in equation 2.8.

shows how to get U in the latter form). From that it can be shown that,

$$H_I = -\hbar g(\sigma^+ a e^{-i\delta t} + \sigma^- a^\dagger e^{i\delta t}) \quad , \quad (2.10)$$

where $\delta = \omega_c - \omega_a$. In order to get H_I into this form, we have made the rotating-wave approximation [58]. More specifically, we have neglected the fast-evolving terms ($\omega_c + \omega_a$) and kept only the slow-evolving ones ($\omega_c - \omega_a$). Since for the case we are interested in, $\omega_c \approx \omega_a$, for the timescale of the near-resonant terms the effect of the rapidly oscillating terms can be assumed to average to zero. Note that not only our approximation can be justified mathematically but also has a physical meaning since we have dropped terms that do not conserve energy, i.e. $\sigma^+ a^\dagger$ and $\sigma^- a$. Specifically, the first term corresponds to an atom getting excited while a photon is emitted, and the second corresponds to an atom relaxing to its ground state while it absorbs a photon.

For the second transformation, we let $U = |e\rangle\langle e| e^{-i\delta t} + |g\rangle\langle g|$, and finally get our time-independent interaction Hamiltonian:

$$H_I = -\hbar g(\sigma^+ a + \sigma^- a^\dagger) \quad . \quad (2.11)$$

By substituting equations 2.2, 2.4 and 2.11 into equation 2.1, we arrive at the following version of the JC Hamiltonian:

$$H_{JC} = \hbar\omega_c a^\dagger a + \hbar\omega_a \sigma^+ \sigma^- - \hbar g(\sigma^+ a + \sigma^- a^\dagger) \quad . \quad (2.12)$$

For the doublet states $|g, n\rangle$ and $|e, n-1\rangle$, the JC Hamiltonian can be expressed in the following matrix form:

$$H_{JC} = \hbar \begin{bmatrix} n\omega_c & -g\sqrt{n} \\ -g\sqrt{n} & n\omega_c - \delta \end{bmatrix} \quad .$$

Then, following the method described in [59], the eigenvalues E_n^\pm and eigenstates $|\pm, n\rangle$

can be determined:

$$E_n^\pm = \hbar \left(n\omega_c - \frac{\delta}{2} \pm \sqrt{\frac{\delta^2 + 4g^2n}{4}} \right) \quad (2.13a)$$

$$|\pm, n\rangle = \begin{cases} \cos(\theta/2) |g, n\rangle + \sin(\theta/2) |e, n-1\rangle \\ -\sin(\theta/2) |g, n\rangle + \cos(\theta/2) |e, n-1\rangle \end{cases}, \quad (2.13b)$$

where $\theta = \tan^{-1} \left(\frac{2g\sqrt{n}}{\delta} \right)$.

It follows from equation 2.13a that $\Delta E_n = E_n^+ - E_n^- = \hbar\sqrt{4g^2n + \delta^2}$. For $\delta = 0$, when $g = 0$, the eigenstates are degenerate. But once $g > 0$, the eigenstates no longer have the same energy and they split. Note that the frequency by which the states split is the same as the frequency at which the exchange of excitation between the cavity and the atom happens [60]. For this reason $2g$ is commonly called the single photon-atom Rabi frequency. Figure 2.1 provides an illustration of this phenomenon which is called the normal-mode splitting and is a keystone of the field of cavity quantum electrodynamics (cQED).

2.1.2 Jaynes-Cummings model for an open system

An extension of the loss-free model described in the previous section will be provided here. Considering imperfectly reflecting mirrors and atoms with finite lifetime in a state, the new “effective” Hamiltonian can be written as,

$$H'_{JC} = \hbar\omega_c a^\dagger a + \hbar\omega_a \sigma^+ \sigma^- - \hbar g (\sigma^+ a + \sigma^- a^\dagger) - i\hbar\gamma \sigma^+ \sigma^- - i\hbar\kappa a^\dagger a, \quad (2.14)$$

where the half-width-half-maximum (HWHM) cavity (κ) and atomic (γ) linewidths, have been included in the equation. Note that H'_{JC} is non-Hermitian, and will therefore generally have complex eigenvalues whose real parts give the energies and imaginary parts the inverse lifetimes (or decay rates).

Using the same basis subset as in Section 2.1.1, the eigenvalues of the system are now

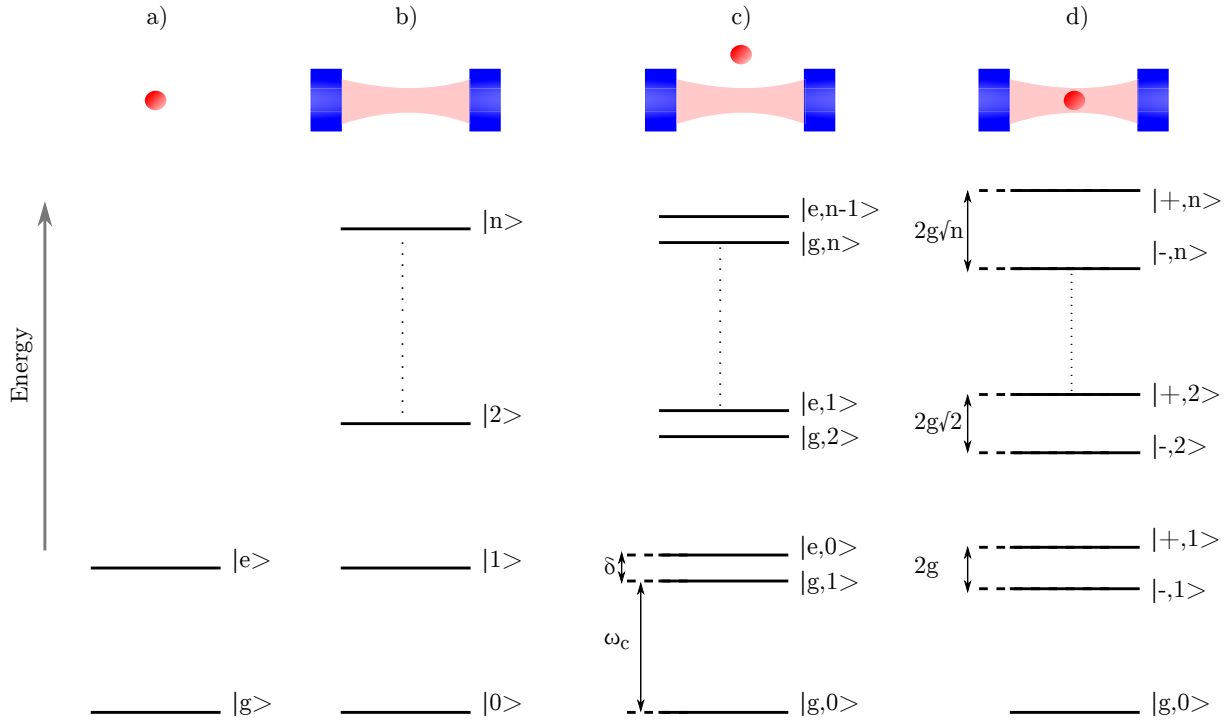


Figure 2.1: Combining the bare atom with the empty cavity. a) Shows the energy levels of the bare atom and b) of the empty cavity. c) The combined system is shown, while the cavity-atom coupling is kept zero ($g = 0$). The degeneracy is only lifted due to the cavity-atom detuning δ (<0 here). d) Here, $\delta = 0$ and $g > 0$. The states are non-degenerate and split by $2g\sqrt{n}$.

found to be,

$$\frac{2}{\hbar}(E_n^\pm)' = (2\omega_c n - \delta) - i[\kappa(2n - 1) + \gamma] \pm \sqrt{4g^2 n + [\delta + i(\gamma - \kappa)]^2} \quad . \quad (2.15)$$

By restricting ourselves to the case that $n = 1$ and $\delta = 0$,

$$\frac{2}{\hbar}(E_1^\pm)' = 2\omega_c - i(\kappa + \gamma) \pm \sqrt{4g^2 - (\gamma - \kappa)^2} \quad (2.16a)$$

$$\Delta E_1' = \hbar\sqrt{4g^2 - (\gamma - \kappa)^2} \quad . \quad (2.16b)$$

Thus, the eigenstates only split now when $4g^2 > (\gamma - \kappa)^2$ and the real part of equation 2.16b is greater than $\frac{\kappa + \gamma}{2}$. Generally, if $g \gg \frac{|\gamma - \kappa|}{2}$, our system is said to lie in the strong-coupling regime⁷. In this regime, the atom and the cavity have enough time

⁷It should be stressed, however, that this condition could lead to the incorrect conclusion that as long as the incoherent terms are equal then their magnitude is unimportant. In contrast, their magnitude determines whether it is possible to observe normal-mode splitting at all, since, in any case, $\sqrt{4g^2 - (\gamma - \kappa)^2}$, should also be greater than the peaks linewidth, $\frac{\kappa + \gamma}{2}$.

to exchange excitations before the loss mechanisms become important.

2.1.3 Probing the cavity

Now that we have introduced some way to put light in our cavity (mirrors have $<100\%$ reflectivity), we can study the dynamics of our system by probing the cavity and collecting the transmitted (or reflected) light. For this reason we now include in our Hamiltonian (H'_{JC}) a pumping term with frequency ω_p and rate ξ ,

$$H_P = -i\hbar\xi(ae^{i\omega_p t} - a^\dagger e^{-i\omega_p t}) \quad . \quad (2.17)$$

Transforming our Hamiltonian twice using a transformation of the form $U^\dagger H U - \zeta$ ($U = e^{-i\zeta t}$), where firstly we set $\zeta = \hbar\omega_p\sigma^+\sigma^-$ and then $\zeta = \hbar\omega_p a^\dagger a$, we can write our effective Hamiltonian in a new form, in a frame rotating with ω_p ,

$$H''_{JC} = \hbar\delta_c a^\dagger a + \hbar\delta_a \sigma^+\sigma^- - \hbar g(\sigma^+ a + \sigma^- a^\dagger) - i\hbar\gamma\sigma^+\sigma^- - i\hbar\kappa a^\dagger a - i\hbar\xi(a - a^\dagger) \quad , \quad (2.18)$$

where $\delta_{c(a)} = \omega_{c(a)} - \omega_p$.

In order to calculate the cavity transmission (T) we will follow the simple method outlined in [61]. Assuming the probe beam is weak (i.e. $\xi < \frac{\kappa+\gamma}{2} \ll g$), we can write the time-dependent state vector associated with our system as:

$$|\psi(t)\rangle = c_0 |g, 0\rangle + c_1(t) |g, 1\rangle + c_2(t) |e, 0\rangle \quad . \quad (2.19)$$

Due to the assumption of weak probing, we also assume negligible excitation, so that $|c_0| \approx 1 \gg |c_{1,2}|$ and take c_0 to be real without loss of generality. Substituting H''_{JC} and $|\psi(t)\rangle$ in the Schrödinger equation, gives:

$$i\dot{c}_1 = -gc_2 + (\delta_c - i\kappa)c_1 + i\xi \quad (2.20a)$$

$$i\dot{c}_2 = -gc_1 + (\delta_a - i\gamma)c_2 \quad . \quad (2.20b)$$

T is proportional to the intracavity photon number $\langle n \rangle$. This can be found once we calculate the probability of $|\psi\rangle$ being in the $|g, 1\rangle$ state. Looking for a steady-state solution

by letting $\dot{c}_1 = \dot{c}_2 = 0$, we find that

$$\frac{T}{T_0} = \left(\frac{\kappa}{\xi}\right)^2 \times \langle n \rangle = \frac{\kappa^2}{|(i\kappa - \delta_c) + g^2/(\delta_a - i\gamma)|^2} \quad , \quad (2.21)$$

where $T_0 = \left(\frac{\xi}{\kappa}\right)^2$ stands for the average photon number when $g, \delta_{c,a} = 0$.

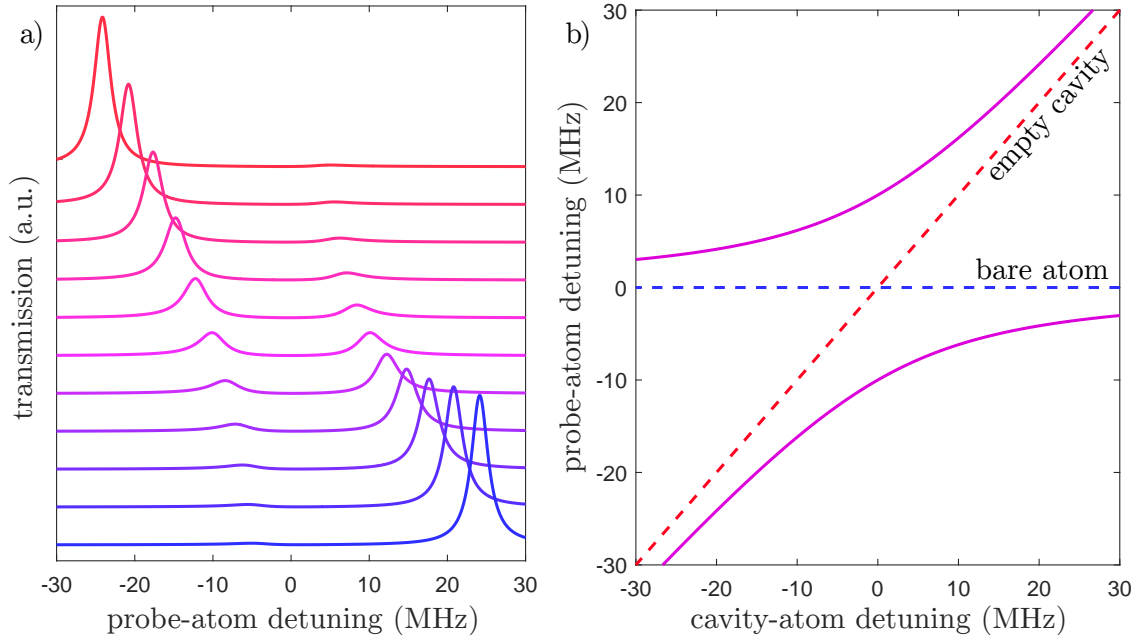


Figure 2.2: Theory plots generated by using the transmission equation 2.21 with parameters $g, \gamma, \kappa=2\pi \times (10, 3, 1)$ MHz. a) Cavity transmission for a number of cavity-atom detunings. Spectra have been shifted vertically for clarity. b) By generating many spectra similar to those shown in a), and tracking the centre frequencies of the peaks, the avoided crossing of the normal modes is plotted.

Using equation 2.21, cavity transmission can be plotted for different cavity-atom detunings, as shown in Figure 2.2a). For the parameters we have chosen, $g, \gamma, \kappa=2\pi \times (10, 3, 1)$ MHz, the states of the system coherently exchange excitation ($2g$) faster than the rate at which photons escape from the cavity mirrors (2κ) or an excited atom spontaneously returns to its ground state (2γ). By tracking the centre frequencies of the transmission peaks, the avoided crossing of the normal modes can be plotted, as shown in Figure 2.2b).

2.1.4 Cooperativity

Following the same methodology as previously, where the transmission equation 2.21 was derived, we will calculate the effect of weakly coupling an atom to a single mode cavity ($\kappa \gg g$) and from that define a dimensionless parameter known as the single-atom cooperativity (C).

We consider the effective Hamiltonian H'_{JC} (equation 2.14) and the same doublet as before ($|g, 1\rangle, |e, 0\rangle$). Our Schrödinger equations now read as:

$$i\dot{c}_1 = -gc_2 - i\kappa c_1 \quad (2.22a)$$

$$i\dot{c}_2 = -gc_1 - i\gamma c_2 \quad . \quad (2.22b)$$

We make the assumption that at $t = 0$, the atom is excited $|e, 0\rangle$. Since $\kappa \gg g$, at $t > 0$ the atom will just decay to $|g, 0\rangle$ and no oscillatory exchange of excitation between $|e, 0\rangle \leftrightarrow |g, 1\rangle$ will be observed. Hence, $\dot{c}_1 \approx 0$, which now leads to,

$$\dot{c}_2 = -c_2 \left(\gamma + \frac{g^2}{\kappa} \right) \quad \longrightarrow \quad c_2(t) = e^{-\left(\gamma + \frac{g^2}{\kappa}\right)t} = e^{-\gamma' t} \quad . \quad (2.23)$$

From this, one can draw the conclusion that the atomic decay rate (γ') has been modified by the presence of the cavity. This is exactly what Purcell had predicted [62]. Rate γ' is now the sum of the bare atom spontaneously emitting light into all possible non-cavity modes (γ) and the atom's coherent scattering rate into the cavity (γ_c),

$$\gamma' = \gamma + \gamma_c = \gamma + \frac{g^2}{\kappa} = \gamma(1 + C) \quad . \quad (2.24)$$

From this equation, we have also defined the single-atom cooperativity⁸ $C = \frac{g^2}{\kappa\gamma}$. This dimensionless term is of great significance for cQED as it provides a measure of how strong or weak the coherent interactions are, compared to the quantities that add decoherence to the system. But, we should be careful here. It is sometimes stated in the literature that if $C > 1$ in a system, then the system should also lie in the strong coupling regime.

⁸In many references as in [63, 64], C can be found to be half what we have defined here. The physical interpretation of the term is independent of this factor of two.

This, strictly speaking is not true, as pointed out by [63]. This is only the case when $\kappa \approx \gamma$. When $\kappa \lesssim \gamma$, $C > 1$ could also correspond to cases that the normal modes are not entirely resolved as the splitting might not exceed their width [65].

2.1.5 Collective strong coupling regime

Our discussion up to now has been limited to the single atom case. Tavis and Cummings (TC) provided an extension of the JC model by considering an atomic ensemble interacting with the single mode of a cavity [13]. The model is based on previous theory by Dicke who examined the behaviour of a gas consisting of two-level atoms when subjected to a radiation field. His findings revealed that atoms interacting with a cavity mode can act collectively and coherently, and no longer radiate independently [12].

After making the rotating wave approximation, the TC Hamiltonian can be written as [66]:

$$H_{TC} = \hbar \left[\omega_c a^\dagger a + \frac{1}{2} \omega_a S_z + g (a^\dagger S_- + a S_+) \right] \quad , \quad (2.25)$$

where $S_\pm = \sum_{i=1}^N S_\pm^{(i)}$ and $S_z = \sum_{i=1}^N S_z^{(i)}$ are the collective atomic operators for an ensemble of N two-level atoms with identical couplings g . Specifically, for the i^{th} atom, with ground state $|g_i\rangle$ and excited state $|e_i\rangle$, the operators are given by:

$$S_+^{(i)} = |e_i\rangle \langle g_i| \quad (2.26a)$$

$$S_-^{(i)} = |g_i\rangle \langle e_i| \quad (2.26b)$$

$$S_z^{(i)} = \left[S_+^{(i)}, S_-^{(i)} \right] \quad . \quad (2.26c)$$

Considering a weak probe beam (i.e. $n \ll N$), a solution for the eigenenergies of the system can be approximated [66],

$$E(n, j) \approx \hbar \left[\left(n - \frac{N}{2} \right) \omega_a + \frac{n\delta}{2} + j \sqrt{\delta^2 + 4g^2 N} \right] \quad , \quad (2.27)$$

where $0 \leq n \ll N$ and $-n/2 \leq j \leq n/2$, with j denoting which state of the multiplet we are in.

As can be seen from equation 2.27, the cavity-atom coupling constant g is now accompanied by \sqrt{N} . We will denote the new variable as G , where $G = g\sqrt{N}$, and refer to it as the collective coupling constant.

We should understand G to play the same role as g in the single atom case. Figure 2.3 illustrates how N can modify the cavity spectrum, from the point that no splitting is visible, to the point that very large splitting is apparent. The parameters chosen here are approximately identical to the ones that apply for our experiment. Since G is now what describes the coherent coupling between the atoms and the cavity, it can be understood that entering the strong coupling regime and achieving normal-mode splitting does not only depend on the cavity design. The regime in which the splitting can be observed in a multi-atom system is called the “collective strong coupling” regime and requires $G > \frac{|\gamma - \kappa|}{2}$.

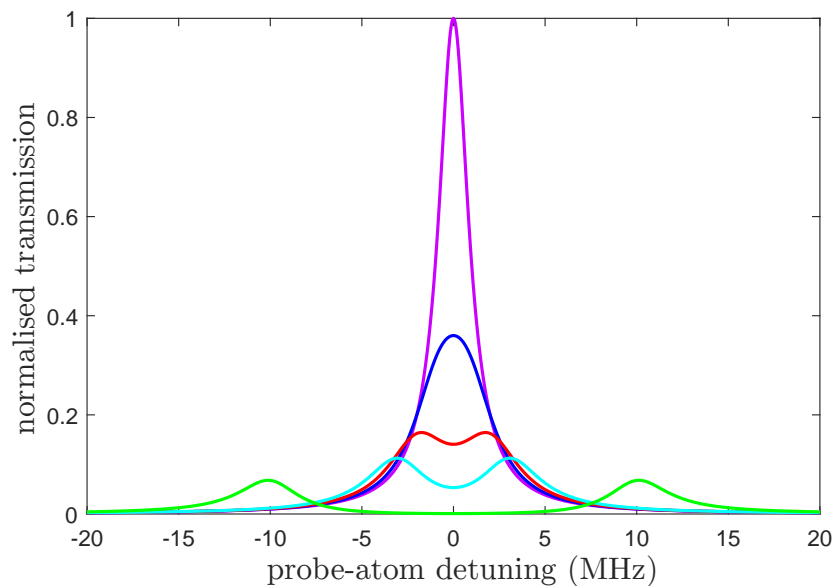


Figure 2.3: Atom number effect on the normal-mode splitting. The spectra are for $\delta = 0$, and were generated by using equation 2.21 and replacing g by G . For the five spectra shown (purple, blue, red, cyan and green), the parameters are: g , γ , $\kappa = 2\pi \times (0.1, 3, 1)$ MHz and $N = 0, 200, 500, 1000, 10000$ (respectively).

2.2 Controlling the group index of refraction of atomic media

As we have seen in the previous section, once a two-level atom is placed inside an optical cavity, its properties are modified. In fact, when this is the case, the atom and the cavity cannot be thought of as two separate entities anymore but as a new combined system instead. Here, we will extend our discussion further, by considering now three-level atoms inside the cavity and including an additional beam that will allow us to study how electromagnetically induced transparency (EIT) can modify the properties of the system.

This section begins with a short discussion about the velocities of light, the refractive index and susceptibility of atomic media. Then, in order to grasp the basics of the EIT theory, we derive the EIT Hamiltonian and susceptibility for a three-level atom system probed in free space, following a semi-classical approach. In the last part of this section, we integrate the EIT medium inside the cavity, and we investigate the properties of the strongly interacting atom-cavity system by following a fully quantum-mechanical treatment, which allows us to plot the transmission spectrum of the cavity.

2.2.1 Velocities of light, refractive index and susceptibility

Great care must be taken when referring to the “velocity of light”. As explained in [67], a number of different velocities of light can be defined, other than the well-known speed of light in vacuum (c_0), and their magnitude could differ by a lot when dispersive media (i.e. media with a refractive index n that depends on the probe frequency ω_p) are considered. For the purposes of this thesis, only two of these velocities are useful to define; the phase velocity (v_p) and the group velocity (v_g).

The electric field of a monochromatic plane wave (with wavenumber k and frequency

ω_p) travelling through space (z) and time can be expressed as [68]:

$$E(z, t) = E_0 e^{i(kz - \omega_p t)} \quad , \quad (2.28)$$

where $kz - \omega_p t$ is the phase (ϕ) of the wave and the velocity at which points with constant ϕ propagate is what we refer to as the phase velocity. If we make a transformation of the form $z \rightarrow z + dz$ and $t \rightarrow t + dt$ while keeping ϕ constant, then,

$$\phi = k(z + dz) - \omega_p(t + dt) = kz - \omega_p t \quad . \quad (2.29)$$

As we can see, $k dz = \omega_p dt$, and using this relationship we can write an expression for the phase velocity of the form:

$$v_p = \frac{dz}{dt} = \frac{\omega_p}{k} \quad . \quad (2.30)$$

The phase velocity is also known to be equal to c_0/n , where we should understand n to be the real part of the refractive index. In general, n could be a function of ω_p (and thus k also), and likewise $v_p = v_p(k)$.

In case we want to examine how fast a pulse of light (i.e. with many frequency components) propagates through a medium, then we need to understand that each frequency component has a different phase velocity. Therefore, if one wants to describe the velocity of the envelope of the pulse, phase velocity is not such a useful quantity anymore. The pulse of light can be written as [69],

$$E(z, t) = \frac{1}{2\pi} \int_{-\infty}^{\infty} \tilde{E}(k) e^{i(kz - \omega_p t)} dk \quad . \quad (2.31)$$

If we assume the dispersion to be linear, ignore second and third order terms (responsible for pulse spreading and distortion, respectively) and expand $\omega_p(k)$ to first order about k_0 (a centre wavenumber), then,

$$\omega_p(k) \approx \omega_0 + (k - k_0) \left. \frac{d\omega_p}{dk} \right|_{k_0} \quad , \quad (2.32)$$

where we have set $\omega_0 = \omega_p(k_0)$. From this we can define the group velocity as

$$v_g = \left. \frac{d\omega_p}{dk} \right|_{k_0} \quad . \quad (2.33)$$

By then substituting equation 2.32 into 2.31,

$$E(z, t) = \frac{1}{2\pi} e^{i(k_0 z - \omega_0 t)} \int_{-\infty}^{\infty} \tilde{E}(k) e^{i(k-k_0)(z-v_g t)} dk \quad , \quad (2.34)$$

and as can be seen, the pulse now has a space-time dependence of the following form:

$$E(z, t) = E(z - v_g t) \quad . \quad (2.35)$$

Therefore, the propagation velocity of the pulse is determined by v_g . However, we should note that the numerous frequency components that compose the pulse still travel at v_p .

In analogy to $n = c_0/v_p$, the group index of refraction n_g can be also be defined as:

$$n_g = \frac{c_0}{v_g} = n + \omega_p \frac{dn}{d\omega_p} \quad . \quad (2.36)$$

It is therefore intuitive to understand that by controlling the dispersion ($dn/d\omega_p$) of a medium, n_g can be made extremely large, or even negative. Group indices greater than or less than 1 lead to the generation of “slow” or “fast” light⁹, respectively, both with vast amount of applications¹⁰ (as discussed in Chapter 1). For this thesis we mainly restrict our discussion to cases that $n_g > 1$.

Before moving to the next section to discuss about EIT in three-level atoms it is necessary to introduce another very important quantity, the susceptibility, χ of a medium. In an isotropic, linear, homogeneous and dispersive medium, $\chi(\omega_p)$ is related to the polarisation (\mathbf{P}) of the medium and characterises its response to an applied electric field (\mathbf{E}) [71],

$$\mathbf{P} = \epsilon_0 \chi \mathbf{E} \quad , \quad (2.37)$$

where ϵ_0 is the electric permittivity of free space. Specifically, the phase shift accumulated by an electric field as it propagates through an atomic medium is related to the real part of susceptibility χ' which relates to the refractive index as $\chi' = n^2 - 1$. Furthermore,

⁹We should add a note here. Fast light media do not violate causality. It has been observed that the peak of a pulse exits a fast light medium before even entering it but in any case the information velocity remains constant and equal to c_0 [70].

¹⁰We mostly discuss about how different v_g can be from c_0 here, but it is worth stressing the fact that v_p is also not bound by c_0 .

the absorption of the electric field is characterised by the imaginary part of susceptibility χ'' , which can be expressed in relation to the absorption coefficient (α) as $\alpha = k\chi''$. For this thesis we will only consider linear media which obey causality and as such χ'' can be related with χ' via the Kramers-Kronig relations [69].

2.2.2 Electromagnetically induced transparency in three-level atoms

The application of EIT can drastically modify the properties of atomic media. This part of the thesis presents the underlying theory behind this technique by employing a simple three-level atomic medium (not inside a cavity).

A semi-classical approach has been followed here, where the atoms are treated fully quantum-mechanically and the fields are assumed to be classical vectors. The derivation partially follows [55, 72, 73] whereas many useful explanations were drawn from the review by Fleischhauer *et al.* [74]. This approach was preferred over a fully quantum mechanical one as it fully captures the essence of the EIT technique and can be more easily understood. However, we should note that a fully quantum mechanical approach exists and is based on quasiparticles called “dark-state polaritons” which basically are a superposition of atomic polarisation and photons [75].

The susceptibility χ of the EIT medium carries all the important information regarding the light propagation (through the medium), and following the strategy described below will allow us to derive an analytical expression for it.

We will consider a system that consists of many atoms, each one being in a non-specified state, and as such, it is sensible to use density operators (ρ) to describe it. The density operator is simply $\rho = \sum_i P_i |\psi_i\rangle \langle\psi_i|$, where P_i is the probability of the system being in the $|\psi_i\rangle$ state. The evolution of the system can be described by solving the master

equation (also called as the von Neumann equation) [76],

$$\dot{\rho} = -\frac{i}{\hbar}[H, \rho] \quad . \quad (2.38)$$

It is also known that the density of (electric) dipole moments in an atomic medium determines its polarisation [77],

$$\mathbf{P} = \mathcal{N}\langle \mathbf{d} \rangle \quad , \quad (2.39)$$

where \mathcal{N} is the atom number density and $\langle \mathbf{d} \rangle$ is the average dipole moment per atom. This expression can be written in a more useful form, permitting us to relate the polarisation to the dipole operator expectation value for the atomic medium being in the ρ mixed state [72],

$$\mathbf{P} = \mathcal{N}\text{Tr}(\mathbf{d}\rho) \quad , \quad (2.40)$$

where $\langle \mathbf{d} \rangle = \text{Tr}(\mathbf{d}\rho)$. Then, by comparing equation 2.37 (from the previous section) with 2.40, we will relate ρ with χ and accordingly study the properties of the EIT medium.

EIT Hamiltonian

The three-level atom we consider here has two stable ground states $|1\rangle$, $|2\rangle$ and an excited state $|3\rangle$, as shown in Figure 2.4. The states correspondingly have energy eigenvalues $\hbar\omega_{n=1, 2, 3}$. A probe field of amplitude \mathcal{E}_p , and optical frequency ω_p , and a coupling field (\mathcal{E}_c , ω_c), with $\mathcal{E}_c \gg \mathcal{E}_p$, address the $|1\rangle \leftrightarrow |3\rangle$ and $|2\rangle \leftrightarrow |3\rangle$ transitions, respectively, and form the EIT Λ system. The $|1\rangle \leftrightarrow |2\rangle$ transition is assumed to be dipole forbidden.

The EIT Hamiltonian in its most general form can be expressed as,

$$H_{EIT} = H_A + H_I \quad , \quad (2.41)$$

where H_A is the Hamiltonian of the free atom and H_I is the atom-light interaction Hamiltonian including both the probe and coupling fields.

H_A can be simply written as,

$$H_A = \hbar(\omega_1 |1\rangle \langle 1| + \omega_2 |2\rangle \langle 2| + \omega_3 |3\rangle \langle 3|) \quad . \quad (2.42)$$

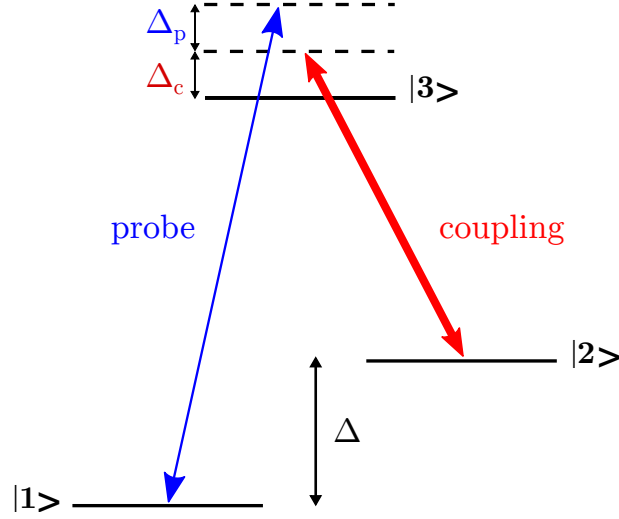


Figure 2.4: Energy level diagram for the EIT Λ system under consideration.

The interaction Hamiltonian is the same as in equation 2.5,

$$H_I = -\mathbf{d} \cdot \mathbf{E} \quad , \quad (2.43)$$

where \mathbf{d} is the dipole operator and \mathbf{E} is the total applied electric field. We should also recall that $\mathbf{d}_{\mu\nu} = \mathbf{d}_{\nu\mu}^* = \langle \mu | \mathbf{d} | \nu \rangle$ and that $\mathbf{d}_{\mu\mu} = \mathbf{d}_{\nu\nu} = 0$, as we only consider atoms with no permanent dipole moments (as in Section 2.1). Furthermore, as we have already assumed that $\mathbf{d}_{12} = \mathbf{d}_{21} = 0$, the interaction Hamiltonian can be expressed as following,

$$H_I = -\mathbf{E} \cdot (\mathbf{d}_{31} |3\rangle \langle 1| + \mathbf{d}_{13} |1\rangle \langle 3| + \mathbf{d}_{32} |3\rangle \langle 2| + \mathbf{d}_{23} |2\rangle \langle 3|) \quad , \quad (2.44)$$

where the classical vector field under consideration is of the following form:

$$\begin{aligned} \mathbf{E} &= \mathbf{E}_p \cos(\omega_p t - \mathbf{k}_p \cdot \mathbf{r}) + \mathbf{E}_c \cos(\omega_c t - \mathbf{k}_c \cdot \mathbf{r}) \\ &= \mathbf{E}_p \cos(\omega_p t) + \mathbf{E}_c \cos(\omega_c t) \\ &= \frac{1}{2} \mathbf{E}_p (e^{i\omega_p t} + e^{-i\omega_p t}) + \frac{1}{2} \mathbf{E}_c (e^{i\omega_c t} + e^{-i\omega_c t}) \quad . \end{aligned} \quad (2.45)$$

Here, $\mathbf{E}_p = \mathbf{e}_{p(c)} \mathcal{E}_{p(c)}$ with $\mathbf{e}_{p(c)}$ being the polarisation vector of the probe (coupling) field. Furthermore, $\mathbf{k}_{p(c)}$ and \mathbf{r} are the wave vector and the position vector, respectively. Getting the equation in the form written in the second line requires making use of the dipole approximation as in Section 2.1.

We then substitute equation 2.45 into 2.44 and make a unitary transformation of the

form $H \rightarrow U^\dagger H U$, $U = e^{iH_A t/\hbar} = |1\rangle\langle 1| e^{i\omega_1 t} + |2\rangle\langle 2| e^{i\omega_2 t} + |3\rangle\langle 3| e^{i\omega_3 t}$. Hence, the interaction Hamiltonian can be written as:

$$H_I = - \left(\frac{1}{2} \mathbf{E}_p (e^{i\omega_p t} + e^{-i\omega_p t}) + \frac{1}{2} \mathbf{E}_c (e^{i\omega_c t} + e^{-i\omega_c t}) \right) \cdot (\mathbf{d}_{31} e^{i\omega_{31} t} |3\rangle\langle 1| + \mathbf{d}_{32} e^{i\omega_{32} t} |3\rangle\langle 2| + \text{h.c.}) \quad , \quad (2.46)$$

where $\omega_{31} = \omega_3 - \omega_1$ and $\omega_{32} = \omega_3 - \omega_2$. By multiplying the terms of the equation, it follows that,

$$H_I = -\frac{1}{2} \mathbf{E}_p (\mathbf{d}_{31} e^{i(\omega_{31} - \omega_p)t} |3\rangle\langle 1|) - \frac{1}{2} \mathbf{E}_c (\mathbf{d}_{32} e^{i(\omega_{32} - \omega_c)t} |3\rangle\langle 2|) + \text{h.c.} \quad , \quad (2.47)$$

after making the rotating wave approximation and omitting terms oscillating rapidly such as $\omega_{31} + \omega_p$ and $\omega_{32} + \omega_c$, while keeping the slowly oscillating terms $\omega_{31} - \omega_p$ and $\omega_{32} - \omega_c$. This approximation is valid since we are considering a system where the coupling and probe beams are near (or on) resonance with the transitions they address.

Finally, by reversing the transformation we get the EIT Hamiltonian:

$$H_{EIT} = \hbar(\omega_1 |1\rangle\langle 1| + \omega_2 |2\rangle\langle 2| + \omega_3 |3\rangle\langle 3|) - \frac{\hbar}{2} (\Omega_p e^{-i\omega_p t} e^{-i\phi_p} |3\rangle\langle 1| + \Omega_c e^{-i\omega_c t} e^{-i\phi_c} |3\rangle\langle 2| + \text{h.c.}) \quad , \quad (2.48)$$

where $\Omega_{p(c)}$ is the Rabi frequency associated with the probe (coupling) beam,

$$\hbar\Omega_p = |\mathbf{d}_{31}| \mathcal{E}_p \quad \quad \hbar\Omega_c = |\mathbf{d}_{32}| \mathcal{E}_c \quad , \quad (2.49)$$

and $\phi_{p(c)}$ is the probe (coupling) beam's phase

$$\mathbf{d}_{31} \cdot \mathbf{e}_p = |\mathbf{d}_{31}| e^{-i\phi_p} \quad \quad \mathbf{d}_{32} \cdot \mathbf{e}_c = |\mathbf{d}_{32}| e^{-i\phi_c} \quad . \quad (2.50)$$

Rotating basis

The previous unitary transformation has been shown to be useful as it resulted to a more simplified form of the EIT Hamiltonian. Our next transformation will be made with an eye towards removing all the time-dependent terms, as well as the dipole moment operator phase.

For this transformation, we need to move to a new basis. We will relate this basis,

also referred to as the rotating basis, to the old basis by $|\tilde{n}\rangle = \tilde{U} |n\rangle$, where,

$$\tilde{U} = e^{-i(\omega_p t + \phi_p)} |1\rangle \langle 1| + e^{-i(\omega_c t + \phi_c)} |2\rangle \langle 2| + |3\rangle \langle 3| \quad . \quad (2.51)$$

The Schrödinger equation can be used in order to write the EIT Hamiltonian in the new basis (see Appendix A.2),

$$\tilde{H}_{EIT} = i\hbar \frac{\partial \tilde{U}}{\partial t} \tilde{U}^\dagger + \tilde{U} H_{EIT} \tilde{U}^\dagger \quad . \quad (2.52)$$

It follows that we can express the Hamiltonian that will be ultimately used in order to analyse the properties of the EIT system as:

$$\tilde{H}_{EIT} = \hbar((\omega_1 + \omega_p) |1\rangle \langle 1| + (\omega_2 + \omega_c) |2\rangle \langle 2| + \omega_3 |3\rangle \langle 3|) - \frac{\hbar}{2}(\Omega_p |3\rangle \langle 1| + \Omega_c |3\rangle \langle 2| + \text{h.c.}) \quad . \quad (2.53)$$

Density matrix

Now that we have derived the EIT Hamiltonian, we are interested in calculating the components of the EIT density matrix (in order to ultimately link them to χ as it has been described at the beginning of Section 2.2.2). For this we will use the (aforementioned) master equation [76],

$$\dot{\tilde{\rho}} = -\frac{i}{\hbar} [\tilde{H}_{EIT}, \tilde{\rho}] \quad (2.54)$$

and include “phenomenological” decay rates. Population decay from a specific state, for example $|\mu\rangle$, will be written as γ_μ . In our experiment we require the ground states $|1\rangle$ and $|2\rangle$ to be stable, and as such we assume $\gamma_1 = \gamma_2 = 0$. Furthermore, for transitions from state $|\nu\rangle$ to $|\mu\rangle$, the decoherence will be written as $\gamma_{\mu\nu} = \frac{1}{2}(\gamma_\mu + \gamma_\nu) + \gamma_{\mu\nu}^{dep}$, where both the decay from the two states and additional dephasing ($\gamma_{\mu\nu}^{dep}$) have been taken into account. We consider a system which is both closed and conservative and assume that the excited state decays to the two ground states with branching coefficients β_1 and β_2 , where $\beta_1 + \beta_2 = 1$. To keep things simple, we set $\beta_1 = \beta_2 = 1/2$.

We calculate the equations of motion for the density matrix elements to be,

$$\dot{\tilde{\rho}}_{11} = +\frac{1}{2}\gamma_3\tilde{\rho}_{33} + \frac{i}{2}\Omega_p(\tilde{\rho}_{31} - \tilde{\rho}_{13}) \quad (2.55a)$$

$$\dot{\tilde{\rho}}_{22} = +\frac{1}{2}\gamma_3\tilde{\rho}_{33} + \frac{i}{2}\Omega_c(\tilde{\rho}_{32} - \tilde{\rho}_{23}) \quad (2.55b)$$

$$\dot{\tilde{\rho}}_{33} = -\gamma_3\tilde{\rho}_{33} - \frac{i}{2}\Omega_p(\tilde{\rho}_{31} - \tilde{\rho}_{13}) - \frac{i}{2}\Omega_c(\tilde{\rho}_{32} - \tilde{\rho}_{23}) \quad (2.55c)$$

$$\dot{\tilde{\rho}}_{21} = \dot{\tilde{\rho}}_{12}^* = [-\gamma_{21} - i(\Delta_p - \Delta_c)]\tilde{\rho}_{21} + \frac{i}{2}\Omega_c\tilde{\rho}_{31} - \frac{i}{2}\Omega_p\tilde{\rho}_{32} \quad (2.55d)$$

$$\dot{\tilde{\rho}}_{31} = \dot{\tilde{\rho}}_{13}^* = (-\gamma_{31} - i\Delta_p)\tilde{\rho}_{31} + \frac{i}{2}\Omega_p(\tilde{\rho}_{11} - \tilde{\rho}_{33}) + \frac{i}{2}\Omega_c\tilde{\rho}_{21} \quad (2.55e)$$

$$\dot{\tilde{\rho}}_{32} = \dot{\tilde{\rho}}_{23}^* = (-\gamma_{32} - i\Delta_c)\tilde{\rho}_{32} + \frac{i}{2}\Omega_c(\tilde{\rho}_{22} - \tilde{\rho}_{33}) + \frac{i}{2}\Omega_p\tilde{\rho}_{12} \quad , \quad (2.55f)$$

where we have defined $\Delta_p = \omega_p - \omega_{31}$ and $\Delta_c = \omega_c - \omega_{32}$.

The equations can be simplified by making the following logical assumptions. First, for a good EIT signal to be generated, most of the atoms must initially populate the ground state $|1\rangle$, thus, $\tilde{\rho}_{11} \approx 1$ and $\tilde{\rho}_{22} = \tilde{\rho}_{33} \approx 0$. Second, if we take $\dot{\tilde{\rho}}_{32} = 0$, we find that $\tilde{\rho}_{32}$ is related to first order with Ω_p . Since we have assumed that the probe is weak compared to the coupling field and the Rabi frequency is proportional to the field amplitude, the last term in equation 2.55d can be neglected.

We are ultimately interested in $\tilde{\rho}_{31}$ which will allow us to describe the susceptibility of the medium with respect to the probe, as will be shown next. In order to calculate $\tilde{\rho}_{31}$, we can use the pair of simplified equations 2.55d and 2.55e, now of the form,

$$\dot{\tilde{\rho}}_{21} = \dot{\tilde{\rho}}_{12}^* = [-\gamma_{21} - i(\Delta_p - \Delta_c)]\tilde{\rho}_{21} + \frac{i}{2}\Omega_c\tilde{\rho}_{31} \quad (2.56a)$$

$$\dot{\tilde{\rho}}_{31} = \dot{\tilde{\rho}}_{13}^* = (-\gamma_{31} - i\Delta_p)\tilde{\rho}_{31} + \frac{i}{2}\Omega_p + \frac{i}{2}\Omega_c\tilde{\rho}_{21} \quad . \quad (2.56b)$$

In order to solve this, we write down equations 2.56 in a matrix form,

$$\mathbf{Y} = \begin{bmatrix} \tilde{\rho}_{21} \\ \tilde{\rho}_{31} \end{bmatrix}, \quad \mathbf{X} = \begin{bmatrix} -\gamma_{21} - i(\Delta_p - \Delta_c) & \frac{i}{2}\Omega_c \\ \frac{i}{2}\Omega_c & -\gamma_{31} - i\Delta_p \end{bmatrix}, \quad \mathbf{C} = \begin{bmatrix} 0 \\ \frac{i}{2}\Omega_p \end{bmatrix} . \quad (2.57)$$

Then, we can write,

$$\dot{\mathbf{Y}} = \mathbf{X} \cdot \mathbf{Y} + \mathbf{C} \quad , \quad (2.58)$$

which for $\dot{\mathbf{Y}} = 0$, has a solution of the form,

$$\mathbf{Y} = -\mathbf{X}^{-1} \cdot \mathbf{C} \quad . \quad (2.59)$$

From this, we calculate the two density matrix components,

$$\tilde{\rho}_{21} = \frac{\Omega_c \Omega_p}{4 \left\{ \frac{\Omega_c^2}{4} + [\gamma_{21} + i(\Delta_p - \Delta_c)](\gamma_{31} + i\Delta_p) \right\}} \quad (2.60)$$

$$\tilde{\rho}_{31} = \frac{\Omega_p(-i\gamma_{21} - \Delta_c + \Delta_p)}{2 \left\{ \frac{\Omega_c^2}{4} + [\gamma_{21} + i(\Delta_p - \Delta_c)](\gamma_{31} + i\Delta_p) \right\}} \quad . \quad (2.61)$$

Susceptibility

In the previous subsection, we have calculated the EIT density matrix element of interest, $\tilde{\rho}_{31}$. Now, we will relate it to the susceptibility/properties of the EIT medium.

As it has already been described earlier in this section, the polarisation of an atomic medium can be determined by,

$$\mathbf{P} = \mathcal{N} \langle \mathbf{d} \rangle \quad , \quad (2.62)$$

where \mathcal{N} is the atom number density and $\langle \mathbf{d} \rangle$ is the average dipole moment per atom, which can also be written in a different formalism,

$$\mathbf{P} = \mathcal{N} \text{Tr}(\mathbf{d}\rho) \quad , \quad (2.63)$$

which is useful as it relates polarisation to the dipole operator expectation value for the atomic medium being in the ρ mixed state. We can then expand the trace to get,

$$\mathbf{P} = \mathcal{N} \text{Tr} \left(\begin{pmatrix} \begin{bmatrix} 0 & 0 & \mathbf{d}_{13} \\ 0 & 0 & \mathbf{d}_{23} \\ \mathbf{d}_{31} & \mathbf{d}_{32} & 0 \end{bmatrix} & \begin{bmatrix} \rho_{11} & \rho_{12} & \rho_{13} \\ \rho_{21} & \rho_{22} & \rho_{23} \\ \rho_{31} & \rho_{32} & \rho_{33} \end{bmatrix} \end{pmatrix} \right) \quad (2.64)$$

$$\mathbf{P} = \mathcal{N} (\mathbf{d}_{31}\rho_{13} + \mathbf{d}_{23}\rho_{32} + \mathbf{d}_{13}\rho_{31} + \mathbf{d}_{32}\rho_{23}) \quad . \quad (2.65)$$

The elements of the density matrix were calculated in the previous section, in the rotating basis. Using the transformation, $\rho = \tilde{U}^\dagger \tilde{\rho} \tilde{U}$, where \tilde{U} , is the same as in equation 2.51,

we can now move back to the non-rotating basis, where,

$$\begin{bmatrix} \rho_{11} & \rho_{12} & \rho_{13} \\ \rho_{21} & \rho_{22} & \rho_{23} \\ \rho_{31} & \rho_{32} & \rho_{33} \end{bmatrix} = \begin{bmatrix} \tilde{\rho}_{11} & \tilde{\rho}_{12} e^{i(\omega_p - \omega_c)t} e^{i(\phi_p - \phi_c)} & \tilde{\rho}_{13} e^{i\omega_p t} e^{i\phi_p} \\ \tilde{\rho}_{21} e^{i(-\omega_p + \omega_c)t} e^{i(-\phi_p + \phi_c)} & \tilde{\rho}_{22} & \tilde{\rho}_{23} e^{i\omega_c t} e^{i\phi_c} \\ \tilde{\rho}_{31} e^{-i\omega_p t} e^{-i\phi_p} & \tilde{\rho}_{32} e^{-i\omega_c t} e^{-i\phi_c} & \tilde{\rho}_{33} \end{bmatrix}. \quad (2.66)$$

Thus, polarisation can be expressed as,

$$\mathbf{P} = \mathcal{N}(\mathbf{d}_{31} \tilde{\rho}_{13} e^{i\omega_p t} e^{i\phi_p} + \mathbf{d}_{23} \tilde{\rho}_{32} e^{-i\omega_c t} e^{-i\phi_c} + \mathbf{d}_{13} \tilde{\rho}_{31} e^{-i\omega_p t} e^{-i\phi_p} + \mathbf{d}_{32} \tilde{\rho}_{23} e^{i\omega_c t} e^{i\phi_c}) \quad (2.67)$$

At the same time, we know that polarisation can be expressed in terms of susceptibility as we have seen in equation 2.37,

$$\begin{aligned} \mathbf{P} &= \epsilon_0 \chi \mathbf{E} \\ &= \frac{\epsilon_0 \chi}{2} [\mathbf{E}_p (e^{i\omega_p t} + e^{-i\omega_p t}) + \mathbf{E}_c (e^{i\omega_c t} + e^{-i\omega_c t})] \quad (2.68) \end{aligned}$$

By comparing equations 2.67 and 2.68, and using equation 2.50, we get that the susceptibility as measured by the probe beam can be written as,

$$\chi(\omega_p) = \frac{2_c \mathcal{N} |\mathbf{d}_{31}| \tilde{\rho}_{31}}{\epsilon_0 \mathcal{E}_p} \quad (2.69)$$

This can be simplified even more by using a reduced susceptibility that is not a function of the properties of the EIT medium (and reminding ourselves that $\hbar\Omega_p = |\mathbf{d}_{31}| \mathcal{E}_p$),

$$\begin{aligned} \chi_r &= \frac{\hbar\gamma_{31}\epsilon_0}{\mathcal{N} |\mathbf{d}_{31}|^2} \chi \\ &= \frac{2\gamma_{31}}{\Omega_p} \tilde{\rho}_{31} \\ &= \frac{\gamma_{31}(-i\gamma_{21} - \Delta_c + \Delta_p)}{\frac{\Omega_c^2}{4} + [\gamma_{21} + i(\Delta_p - \Delta_c)](\gamma_{31} + i\Delta_p)} \quad (2.70) \end{aligned}$$

Figure 2.5 shows the reduced susceptibility as a function of the probe detuning. We can see that once $\Omega_c > 0$, the imaginary part of the susceptibility goes to zero and a transparency peak appears. As Ω_c is further increased, the width of the transparency peak gets broader and the spectrum is reminiscent of two absorption peaks getting separated, a phenomenon widely known as Autler-Townes splitting [78] that will be discussed in detail

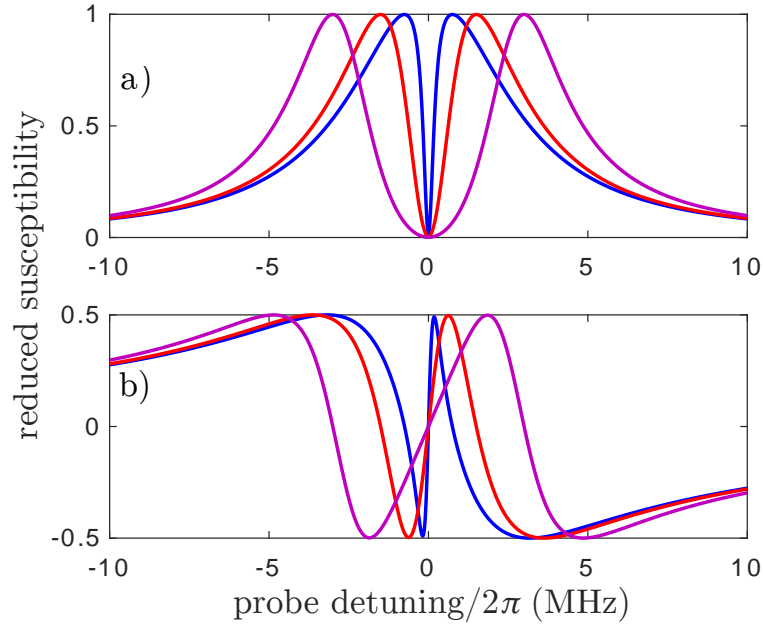


Figure 2.5: Reduced susceptibility plotted for various values of Ω_c , using equation 2.70. The parameters here for the three curves are $(\gamma_{31}, \gamma_{21}, \Delta_c) = (2\pi \times 3 \text{ MHz}, \gamma_{31}/1000, 0)$ and $\Omega_c = (0.5, 1, 2) \times \gamma_{31}$, for the blue, red and purple curve respectively. a) Imaginary part of susceptibility is shown. Near resonance, this goes to zero, meaning there is no absorption. b) Real part of susceptibility. The positive slope around zero frequency gets less steep as Ω_c is being increased.

in Chapter 7. At the same time, for the real part of susceptibility, a steep positive slope around zero probe detuning appears. The slope gets shallower as Ω_c is being increased.

Figure 2.6 shows how susceptibility tunes with respect to the decoherence term, γ_{21} . It can be seen that the imaginary part of the susceptibility goes to zero only when γ_{21} is low. For increased decoherence, the EIT resonance gets from barely to not at all visible. Furthermore, the slope around zero detuning for the real part of susceptibility gets shallow for high γ_{21} and even changes sign. This clearly demonstrates the importance of coherence between $|1\rangle$ and $|2\rangle$ for EIT.

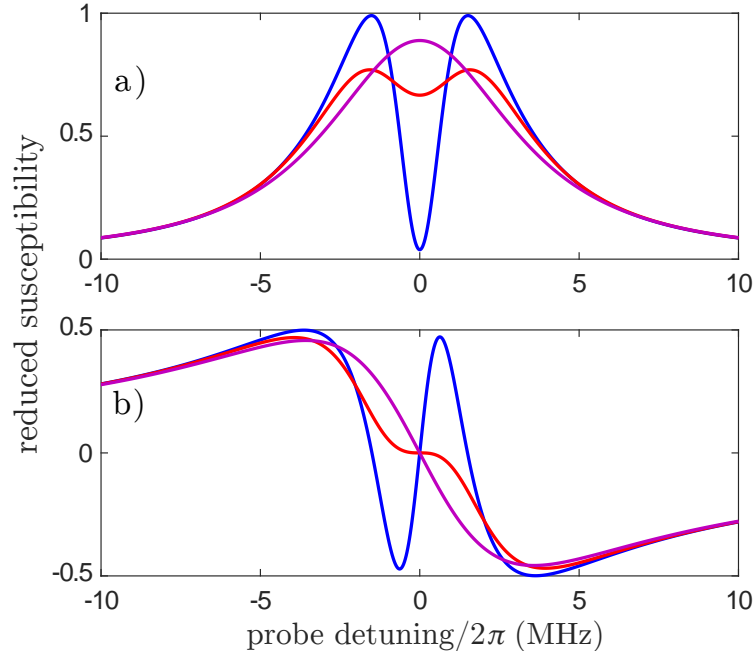


Figure 2.6: Reduced susceptibility, plotted for various γ_{21} , using equation 2.70. The parameters here for the three curves are $(\gamma_{31}, \Omega_c, \Delta_c) = (2\pi \times 3 \text{ MHz}, 1 \times \gamma_{31}, 0)$ and $\gamma_{21} = (0.01, 0.5, 2) \times \gamma_{31}$, for the blue, red and purple curve respectively. a) Imaginary part of susceptibility is shown. Near resonance, this goes to zero as long as γ_{31} is kept low. b) Real part of susceptibility. The positive slope around zero frequency gets less steep and even changes sign as γ_{21} is being increased.

2.2.3 Electromagnetically induced transparency in an atom-cavity system

Whilst the semi-classical approach followed in the previous section was useful in understanding the effect of the EIT technique on the properties of the atomic medium, here we will switch to a fully quantum mechanical approach to investigate the properties of the strongly coupled atom-cavity system. In the following pages, the Hamiltonian of the system will be derived and the cavity transmission will be plotted, by solving the master equation.

Hamiltonian

We consider the same three-level atom with energy levels $|1\rangle$, $|2\rangle$ and $|3\rangle$, as in the previous section. The probe field is close to resonance with the $|1\rangle \leftrightarrow |3\rangle$ transition and has a Rabi and optical frequency Ω_p and ω_p , respectively. The probe will drive the cavity at a rate ξ (ξ depends on the probe beam intensity and the cavity transmission). On the other hand, the coupling field (Ω_c, ω_c) addresses the $|2\rangle \leftrightarrow |3\rangle$ transition. The atoms are strongly coupled to a cavity (ω_{cav} ¹¹), on $|1\rangle \leftrightarrow |3\rangle$. The atomic medium-cavity Rabi frequency is $2G$. For now, no dephasing terms will be considered.

The Hamiltonian describing the system is:

$$\begin{aligned} \frac{H}{\hbar} = & \omega_{\text{cav}} a^\dagger a + \omega_a |3\rangle \langle 3| + \Delta |2\rangle \langle 2| - \xi(a^\dagger e^{-i\omega_p t} + a e^{i\omega_p t}) \\ & - G(|1\rangle \langle 3| + |3\rangle \langle 1|)(a^\dagger + a) - \Omega_c(|2\rangle \langle 3| + |3\rangle \langle 2|) \cos(\omega_c t) \quad , \end{aligned} \quad (2.71)$$

where Δ is the frequency difference between $|1\rangle \leftrightarrow |2\rangle$ and we have assumed Δ is much greater than G , Ω_c and the decay rates we will consider below.

After a number of transformations similar to those shown earlier, the Hamiltonian becomes:

$$\begin{aligned} \frac{H}{\hbar} = & -(\omega_p - \omega_{\text{cav}}) a^\dagger a - (\omega_p - \omega_a) |3\rangle \langle 3| - (\omega_p - \omega_c - \Delta) |2\rangle \langle 2| \\ & - \xi(a^\dagger + a) - G(|1\rangle \langle 3| a^\dagger + |3\rangle \langle 1| a) - \frac{1}{2} \Omega_c(|2\rangle \langle 3| + |3\rangle \langle 2|) \quad . \end{aligned} \quad (2.72)$$

For the special case that $\omega_{\text{cav}} = \omega_a$ (i.e. for which the normal-mode splitting happens) and the coupling beam is exactly on resonance ($\omega_c + \Delta = \omega_a$),

$$\begin{aligned} \frac{H}{\hbar} = & -\delta(a^\dagger a + |3\rangle \langle 3| + |2\rangle \langle 2|) - \xi(a^\dagger + a) \\ & - G(|1\rangle \langle 3| a^\dagger + |3\rangle \langle 1| a) - \frac{1}{2} \Omega_c(|2\rangle \langle 3| + |3\rangle \langle 2|) \quad , \end{aligned} \quad (2.73)$$

where $\delta = \omega_p - \omega_{a,\text{cav}}$.

¹¹Note that here, the cavity frequency is symbolised as ω_{cav} instead of as ω_c that used to be the case in Section 2.1. The reason is because we chose ω_c to represent the frequency of the coupling beam, as it has been the case from the beginning of Section 2.2.

Master equation

The dynamics of the system can be studied using the the master equation, which in the Lindblad form [76], reads as,

$$\dot{\rho} = \frac{-i}{\hbar}[H, \rho] + \kappa\mathcal{D}[a]\rho + \gamma_{13}\mathcal{D}[|1\rangle\langle 3|]\rho + \gamma_{23}\mathcal{D}[|2\rangle\langle 3|]\rho + \gamma_{21}\mathcal{D}[|2\rangle\langle 1|]\rho \quad , \quad (2.74)$$

where, $\mathcal{D}[O]\rho = 2O\rho O^\dagger - O^\dagger O\rho - \rho O^\dagger O$, γ_{13} accounts for the decay rate from $|3\rangle \rightarrow |1\rangle$, γ_{23} accounts for the decay rate from $|3\rangle \rightarrow |2\rangle$, and γ_{21} for the dephasing between $|2\rangle \leftrightarrow |1\rangle$.

By requiring that $\dot{\rho} = 0$, the photon output rate at steady state (and hence the normalised cavity transmission) can be calculated as,

$$T = \left(\frac{\kappa}{\xi}\right)^2 \text{Tr}(a^\dagger a \rho) \quad . \quad (2.75)$$

This was solved numerically using *QuTiP* [79], a module available on Python dedicated to solving the dynamics of open quantum systems.

Figure 2.7 shows example cavity transmission spectra for a range of parameters. We chose our system to lie in the strong coupling regime and, as such, when $\Omega_c = 0$ the splitting of the normal mode of the cavity is apparent and transmission goes to zero when the probe is on resonance. When $\Omega_c > 0$, transparency is attained and a narrow peak appears. The transparency peak becomes smaller as γ_{21} is being increased, highlighting the importance of eliminating decoherence mechanisms in such a system.

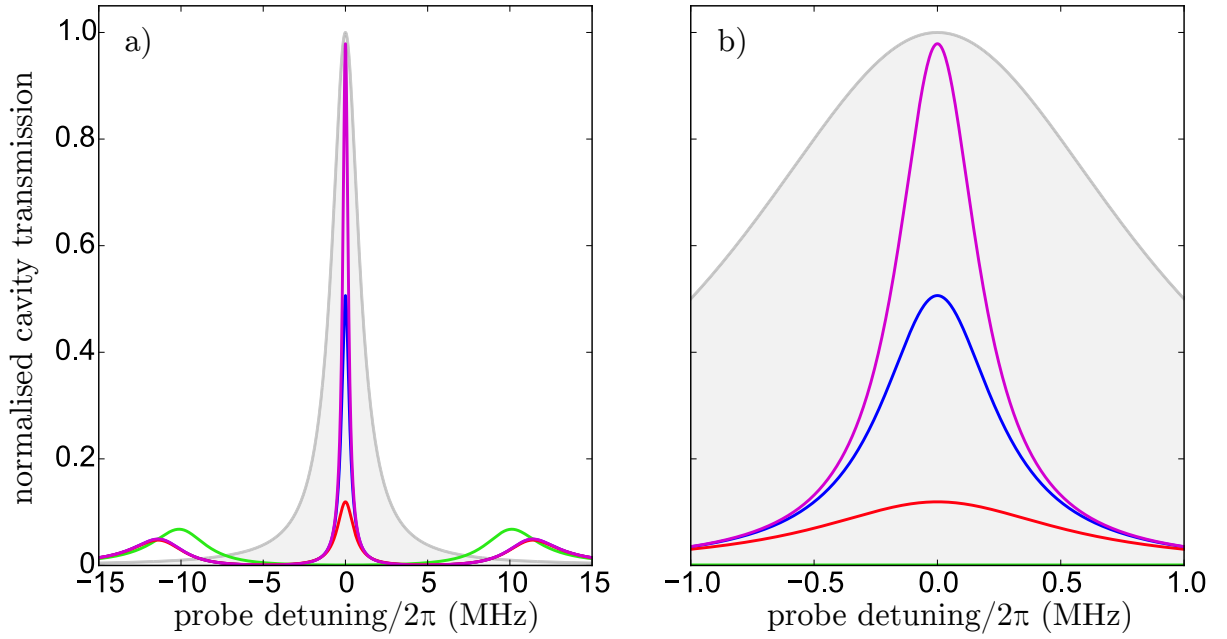


Figure 2.7: Normalised cavity transmission. The parameters here are $(G, \kappa, \gamma_{13}) = 2\pi \times (10, 1, 3)$ MHz, and $(\xi, \gamma_{23}) = (\kappa, \gamma_{13})/1000$. For the green curve, $\gamma_{21}, \Omega_c = 0$. For the purple, blue and red curves, $\Omega_c = 2\pi \times 10$ MHz, and $\gamma_{21} = 2\pi \times (0.0, 0.1, 0.5)$ MHz, respectively. The cavity transmission without atoms is in grey. An increase in the normal-mode splitting when $\Omega_c > 0$ is noticeable. Figure a) is same as b), just for a different detuning range.

Chapter 3

Experimental apparatus

This chapter will present the different components of our experimental setup. Its main objective is to provide the reader with all the information necessary to understand how the experiment works, without including the “non-essential” details. Emphasis will be given to setups that have been developed during the time of this PhD. More detailed descriptions of particular parts of the apparatus may be found in former students’ theses [80–82].

The chapter is divided into four sections. The vacuum system, necessary for cold atom experiments, will be presented first, and then the laser systems making possible the atom laser cooling and study of light-matter interactions will be described. The third section explains the details of our ring cavity design and how different parameters such as the single atom-photon coupling constant can be obtained. Finally, the magnetic field configuration we employ to spatially trap atoms will be presented, and an outstanding issue deriving from when we shut off the field during measurements will be discussed.

Since typical cold atom experiments have a lifetime which is longer than the duration of a PhD, and usually more than one person is involved in the experiment at the same time, it is useful to make clear my involvement and contribution to the project. Specifically, during this PhD, I have worked in the design and assembly of the vacuum system, and in the design and set up of the laser systems (in particular of the atom-cavity system;

Robert Culver and Komal Pahwa have worked in the atom cooling and trapping system, whereas Robert has also helped in the atom-cavity system). Furthermore, I was involved in the design of the ring cavity and in the making of the coils generating the magnetic field for the atom trapping.

We shall make a note here that all trade names and part numbers included in this thesis are used for identification purposes only. They do not constitute endorsements. The performance of other products may be similar or even better.

3.1 Vacuum

Ultra-high vacuum systems are an essential part of cold atom experiments, which cannot take place under atmospheric pressure where the mean free path is on the order of $1\ \mu\text{m}$ [83]. Our vacuum system is composed of two main chambers that are connected to each other by a narrow graphite tube¹ and have a calculated two-orders of magnitude relative pressure difference [80]. The chamber with the relatively higher pressure serves as the atom collection and preparation chamber, while the second chamber, which from now on we will be calling the science chamber, houses the ring cavity and is where we study light-matter interactions with cold atoms. In a previous generation of this experiment, the science chamber housed both the atom source (alkali metal dispensers²) and the ring cavity. This single-chamber version of the experiment was found to have a limited useful lifetime as the cavity mirrors got gradually and irreversibly dirty, leading to a degradation of the cavity linewidth from $\sim 1\ \text{MHz}$ to $>20\ \text{MHz}$, within three months of the dispensers first firing. The two-chamber design ensures that the cavity mirrors are kept clean, and also prolongs the 3D-MOT lifetime as it reduces collisions between atoms and background gas.

A computer-aided design (CAD) drawing of our vacuum system is shown in Figure 3.1.

¹Goodfellow, 494-159-79.

²SAES, K/NF/4.5/25/FT10.

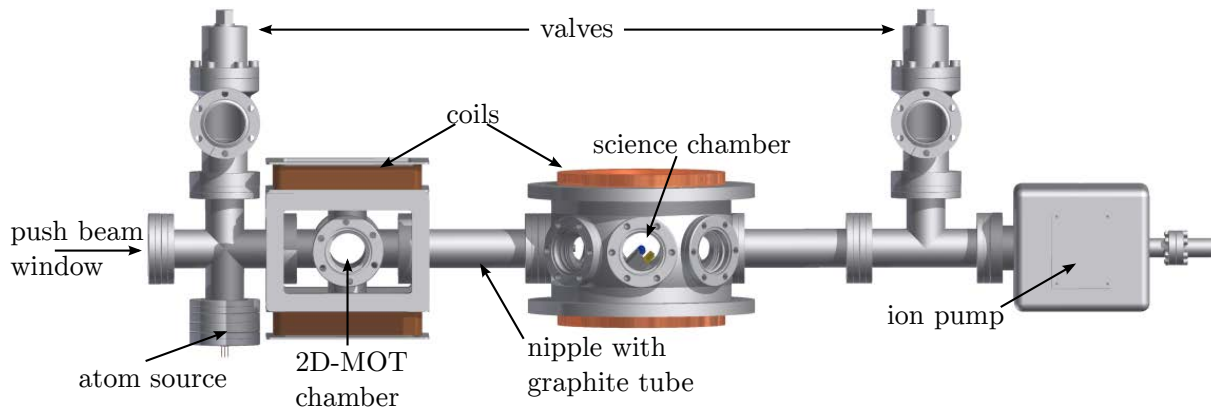


Figure 3.1: A CAD drawing of the vacuum system as viewed from the side, with its different parts and the coils we use to make our 2D- and 3D-MOT, shown.

The dispensers release atoms on the walls of a stainless steel cross which are heated in order to maintain high potassium vapour pressure. The dispensers cross is next to the two-dimensional magneto-optical trap (2D-MOT) chamber where the atoms are first collected. This chamber is simply composed of a six-way cross and four viewports³ with a 15 mm radius aperture and a broadband anti-reflective coating⁴ for the two pairs of orthogonal MOT beams. A beam shone from another viewport (push beam window), which is orthogonal to the 2D-MOT axes, pushes the pre-cooled 2D-MOT atoms towards the science chamber.

The atoms traverse through the graphite tube and make their way to the science chamber where they get re-collected by a 3D-MOT, and are spatially overlapped with the cavity mode (by design). A spherical octagon⁵ and eight viewports (six for the MOT beams and two serving as the cavity input and output ports) compose this chamber. The ring cavity is mounted on a reducing flange⁶ which has been modified by the school's workshop in order to accommodate an electrical feedthrough⁷ (powering the cavity piezo) and to rigidly mount the cavity frame.

The vacuum system also comprises a 20 Ls^{-1} ion pump⁸ which is attached to the other

³Torr Scientific, VPZ38BBARLN.

⁴All viewports used in the experiment are of the same type.

⁵Kimball Physics, MCF600-SphOct-FC28.

⁶Kurt J. Lesker, DN100CF-DN40CF.

⁷Kurt J. Lesker, IFTAG034031.

⁸Agilent Technologies, 9191145 Vacion Plus 20.

end of the science chamber, and two angle valves⁹ installed on each side of the system. The valves connect the system to turbo pumps during bake-down periods and are also used to switch from using the turbo pump to using the ion pump when a low enough pressure is reached, without breaking the vacuum.

3.2 Laser systems

While the vacuum system provides an ultra-low pressure environment that is suitable for cold atom experiments, lasers are necessary to make a MOT and to study light-matter interactions. We make use of two independent laser systems, each one having a very different but equally important role to play in the experiment. The first system that will be described is responsible for generating the beams required to laser cool the atoms, in a 2D- and a 3D-MOT. The second laser system is responsible for probing and stabilising the length of the ring cavity as well as for generating the coupling beam, which is used in order to achieve EIT.

Before discussing the two laser systems, we shall describe how we control the different experimental parameters, such as the frequencies of the laser beams, in the experiment. The key element in this process is a commercial control board¹⁰. The board has 8 analogue channels that are used to control voltage controlled oscillators (VCOs). Then, the VCOs' outputs, either mixed with other beat-notes or fed directly to acousto-optical modulators (AOMs), control the frequency of the light beams in the experiment. The board also has 8 digital channels. We use these channels to instruct shutters and RF switches to block/unblock and switch on/off beams, respectively, and to trigger the camera (used for MOT imaging purposes) and oscilloscope. More information regarding the computer control of the experiment can be found in [80].

⁹VAT Vacuum Products Ltd, 54132-GE02-0001.

¹⁰National Instruments, PCI-6733.

3.2.1 Atom cooling and trapping

Light addressing specific transitions is required in order to make a MOT. This light in our experiment is provided by three external cavity diode lasers (ECDL) operating at 766.7 nm, which corresponds to the D₂ line of ³⁹K. The lasers were built based on the design described in [84]. As will be explained in Chapter 5, two different frequencies are necessary to make a ³⁹K MOT. The two frequencies are called the “cooling” and “repump”, and are indicated on the saturated absorption spectroscopy signal shown in Figure 3.2a). We have dubbed our lasers “master”, “push” and “MOT” based on their operation. In order to keep the setup relatively simple, we use the same frequencies to make the 2D- and the 3D-MOT. An overview of the laser system is shown in Figure 3.2b).

The master laser is the first laser to be locked¹¹ in our laser “locking sequence”. This laser is locked using a technique called sub-Doppler magnetically-induced dichroism (MIDL) [85] at the crossover feature of the spectroscopy signal shown in Figure 3.2a), and has been providing a very reliable error signal since it was first set up (May, 2012). The main purpose of the master laser is to provide a stable frequency reference as the other lasers of the system are locked with respect to it. The basic stability requirement here is that the frequency of the master (and the other lasers that compose this laser system) does not vary by more than the natural linewidth Γ , which for the D₂ line of ³⁹K is 6.035 MHz [86]. The master laser was found to have a 0.8 MHz frequency stability¹² [80].

The push laser is the second laser in the locking sequence and is stabilised using a beat-note offset lock (BOL₁) [87] to the master, with approximately 0.95 MHz frequency stability. This laser is red-detuned by a few Γ from the $F = 1 \rightarrow F' = 2$ transition and generates the beam that pushes the 2D-MOT atoms into the science chamber. The push beam has 1 mm $1/e^2$ intensity radius, ~ 1 mW power, and linear polarisation. It is

¹¹To lock the laser means to stabilise it to a certain frequency.

¹²The stability of the locks discussed in this thesis was estimated by calculating the ratio between the root mean square noise level and the slope of the error signal.

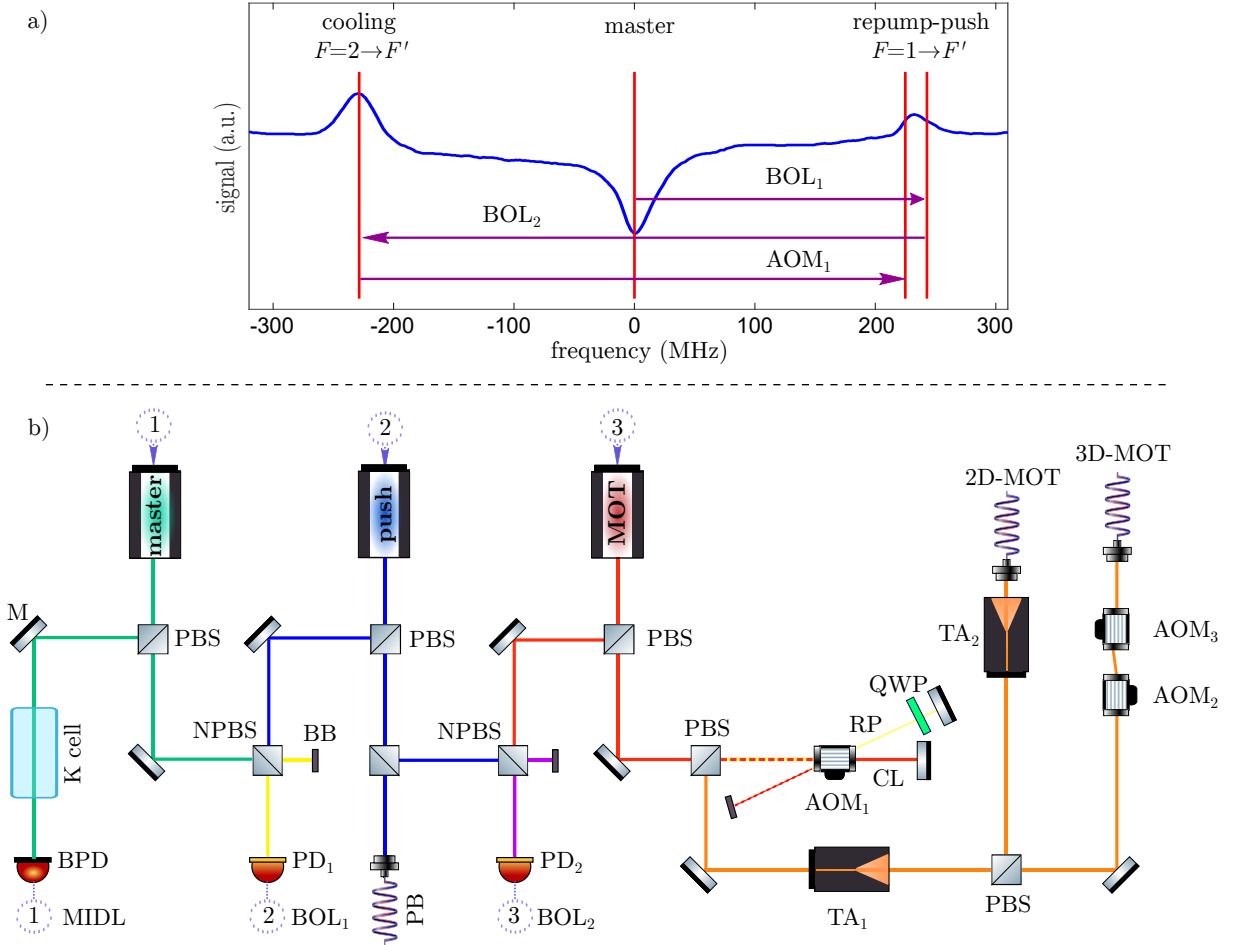


Figure 3.2: The MOT laser system. a) Saturated absorption spectroscopy on the D_2 potassium line, indicating the approximate frequency of the different beams involved in the atom cooling and trapping system. The repump-push frequencies should approximately be identical; they have only been shifted in frequency for better visualisation of the system. The frequency splitting between $F = 1 \rightarrow F' = 0, 1, 2$ and $F = 2 \rightarrow F' = 1, 2, 3$ corresponds to the ground-state hyperfine splitting and is 461.7 MHz. The transmission dip at the centre of the spectrum corresponds to the crossover between the ground states. The locking sequence is described in the text. b) An overview of the laser system responsible for making the MOTs. The colour coding used here does not relate to a). Most of the optics and other components have been omitted here. Numbers in circles represent locks feeding back to the lasers. M: mirror; (N)PBS: (non-)polarising beam splitter; BB: beam block; AOM: acousto-optic modulator; (B)PD: (balanced) photodetector; TA: tapered amplifier; RP: repump; CL: cooling; QWP: quarter-wave plate; PB: push beam; MIDL: magnetically-induced dichroism; BOL: beat offset lock.

possible to control whether this beam is on/off by the use of a shutter, which is useful as the push beam needs to be on when we are loading atoms in the 3D-MOT, but needs to be off during other measurements.

The last but most important laser in the sequence is the MOT laser. This laser is locked with the same offset locking technique to the push laser (BOL₂; MOT-push lock stability ~ 0.89 MHz) and is responsible for the generation of both the cooling and repump light. The MOT laser operates near the cooling transition frequency (i.e. $F = 2 \rightarrow F' = 3$) and in order to derive the light addressing the repump transition ($F = 1 \rightarrow F' = 2$), we double pass AOM₁. The unshifted beam is then used as the cooling light and the double-shifted first order of diffracted light as the repump¹³. In order to optimise the different MOT parameters such as the atom number and temperature, it is important to get the cooling and repump light at the correct frequencies and powers.

We combine the cooling and repump light and inject a home-built tapered amplifier (TA₁¹⁴) with them; TA₁ is described in [82]. Their combined power before injecting TA₁ is ~ 10 mW, and the output power from TA₁ is > 500 mW. At the same time, the cooling to repump power ratio is 1:1 before the injection and becomes 3:2 after TA₁. We then split this light to two different paths, to couple it into the 2D-MOT and 3D-MOT fibres.

A portion of the light that comes out of TA₁ gets fibre coupled and goes to TA₂¹⁵, specified for 780 nm. We use the light coming out of TA₂ to make our 2D-MOT. TA₂ provides a $> 3\times$ amplification of the fibre input light. Using fibre 50:50 beam splitters and appropriate collimators we end up with two beams with one-inch $1/e^2$ (intensity) diameter and ~ 40 mW/cm² peak intensity, each. We make our 2D-MOT by retro-reflecting the two beams on a quarter-wave plate (QWP) and a mirror.

The rest of the light coming out of TA₁ is used in order to make the 3D-MOT. The light is single-passed through two consecutive AOMs (AOM_{2,3}), which shift the frequency in opposite directions by the same amount, resulting in no overall frequency shift. The light is then fibre coupled. This is done in order to be able to switch off the MOT beams

¹³By unshifted we mean the (0,0) diffraction mode and by shifted we mean the (+1,+1) diffraction mode, where the first index represents the diffraction mode for the forward pass and the second index represents the diffraction mode for the reflected path.

¹⁴M2K Laser, M2K-TA-0765-1000, DHP-F packaging.

¹⁵New focus, TA-7613-P. This TA has been borrowed from another experiment in the group, working with rubidium.

very fast by simply turning to zero the RF power to the AOMs. The three MOT beams that we use have one-inch $1/e^2$ (intensity) diameter and ~ 10 mW/cm² peak intensity each, and are also retro-reflected on a QWP and a mirror.

3.2.2 Probing the atom-cavity system

While the laser system just described provides the light to make our MOTs, a second independent laser system is dedicated to the stabilisation of the length of the ring cavity and the generation of the probe and coupling beams enabling the study of cQED and EIT in our experiment.

The three most important components of the system are two commercial lasers¹⁶ and a Fabry-Pérot (FP) cavity. One of the two lasers operates at 770.1 nm (D₁ line of ³⁹K, thus we will be calling this as the “potassium” laser) and is used to probe the cavity and the atoms inside the cavity. The other laser operates near 852 nm (and as this wavelength is near resonance with the D₂ line of caesium-133 (¹³³Cs) [88], we will be calling it as the “caesium” laser). The caesium laser is used for the length stabilisation of the ring cavity, and as such, its wavelength was chosen primarily as it is far away from potassium resonances, hence it minimally disturbs the atoms inside the science cavity¹⁷. Lastly, the FP cavity is used in order to stabilise the frequency of the potassium and caesium lasers to the same reference.

In Figure 3.3a) the different frequencies generated by the potassium laser are indicated with respect to the D₁ line saturated absorption spectrum. Furthermore, in b) a simplified schematic of the laser system is shown. The locking sequence for this system is as follows. Firstly, the potassium laser is locked to the FP cavity using the well-known Pound-Drever-Hall (PDH) technique [89, 90]. Then, the FP cavity is scanned and locked to the potassium spectroscopy using the already frequency stabilised potassium laser light. The error signal

¹⁶Toptica, DLPro.

¹⁷Additional reasons for this choice were the high reflectivity of the ring cavity mirrors for light at 852 nm (discussed in Section 3.3), as well as the availability of vapour cells and other optical components at this wavelength.

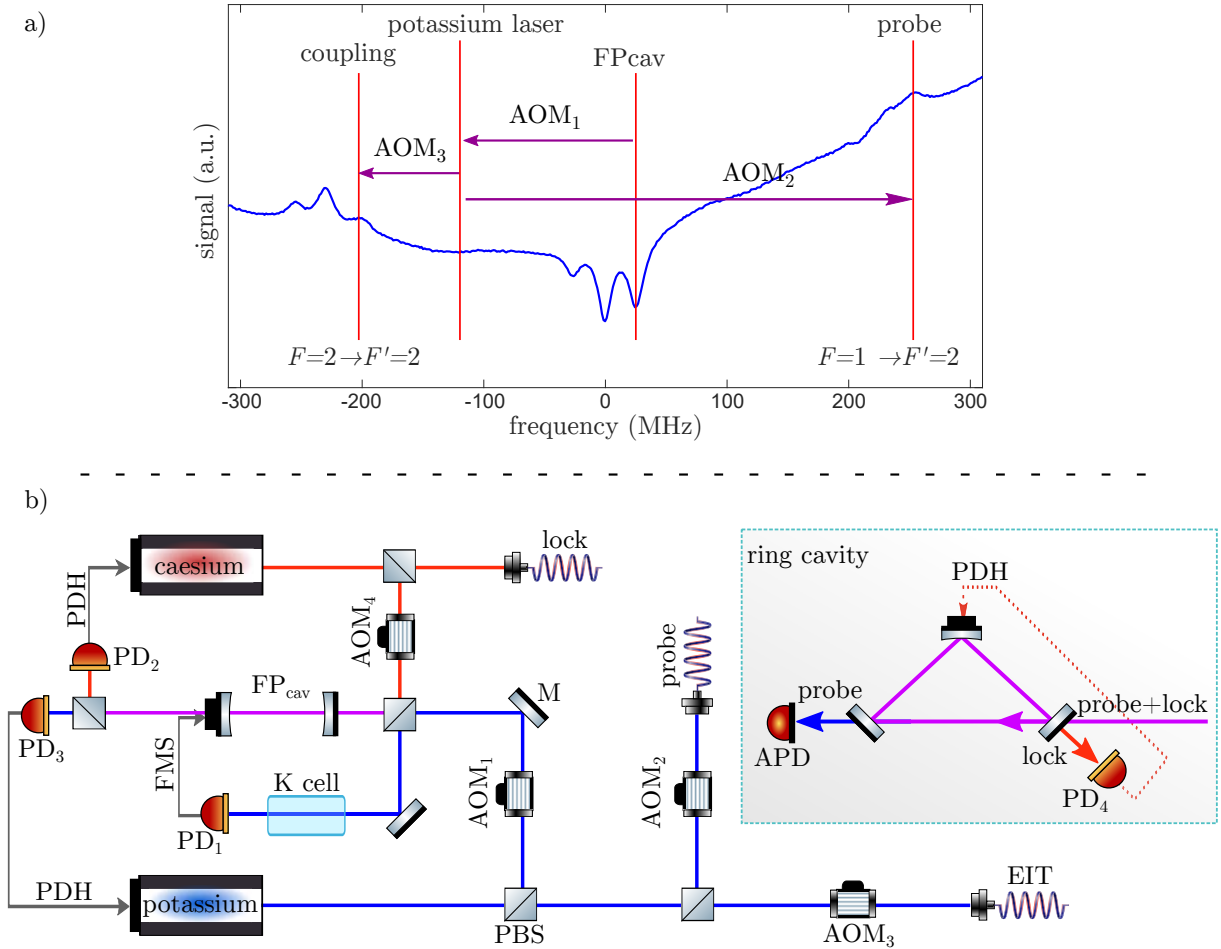


Figure 3.3: The atom-cavity system. a) Saturated absorption spectroscopy on the D_1 potassium line, indicating the frequencies associated with the potassium laser. Note that in comparison to the D_2 line spectroscopy, here the different transitions are easier to identify. b) The parts that compose the atom-cavity probing laser system are presented. Note that the colour coding used here does not relate to a). Dichroic filters, which are used to separate the two wavelengths at different places, have been omitted as well as most of the other optical components of the system. All the AOMs except from AOM_3 are in a double-pass configuration. M: mirror; PBS: polarising beam splitter; AOM: acousto-optic modulator; (A)PD: (avalanche) photodiode; FMS: frequency modulation spectroscopy; PDH: Pound-Drever-Hall; FP_{cav} : Fabry-Pérot cavity.

enabling this lock is derived by employing the frequency modulation spectroscopy (FMS) technique [91]. Following, the caesium laser is also locked to the FP cavity, again by using the PDH method. Lastly, the ring cavity length is locked using the stabilised caesium light, once again by applying the PDH technique.

After presenting an overview of this laser system, we will next discuss in more detail the role of the lasers and the FP cavity in the experiment.

Potassium laser

The potassium laser is current modulated at ~ 17 MHz to produce the frequency sidebands, required for locking purposes. Its output light power is split into three to serve the different purposes of the experiment (as shown in Figure 3.3).

In the first path, the light is double-passed through AOM₁ and then splits in order to probe: a) the FP cavity and b) the potassium vapour cell. Using the transmitted light in a) the laser is locked to the cavity using PDH (potassium laser-FP cavity lock stability is about 0.84 MHz), whereas by using the light in path b) the FP cavity is stabilised using the FMS technique, which is calculated to provide a 0.7 MHz frequency stability to the cavity.

Light in the second path double-passes through AOM₂ before it gets fibre coupled. This light is used for probing the ring cavity, and once the potassium laser is stabilised using light in the first path, the probe frequency can be scanned (using AOM₂).

Most of the light coming out of the laser is used in the third path. There, the light single-passes AOM₃ and the first order of diffracted light is fibre coupled and used as the EIT (coupling) beam. We use an AOM here in order to be able to switch this beam on and off rapidly. This beam is single-passed (not double-passed like the rest) in order to obtain the maximum optical power available.

Before moving to the details of the caesium laser, summarising the role of the different AOMs in this system is useful. First, the frequency of the coupling beam can be tuned (together with that of the probe beam) using AOM₁, which is useful for when we are looking for the EIT resonance. Additionally, the probe frequency can be set and scanned using AOM₂, which is necessary for when we are probing the cavity and the potassium atoms, for cQED and EIT related measurements. Lastly, AOM₃ provides a fast optical switch for the coupling beam.

Caesium laser

As with the potassium laser, the caesium laser is also current modulated at ~ 17 MHz. The output power of this laser splits into two separate paths (see Figure 3.3b)). A portion of the light double-passes AOM₄, probes the FP cavity, and then, by exploiting the PDH technique, it is used to lock the laser to the FP cavity (with calculated 0.93 MHz lock stability). The rest of the light is used to probe the ring cavity. By collecting the reflected 852 nm light from the input mirror of the cavity and once again applying the PDH technique we stabilise the ring cavity length to the already frequency stabilised caesium laser (0.8 MHz frequency stability). Therefore, the ring cavity length can be tuned by changing the AOM₄ frequency.

Fabry-Pérot cavity

The design of the FP cavity is mostly based on [92] and is extensively discussed and characterised in [81]. The cavity is about 19 cm long and is built out of cylindrical brass pieces, two curved mirrors¹⁸ with 15 cm radius of curvature each and 99% power reflectivity, and a ring piezo¹⁹. The measured linewidth for 770 nm and 852 nm light is 3.8(2) MHz and 4.4(2) MHz respectively.

By properly choosing the cavity length, a number of degenerate transverse modes satisfy the resonance condition [92]. This leads to a subdivision of the free spectral range of the cavity and offers fine-tuning of the frequency of the lasers that are locked to it.

We lock both our potassium and caesium lasers to the Fabry-Pérot cavity, using the PDH technique. This achieves a correlated stability between the two lasers. We have chosen the modulation frequency of the lasers to be half of the mode spacing in order to make the comb of lock points even more dense. The cavity itself is locked using the FMS technique, as previously discussed.

¹⁸Melles Griot/CVI.

¹⁹Piezomechanik, HPCh 150/12-6/2.

3.3 Ring cavity

At the heart of our experiment lies the ring cavity. Figure 3.4 shows the cavity fully assembled and under vacuum. On the far right of the photograph, the tube from which the pre-cooled atoms emerge is also visible. The design of the ring cavity and its different parameters relevant for cQED studies are discussed in this section.

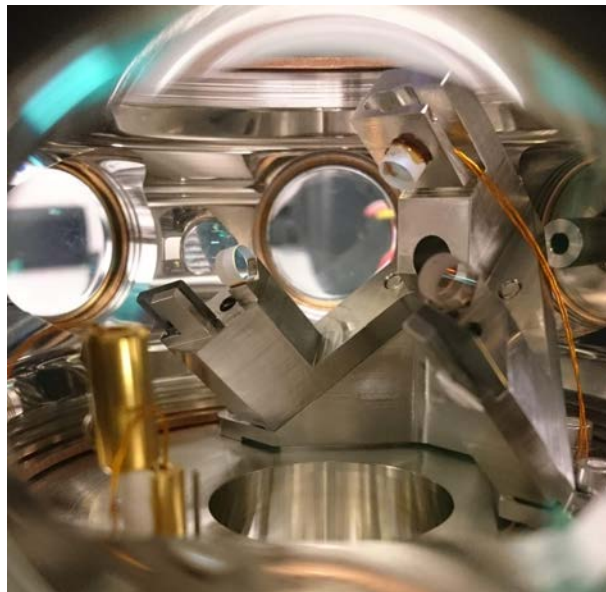


Figure 3.4: Photograph of the ring cavity under vacuum from a MOT beam window. The tube connecting the 2D-MOT chamber with the science chamber is visible on the right.

3.3.1 Design and assembly

The ring cavity is mainly composed of two stainless steel parts (see Figure 3.5a) and b)); the cavity frame, which has a monolithic design and is where all the mirrors are glued, and the “tilting block” which elevates the cavity frame to a 45° angle, in order to avoid the incoming atomic beam from the 2D-MOT chamber.

The cavity consists of two flat and a curved mirror, of 3.175 mm radius and 4 mm thickness each. These three mirrors form a right-angle triangle with an intended 40 mm hypotenuse. The flat mirrors serve as the input/output ports of the cavity, and the curved central mirror, with a 100 mm radius of curvature, helps to steer the beam and get the

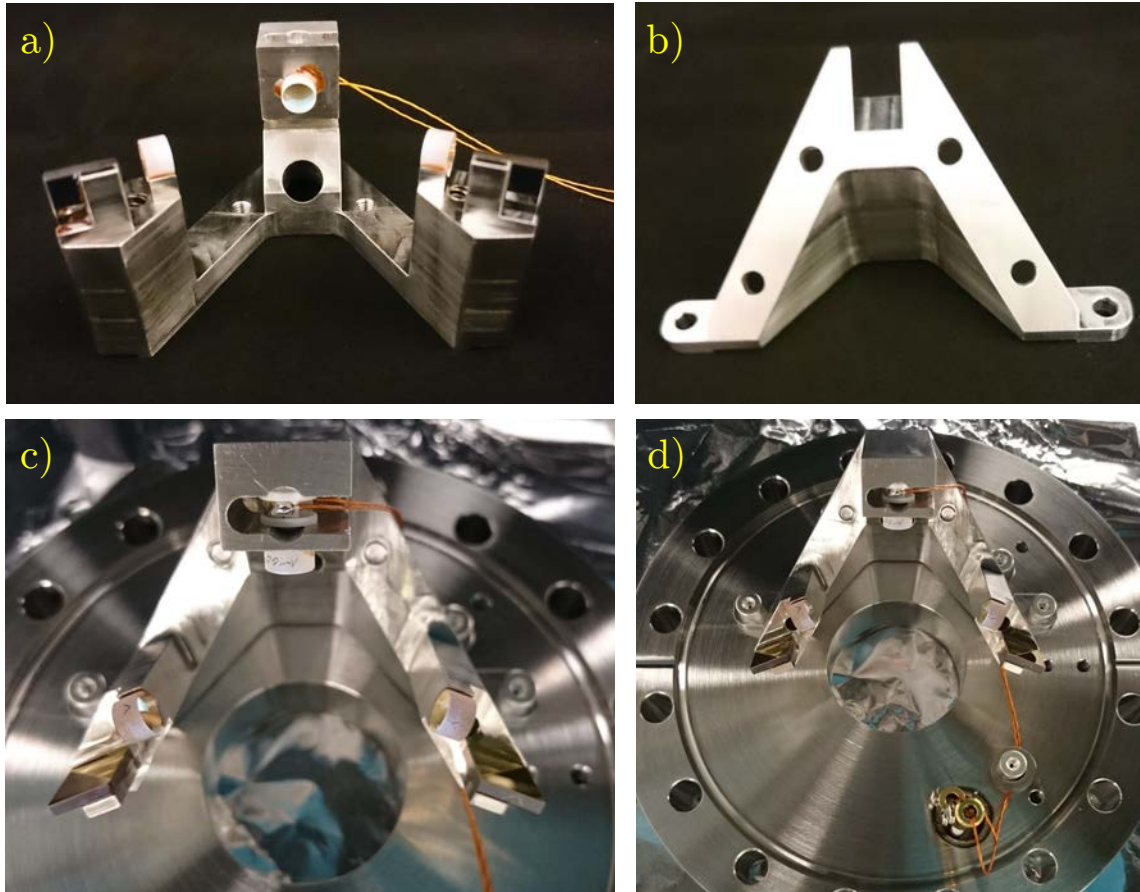


Figure 3.5: The ring cavity assembly. a) The cavity frame with all mirrors glued on it. The hole in the frame which allows the atoms to enter the cavity mode is also visible. b) The 45° tilting block. c) Zooming in on the flex mount with the piezo and ceramics that isolate it from the frame on the focus. d) The fully assembled cavity on the mounting flange. Note how the piezo wires are clamped and connected to the electrical feedthrough.

cavity aligned. Two additional square gold mirrors (5 mm×5 mm, 2 mm thick), positioned behind the flat mirrors at a right angle, assist in the steering of reflected light out of the chamber. Additionally, a 7.5 mm hole on the cavity frame allows atoms to pass through the cavity frame into the 3D-MOT chamber.

The cavity length can be altered using a vacuum-compatible piezo that is placed into a flexure mount just behind the central curved mirror, visible in Figure 3.5c) and d). Two ceramic disks, one at each side of the piezo, ensure that it does not make electrical contact with the cavity frame. The piezo wires are clamped onto the mounting flange and make their way to an electrical feed-through (see Figure 3.5d)).

The cavity design that has just been described complements the aforementioned modifications in the vacuum system. After the previous single-chamber version of our vacuum system failed to keep the cavity mirrors clean, together with modifications to the vacuum design, we also made some changes to the cavity. First, the cavity now is tilted and has a hole on its frame to let the pre-cooled atoms to enter the science chamber (previously there was no need for those). Furthermore, the new design addresses previous limitations such as the unavailability of access to both faces of the flat mirrors, and the curved mirror being directly glued to the piezo. The former was solved by gluing the mirrors on v-grooves, and is useful as in case the cavity mirrors get dirty again then we can break vacuum and clean them with acetone and isopropanol. The latter was addressed by the flexure mount and is also useful as if we want to separate the piezo from the curved mirror, we can just do that without damaging either or both of them.

3.3.2 Parameters

Here, we summarise the most important cavity parameters. All the parameters apart from the linewidth were measured by Robert Culver [80]. As such, it is beyond the scope of this thesis to get into the details of these particular measurements. However, it is important to provide a full list of them and understand their role in cavity-atom interactions.

Table 3.1 lists all the measured parameters which are associated with the cavity. The power transmission and reflection parameters of the cavity mirrors were measured by analysing many on resonance transmission and reflection spectra and taking into account effects from imperfect mode-matching. The values indicated here are for 770.1 nm light, but the mirrors are specified to have similar behaviour for light at 852 nm.

The cavity length (l) was determined using a technique that relied on the splitting of the transverse modes of the cavity. This technique is particularly useful when the free spectral range (FSR), defined as $FSR = c_0/l$, is large, as it is not susceptible to nonlinearities in the laser or cavity piezo scan. The tangential (w_{\parallel}) and sagittal (w_{\perp}) waists

Parameters	Measured values
power reflectivity (f)	99.848(3) %
power reflectivity (c)	99.938(7) %
power transmissivity (f)	0.116(1) %
length	9.51(5) cm
free spectral range	$2\pi \times 3151(16)$ MHz
tangential waist	90.2(5) μm
sagittal waist	128.0(3) μm
mode volume	2.40(3) mm^3
single atom-photon coupling	$2\pi \times 91.5(5)$ kHz
linewidth (HWHM)	$2\pi \times 920(30)$ kHz
finesse	1710(60)

Table 3.1: Measured cavity parameters at 770.1 nm. Letters f and c in the parentheses stand for flat and curved mirrors, respectively. The indicated mode volume is for the TEM₀₀ mode and the linewidth specified here is for s-polarised light. All errors are standard deviations.

were deduced after l was measured, by an ABCD matrix calculation. Lastly, by using l and w_{\parallel} , w_{\perp} , the all-important volume²⁰ (V) for the TEM₀₀ was calculated.

Single-atom single-photon coupling strength

In order to calculate the single atom-photon coupling strength (g), the dipole moment (d) for the transition of interest (i.e. D₁ line) and the mode volume (V) are required as

$$g = d \sqrt{\frac{\omega_c}{2\hbar\epsilon_0 V}}.$$

For the D₁ line, $\lambda = 770.1$ nm [93] and the linewidth of the atomic transition $\gamma = 2\pi \times 2.978(6)$ MHz (HWHM) [86]. This gives $d = \frac{3\hbar\epsilon_0\gamma\lambda^3}{4\pi^2} = 2.905 e\alpha_0 = 2.462 \times 10^{29}$ Cm (e is the electron charge and α_0 the Bohr radius). As V is also known, we calculate $g = 2\pi \times 91.5(5)$ kHz.

²⁰The cavity mode volume is simply the volume integral over the normalised mode intensity.

Linewidth and finesse

We will now discuss the last two parameters of Table 3.1, the linewidth (κ) and finesse (\mathcal{F}). The two of them are intrinsically connected as $\mathcal{F} = FSR/2\kappa$. Both of these terms are crucial for cQED experiments as they provide a measure of the rate at which photons escape from the cavity. If κ is large, \mathcal{F} is small, meaning that photons do not live in the cavity for long. This is unwanted for experiments that need to operate in the strong coupling regime. We restrict our discussion here to measurements done with s-polarised light, for which κ (for our set of mirrors) is approximately 5 times smaller than for p-polarised light.

Monitoring κ (and thus \mathcal{F}) in regular time periods is necessary to ensure that the cavity mirrors remain clean, as the pressure in the vacuum chamber is expected to get higher with the regular use of the dispensers (as happened in a previous generation of the experiment). The least time-consuming and most straight-forward method available to us is to use the modulation already added to the current of the probe laser, and take a cavity transmission spectrum. Then, by using the known frequency separation between the probe and the sidebands, the cavity linewidth can be deduced. Figure 3.6 shows an example of a fitted cavity spectrum. Measurements on different days have not been very conclusive about the actual value of κ which was found to be between 1.14(12) MHz and 0.86(9) MHz, where error here is the standard deviation of 4 traces.

However, this method can be inaccurate and limited in the case where the linewidth of the probe laser is similar or higher than that of the cavity. Since in our case an actual measurement of the probe laser's linewidth has not been made (even though the laser is specified by TOPTICA for ~ 300 kHz), this particular measurement of the cavity linewidth is not necessarily valid. For this reason, we followed another approach to determine κ , which has no dependence on the relative linewidths of the laser and the cavity; the so-called ring-down technique [94].

The ring-down technique requires that a probe beam is on resonance with the cavity

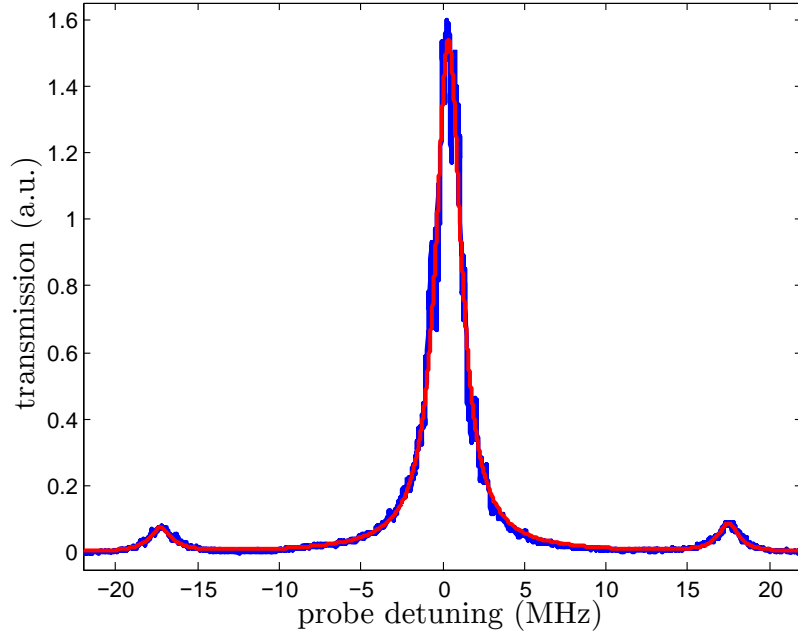


Figure 3.6: Example cavity transmission spectrum. Cavity transmission is in blue, and a Lorentzian fit to it is in red. The fit reveals $\kappa = 0.92(2)$ MHz where the number in the parenthesis is the standard error from the fit. The fit assumes that the two sidebands are at the same absolute frequency from the central cavity transmission peak. The modulation frequency here is 17.273 MHz.

and at a specific time is switched off using a fast optical switch (in this particular case, we use the double-passed AOM₂, shown previously in Figure 3.3b)). The cavity output is collected by a high-bandwidth detector²¹ (50 MHz), and a digital oscilloscope records the power $P(t)$ leaking out of the cavity. This relates to the lifetime of the photon inside the cavity τ_c and ultimately κ as,

$$P(t) = P_0 e^{-t/\tau_c} = P_0 e^{-2\kappa t} \quad . \quad (3.1)$$

Figure 3.7 shows an example of a cavity ring-down spectrum. In order to keep the probe on resonance, all the atom–cavity laser system’s locks were enabled. Because it takes ~ 40 ns for the AOM to completely switch off, it was chosen to fit the exponentially decaying curve starting at 80 % of its normalised transmission. The average of twelve traces gives $\kappa = 920(30)$ kHz (thus, $\mathcal{F} = 1710(50)$).

The two linewidth measurements show similar results. This indicates that either

²¹Thorlabs, APD110A-M

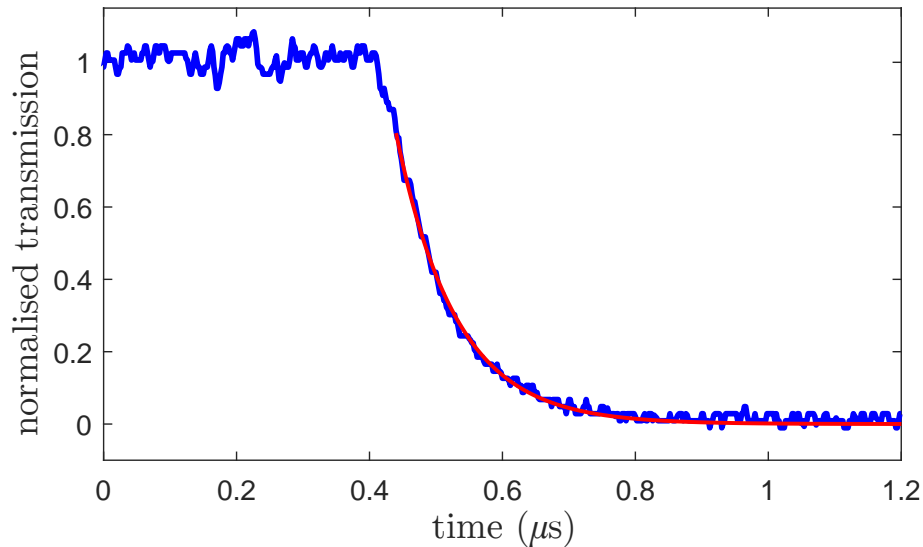


Figure 3.7: Cavity ring-down spectrum. The normalised cavity transmission curve is in blue, and the fit to the curve in red. Light begins to shut-off at $0.4 \mu\text{s}$.

method could be used in our experiment in order to monitor κ over time.

3.4 Magnetic field

The different parts that compose the vacuum system, the laser systems we use to stabilise lasers, cavities, and generate the MOT beams, and the beams necessary to probe the atoms in the cavity and study EIT, have been discussed in the previous sections. Here, the magnetic field configurations employed to make a 2D- and 3D-MOT, and issues related to mechanical oscillations induced by the switching of the current flowing through the 3D-MOT coils, are discussed.

3.4.1 2D-MOT field

Four rectangular coils (222 turns each) were made in order to produce the required 2D-MOT field geometry which has a zero-field line along which the atoms are cooled and trapped. When 2.5 A flows through each coil, a magnetic field gradient of 10 G/cm is created at the region of the 2D-MOT.

We found useful to connect the four coils to different power supplies and, with small adjustments of the current through each coil, to accurately position the 2D-MOT with respect to the graphite tube and the push beam, and thus optimise the 3D-MOT loading rate.

3.4.2 3D-MOT field

As a large atom number interacting with the cavity mode is beneficial for the experiment, it was firstly decided to employ a 2D- instead of the conventional 3D-quadrupole magnetic field, in order to make an elongated atomic cloud as in [95]. For a couple of reasons, this geometry did not work for us. First, it was found to be extremely difficult to overlap the elongated MOT with the cavity mode, as not only its position matters but its angle as well (giving four rather than two degrees of freedom, which is the case for a MOT which is not elongated). Secondly, even when the MOT was overlapped with the cavity and clearly elongated (Figure 3.8 shows a $\sim 5:1$ aspect ratio between the two axes), the number of atoms interacting with the cavity mode was only barely benefited as it is extensively discussed in Robert's thesis [80].

Since the first generation of coils failed to show any benefit by employing them, we chose to replace them with standard circular anti-Helmholtz coils (coils with current flowing in opposite directions with each other). Each coil consists of 60 turns of copper ribbon wire²². When 10 A flows through the coils, a magnetic field gradient of 8 G/cm in the strong vertical direction (and 4 G/cm in the other axes), is produced. One of the coils sits on the top of the science chamber while the other one is placed on three adjustable height 1.5" diameter posts²³ that were purchased in order to ease the procedure of horizontally aligning the 3D-MOT coils with respect to each other, and overlapping the 3D-MOT with the cavity mode (both horizontally and vertically). Both coils sit on layers of sorbothane to damp mechanical vibrations caused by switching on/off the current through the coils.

²²High Precision Foils, HP04-252.

²³Thorlabs, BLP01/M.

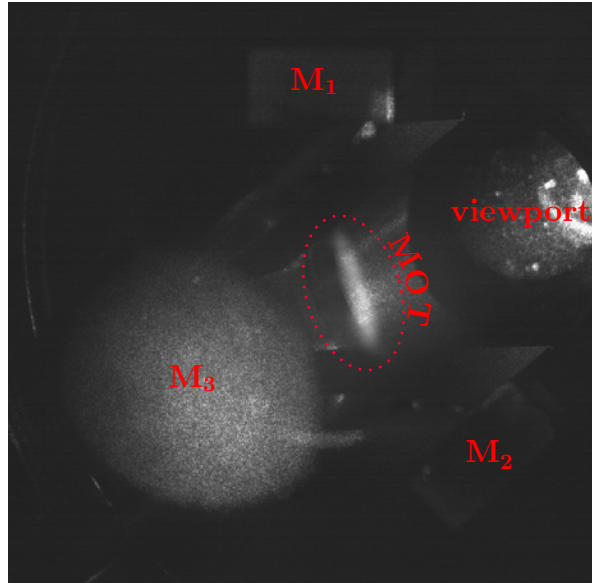


Figure 3.8: Photograph of the elongated MOT ($\sim 5:1$ aspect ratio) inside the old-generation cavity. Scattered MOT light from the top-bottom viewports blurs the photo. Bottom viewport is labelled.

The coils need to switch on and off quickly in the experiment as the magnetic field close to the atomic cloud is required to be near zero when looking for narrow EIT resonances, and aiming for atom clouds with very low temperatures. All the results that will be shown in this thesis were generated using the circular anti-Helmholtz coils.

Shutting on and off the coils

Replacing the unconventional 3D-MOT coils with a more standard version of them made our system much more compact and eased the procedure of overlapping the atomic cloud with the cavity mode. Furthermore, the new coils (in combination with other adjustments that will be discussed in Chapter 5) resulted in a MOT with higher atom number and optical depth. However, it was found that by switching off the current flowing through the coils, mechanical oscillations in the cavity frame were induced, which the cavity lock was not able to compensate for (fundamentally, the servo bandwidth has to be lower than the natural frequency, which gets excited during the shut-off). The oscillations last for seconds after the field shut-off (a very long time for our cold atom experiment).

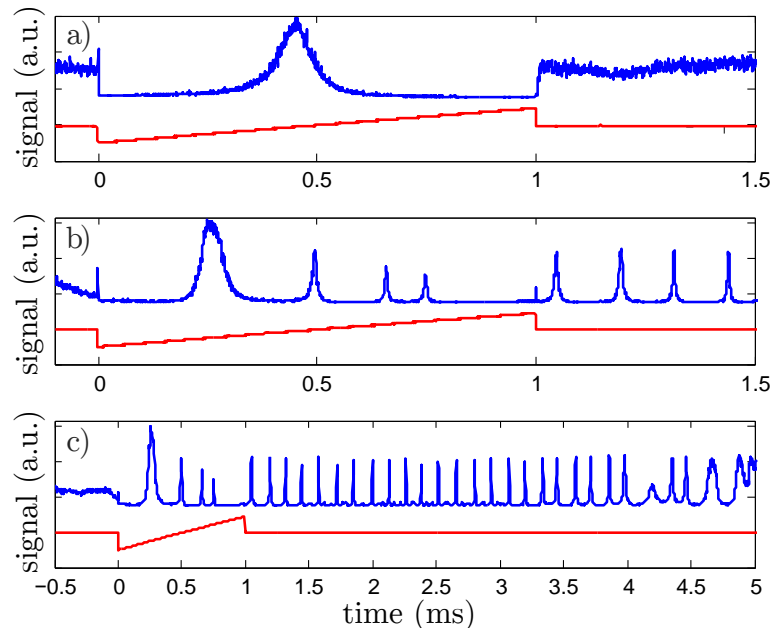


Figure 3.9: Coils' shut-off effect on the cavity. Cavity transmission and probe frequency ramp are in blue and red, respectively. The cavity is “locked” during the measurement. a) Current runs through the coils during the probe frequency scan. b) Coils are completely shut off when the probe frequency scan starts. Their shut-off is linear and takes $150 \mu\text{s}$. By the end of the probe scan, the coils are switched on again. c) Same events as in b), different timescale. Mechanical disturbances in the cavity remain for a long time after the coils are completely off.

The current through the coils was switched off using a relay switch²⁴ with $\sim 170 \mu\text{s}$ response time and $150 \mu\text{s}$ switch-off time. Figure 3.9 shows a cavity transmission spectrum, from which the response of the cavity after the coils were shut off can be examined. As can be seen in b) and c), once the current flow through the coils is disrupted, more than one resonance peak appears in the cavity transmission during the probe frequency scan or even for a long time after. Even when the current through the coils was slowly switched off (switching times on the order of 10 ms were also put into test), more or less the same spectra were obtained, with the amplitude of the peaks only slightly being reduced.

Mechanical vibrations caused by switching on and off the coils are partially damped by the sorbothane placed below the two coils, as previously mentioned. It is believed that eddy currents induced inside the vacuum chamber and/or the cavity frame are responsible for the remaining disturbance. The fact that the cavity is also rigidly mounted on the

²⁴Crydom, DC50D80.

bottom flange does not help any vibrations to be damped. In order to overcome this completely it may be necessary to re-design the cavity to isolate it from its frame or even to replace the spherical octagon with a chamber made out of glass.

As a first stage measure (after I left from the lab), Viton (low outgassing rubber) was placed inside a small gap just below the flex-mount to help damp vibrations. This seems to have helped to get a cleaner cavity transmission spectrum during the probe frequency scan (when the coils are shut off). All the measurements shown in this thesis are before the vacuum was broken and the viton piece was added.

Chapter 4

Electromagnetically induced transparency in an atomic vapour

The content presented here, such as figures and text, has partially been taken from [96]: A. Lampis, R. Culver, B. Megyeri and J. Goldwin, *Coherent control of group index and magneto-optical anisotropy in a multilevel atomic vapor*. *Optics Express* **24** (14), 15494–15505 (2016).

In this chapter, studies of EIT in a heated potassium vapour cell will be presented. The studies were done with an eye towards understanding better the EIT technique before implementing it on the cold, in-cavity atomic cloud in the main experiment. Since the generated results were particularly interesting, especially when an added longitudinal magnetic field was used to split the EIT feature, further investigations, for instance of magneto-optical anisotropy of the atomic system, were made.

We begin this chapter by giving some motivation on why EIT in potassium is interesting and presenting our experimental setup. We then show EIT generated resonances, with deeply sub-natural width, calculated to result to group indices larger than 6000. The last part of the chapter discusses how different relative polarisation configurations of the probe and coupling beams, involved in the formation of the EIT system, can lead to very

different magneto-optical activity.

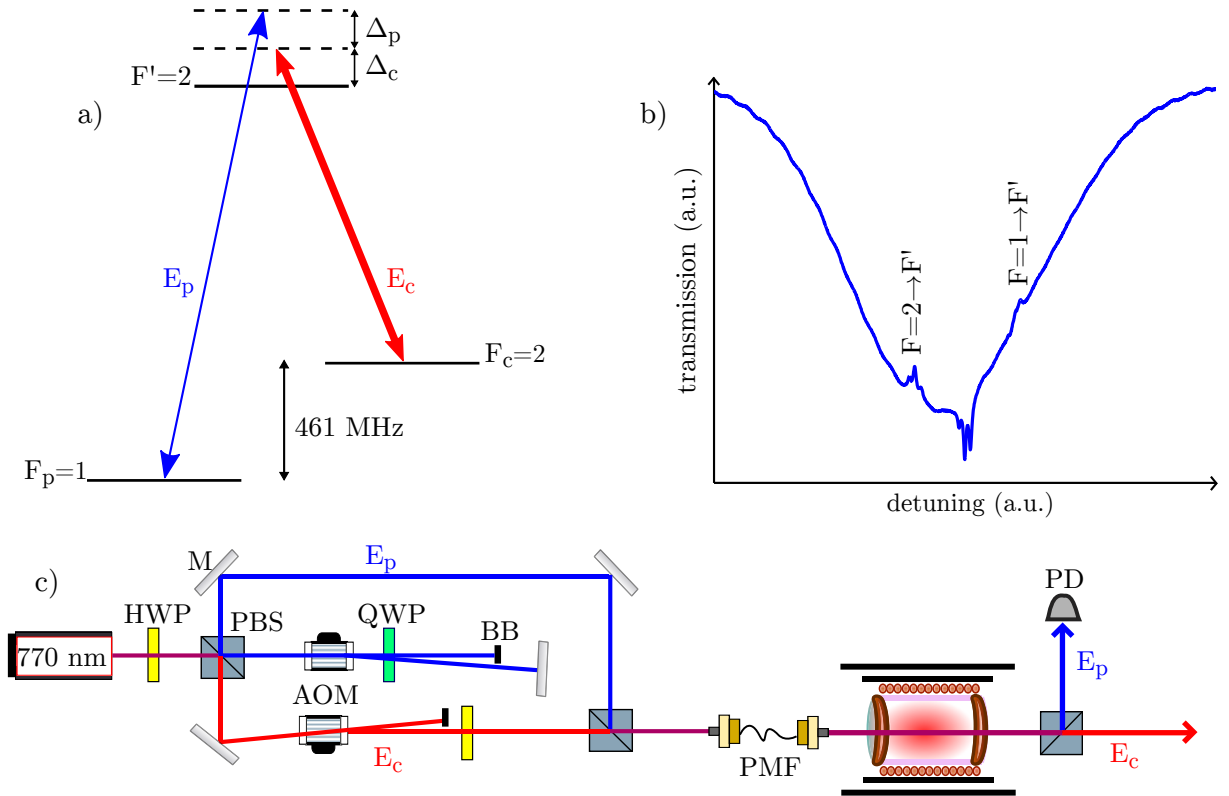


Figure 4.1: a) Simplified energy level diagram of the D_1 hyperfine transitions of ^{39}K used in this experiment. The coupling beam field E_c (red) is detuned by Δ_c from the $F' = 2$ excited state manifold, and the probe (E_p , blue) is detuned by Δ_p from Raman resonance. The $F' = 1$ here has been omitted for clarity and the ground state hyperfine splitting is taken from [93]. b) Saturated absorption spectrum i.e. with no coupling beam present. The Doppler profile and transitions that take place in a) are shown. Furthermore, the partially resolved features which are visible include the excited state crossover resonances whereas the dips in the transmitted signal, indicating increased absorption, are due to ground state crossovers. c) The experimental layout, which is described in detail in the text. M: mirror; HWP: half-wave plate, QWP: quarter-wave plate; PBS: polarising beam splitter; AOM: acousto-optic modulator; BB: beam block; PMF: polarisation-maintaining fibre; PD: photodiode.

4.1 EIT in potassium

Compared to other alkali metals such as rubidium and caesium, potassium is rather peculiar in the sense that its hyperfine splitting is especially small. More specifically, its ground states' hyperfine splitting is similar in frequency to the Doppler broadening

when we consider an experiment taking place in a heated vapour cell. Furthermore, the splitting between its excited states approaches its natural linewidth. These facts can cause complications in EIT and decrease the maximum attainable transparency as we can no longer control which atoms are effectively involved in the formation of EIT systems and which are only causing excess probe light absorption.

At the same time, we can use the small frequency splitting of the hyperfine levels of potassium in our favour. For instance, we can generate the probe and coupling beams simply by the use of an acousto-optical modulator and detect the coherent pair of beams simultaneously using a fast photodiode. This is in fact what we did in this experiment.

4.2 Experimental setup

We implement EIT on the D_1 ($4^2S_{1/2} \leftrightarrow 4^2P_{1/2}$) lines of potassium, shown schematically in Figure 4.1a). Due to the relatively small isotope shifts and hyperfine splittings all of the D_1 transitions for the naturally abundant potassium isotopes occur within a single Doppler-broadened profile (see Figure 4.1b)). Thus, inevitably the probe and coupling beams address multiple transitions. However, given the 93% abundance of ^{39}K and taking into consideration the oscillator strengths of the different transitions, we associate the probe with the dominant $F = 1 \leftrightarrow F' = 2$ manifold of ^{39}K transitions, and the coupling beam with $F = 2 \leftrightarrow F' = 2$.

The experimental setup is outlined in Figure 4.1c). Both the probe and coupling beams are derived from the output of an external-cavity diode laser running at a wavelength $\lambda = 770.1$ nm, part of the “atom-cavity” laser system described in Chapter 3¹. Most of the light is dedicated to the coupling beam and only a small fraction of the laser power is used for the probe. The coupling beam single-passes an AOM which allows us to turn it on and off instantaneously. The probe beam, after double-passing a different AOM, becomes 461.7 MHz blue detuned with respect to the coupling. We recombine the two beams

¹In Chapter 3, this is referred to as the potassium laser.

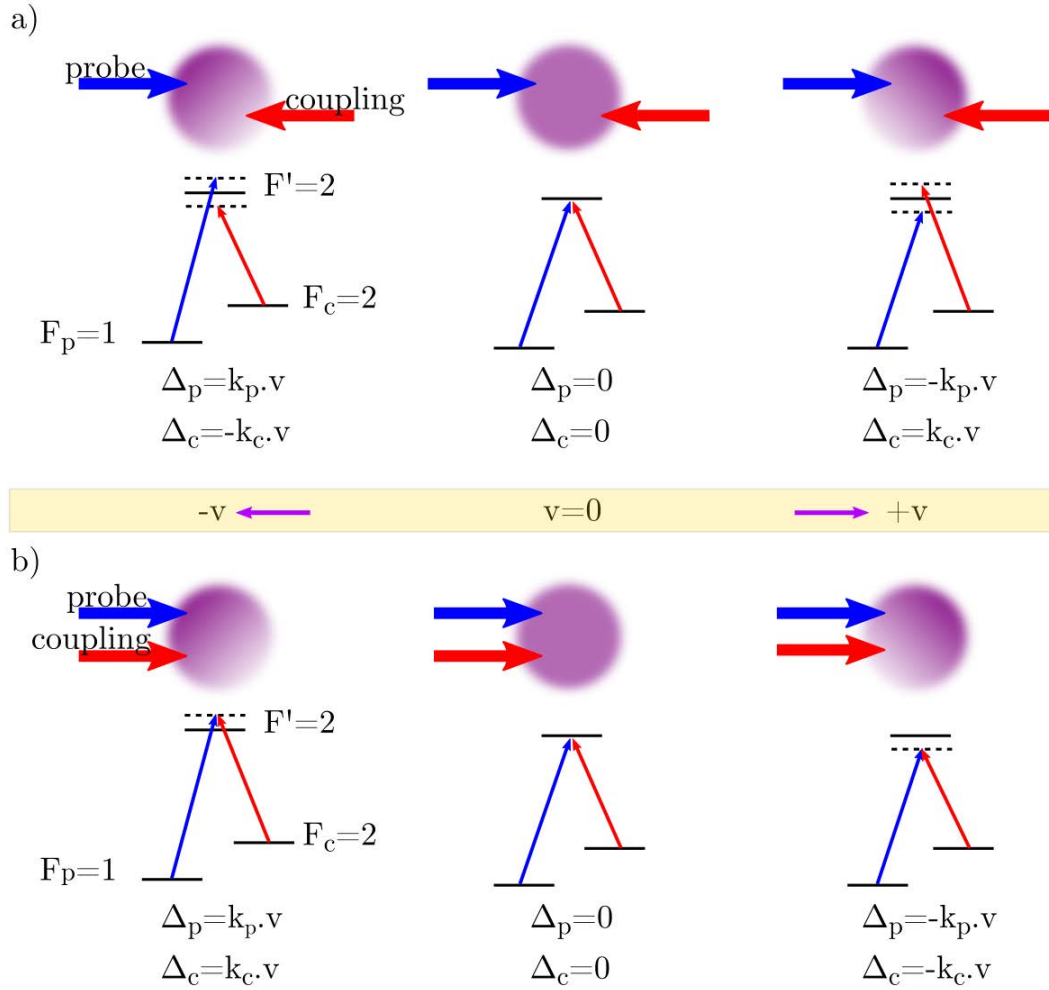


Figure 4.2: Doppler shift effect on the detunings of the probe (Δ_p) and the coupling beam (Δ_c). In a) the two beams are counter-propagating and the beams' frequencies are shifted by a different amount. Hence, not all the velocity classes of atoms contribute to the resulting EIT signal. b) The probe and coupling beams co-propagate, and their Doppler shifts cancel. Atoms from all different velocity classes do contribute to the EIT signal in this case. Similar explanation has been given by [97].

on a polarising beam splitter (PBS) and couple them into orthogonal axes of a single-mode polarisation-maintaining fiber (PMF). Then, the beams are collimated together out of the fiber to a $1/e^2$ intensity diameter of ~ 7.5 mm. As Figure 4.2 explains, since the probe and coupling beams are co-propagating, the two-photon EIT transition is effectively Doppler-free. In fact, from the ground-state hyperfine splitting, we calculate a broadening of 600 Hz which is negligible for even our narrowest features. Since the interference effect responsible for EIT does not depend on the detuning of the coupling beam Δ_c , a large

fraction of atoms can contribute to the signal, with very little dependence on the laser frequency. Actually, the relevant scale which is set by the typical single-photon Doppler width Δ_D , is on the order of $2\pi \times 400$ MHz half-width at half-maximum (HWHM). Therefore, we are able to make all of the measurements described here without any active stabilisation of the laser frequency.

The probe and coupling beams co-propagate through a commercial reference cell with an internal length of 70 mm and a natural abundance of potassium (no anti-relaxation coating or buffer gas). In order to control the vapour pressure and prevent condensation of potassium on the windows, we make use of thin-foil resistive heaters² with integrated temperature sensor, at each end of the cell. The heaters were found to be producing some stray magnetic fields (as we show in Figure 4.3), thus, we found it necessary to momentarily turn off the currents during measurements in order to obtain the best transparency features. The assembly was placed within an aluminium lens tube with anti-reflection-coated windows and wrapped in thermal insulation. A solenoid was also wound around the lens tube in order to have better control of the longitudinal magnetic field in the cell. The system was placed into a 24 cm long, two-layer cylindrical mu-metal shield (without end caps). The probe and coupling beams were separated after the cell by another PBS, and the probe power was detected with a biased photodiode whose output current was loaded by the $1\text{ M}\Omega$ input impedance of a digital oscilloscope.

4.3 Transparency linewidth, absorption coefficient and group index

Figure 4.3a) shows an example EIT resonance. The laser is tuned so that the probe is near resonance with the $F = 1 \rightarrow F' = 2$ transitions (as seen by atoms at rest in the lab frame), and the two-photon detuning Δ_p is swept with a voltage-controlled oscillator

²Thorlabs, HT10K.

(VCO) driving the AOM. The power of the coupling beam at the entrance of the cell is $700 \mu\text{W}$, whereas for the probe beam it is just $50 \mu\text{W}$ (far below saturation). The fractional transmission, defined as the ratio of change in absorption of the probe when a coupling beam is also present to the absorption of the probe when no coupling beam is present, varies from ~ 4 to 17% over a frequency range which is much narrower than the natural linewidth $\gamma = 2\pi \times 2.98 \text{ MHz}$ [86]. If we would like to have a complete theory for the lineshape of the EIT resonance, we should take into consideration the presence of multiple Λ subsystems, effects like Doppler and transit-time broadening³, as well as variations in the intensity of the coupling beam over the full cell volume. However, all of the EIT signals we observe are described well by simple Lorentzian functions of detuning, which we thus choose to use for simplicity.

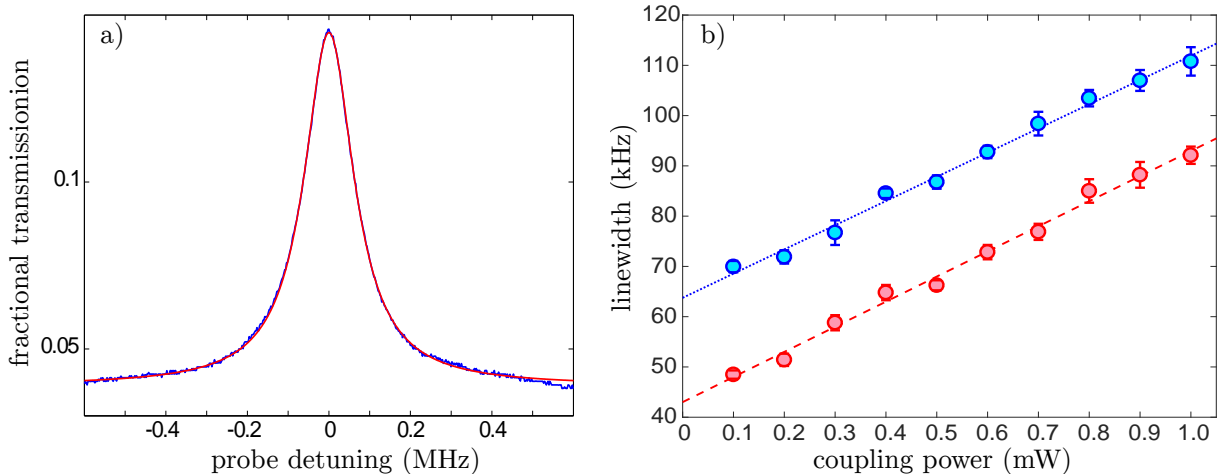


Figure 4.3: a) Example EIT feature, showing the fractional transmission through the cell at a temperature of $74 \text{ }^\circ\text{C}$. The coupling (probe) beam power is at 700 (50) μW at the entrance of the cell. Data are shown in blue and the red curve shows a Lorentzian fit, which gives a HWHM of $2\pi \times 76.9 \text{ kHz}$. b) EIT linewidth (HWHM) for varying coupling beam power. Points are fits from the data such as in a) and averaged over six traces for each power. For the red (blue) data, the heaters were turned off (on) during the measurement. The straight lines are a fit to equation 4.1. The fit gives a dephasing rate of $2\pi \times 43(1) \text{ kHz}$ and $2\pi \times 64(2) \text{ kHz}$ for the red and blue data, respectively. Error bars here show standard deviations.

Figure 4.3b) shows the EIT linewidth as a function of coupling beam power. The

³This effect arises as a consequence of the finite interaction time of the atoms with light. This in its turn causes a spread in frequencies which is proportional to the atomic velocity and inversely proportional to the beam diameter [98].

(additional) broadening of the EIT feature of approximately 20 kHz when the heaters were left on during the measurement is also shown. Despite the aforementioned theoretical complications, a simple linear model was found to be adequate to describe the data,

$$\Gamma_{\text{EIT}} = \gamma_{21} + \frac{\Omega_c^2}{W} . \quad (4.1)$$

Here, γ_{21} represents dephasing between the two ground states, Ω_c is the coupling beam Rabi frequency, which is proportional to the square root of optical intensity, and parameter W characterises the total decoherence and broadening (the excited state decay rate and Doppler broadening Δ_D contribute to its value). We will restrict our discussion to results for which the heaters were momentarily turned off during the measurement. For those, equation 4.1 yields $\gamma_{21} = 2\pi \times (43.0 \pm 1.0)$ kHz (HWHM), which is 70 times narrower than the natural linewidth. We calculate $\sim 2\pi \times 11$ kHz contribution from the transit-time across the beams [99] (see Appendix B.1). The remainder, we find consistent with estimations of 1.2 μT magnetic field variations over the volume of the beams arising from the fact that our magnetic shield has no end caps. In order to determine W , we calculate Ω_c^2 from the mean optical intensity averaged over the transverse profile of the coupling beam at the entrance to the cell [69]. In this calculation we also take into account a 1/6 factor to average over the $F = 2 \leftrightarrow F' = 2$ oscillator strengths. The result is $W = 2\pi \times (67 \pm 2)$ MHz, which is about six times smaller than the Doppler width. This contradicts the prediction by [100], stating that $W \gtrsim \Delta_D$. We believe that the small excited splitting in ^{39}K leads to some scattering from the coupling on the $F = 2 \leftrightarrow F' = 1$ transitions, leading to an increased saturation intensity, hence reduced optical pumping efficiency.

In addition to the narrow EIT features, we also obtain large group indices of refraction using our setup. For a phase index n , which depends on the probe frequency ω_p , we can define the group index n_g as,

$$n_g = n + \omega_p \frac{dn}{d\omega_p} . \quad (4.2)$$

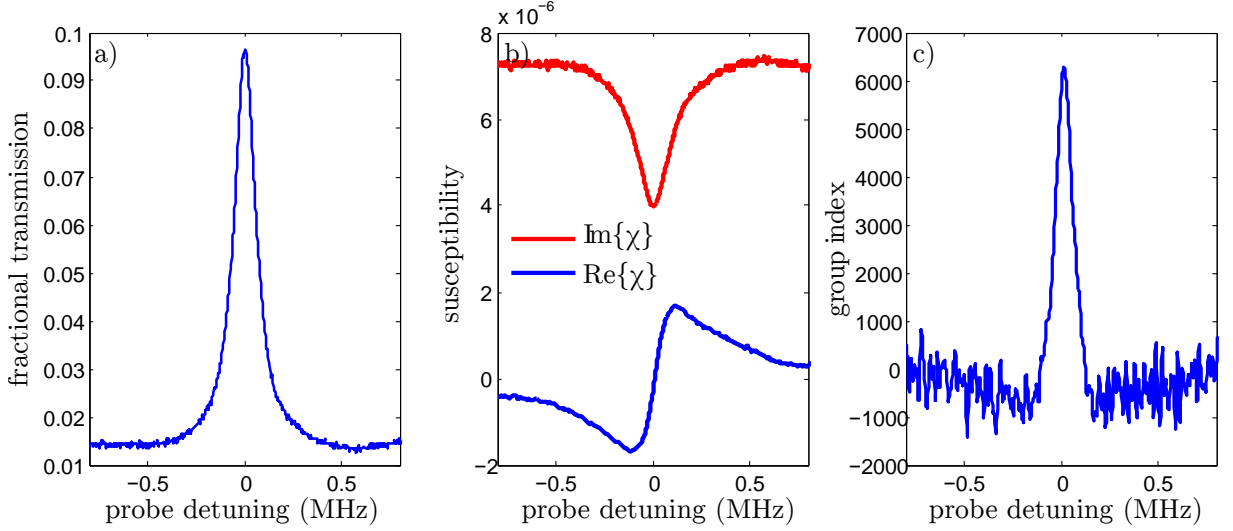


Figure 4.4: Determination of the group index from a transmission spectrum. a) Fractional transmission spectrum $T(\omega_p)$ for coupling (probe) power of 300 (50) μW and a cell temperature of 84 $^\circ\text{C}$. b) Real (blue) and imaginary (red) parts of susceptibility, obtained from spectrum a) and as described in the text. c) The group index of refraction n_g of the gas as obtained by the numerical derivative of $[1 + \chi(\omega_p)]^{1/2}$. The analysis for these conditions gives a peak group index of 6330(160), averaged over three spectra.

In order to determine n_g for our spectra, we apply a method recently demonstrated with Doppler-broadened media, in the absence of the EIT resonance (i.e. $E_c = 0$) [101]. As in that study, our EIT medium is described by a complex susceptibility $\chi(\omega_p) = \chi' + i\chi''$, describing the linear response with respect to the probe. As the probe traverses through the cell, it picks up a phase shift proportional to χ' (the real part), with $\chi' = n^2 - 1$. At the same time, any absorption experienced by the probe is proportional to $\chi'' > 0$ (imaginary part), or equivalently the absorption coefficient $\alpha = k\chi''$, where $k = 2\pi/\lambda$ is the wavenumber. The fractional probe power transmission through an atomic medium of L length and α can be written as:

$$T(\omega_p) = e^{-\alpha(\omega_p)L} \quad . \quad (4.3)$$

We should understand the response of the EIT medium under consideration to be linear in E_p , but nonlinear in E_c . E_c varies throughout the cell volume due to the absorption along the propagation axis and the intensity profile which is Gaussian. Thus, when we apply the method explained in [101], we must realise that χ represents the susceptibility

averaged over the entire volume of the cell and weighted by the transverse intensity profile. Then, $\chi(\omega_p)$ can just be calculated from probe transmission measurements, according to equation 4.3. The medium obeys causality, thus we can relate χ' and χ'' via the Kramers-Kronig relations. More specifically, we can obtain $\chi'(\omega_p)$ by Hilbert transforming $\chi''(\omega_p)$. Then, by numerically differentiating $n(\chi'(\omega_p))$ we calculate $n_g(\omega_p)$, using equation 4.2. Figure 4.4 shows an example of this analysis. The particular results imply that a pulse of light can propagate through the cell with a group velocity $v_g = c_0/n_g$ which is more than 6000 times slower than the vacuum speed of light, c_0 .

As mentioned previously, since the probe and coupling beams are co-propagating, we can observe a transparency feature around zero Raman detuning ($\Delta_p = 0$), independent of Δ_c . Three additional transmission spectra are shown in Figure 4.5a), for a cell temperature of 84°C, 300(50) μ W coupling (probe) beam power at the cell entrance, and a selection of the single-photon detuning Δ_c . In trace C, Δ_c is tuned so that the probe is approximately at the centre of the single-photon Doppler profile shown in Figure 4.1b), in order to have the strongest background absorption. Over a frequency range of $2\pi \times 62$ kHz, the fractional transmission in C varies by 8 %. For A and B, although the spectra were chosen to have similar α outside of the EIT resonance, the heights of the peaks are significantly different. When the probe is blue-detuned, as in trace A, probe and coupling are near resonance with the transitions shown in Figure 4.1a) in the lab frame, resulting in optimum EIT. On the contrary, when the probe is red-detuned, as in trace B, the probe absorption is dominated by high-velocity atoms in the $F = 2$ (wrong) ground state. These atoms see the probe beam red-shifted into resonance and to form a Λ system, the coupling beam needs to be addressing the $F = 1 \leftrightarrow F'$ transitions. Obviously, only a very small fraction of atoms participate in the formation of a Λ system in this case and excess probe absorption only leaves a small EIT feature.

We measured n_g for varying laser detuning, at multiple cell temperatures and a sample of them are shown in Figure 4.5b). The upper branch, for each set of data, corresponds to probe detunings on the blue side of the Doppler profile. In this regime, n_g is proportional

to α for all different temperatures, as shown by the linear fit (dashed line). This happens as when off-resonant absorption is negligible, the group index should be proportional to the absorption coefficient. On the red side, the group index is much smaller for a similar absorption coefficient, showing the single-photon absorption effects. We observe the peak group index monotonically increasing with the cell temperature until $\sim 90^\circ\text{C}$. After exceeding this temperature, the maximum achievable n_g is reduced as a result of the excessive absorption of the coupling beam. We thus decided to keep the cell at 84°C for the rest of the experiments we describe here.

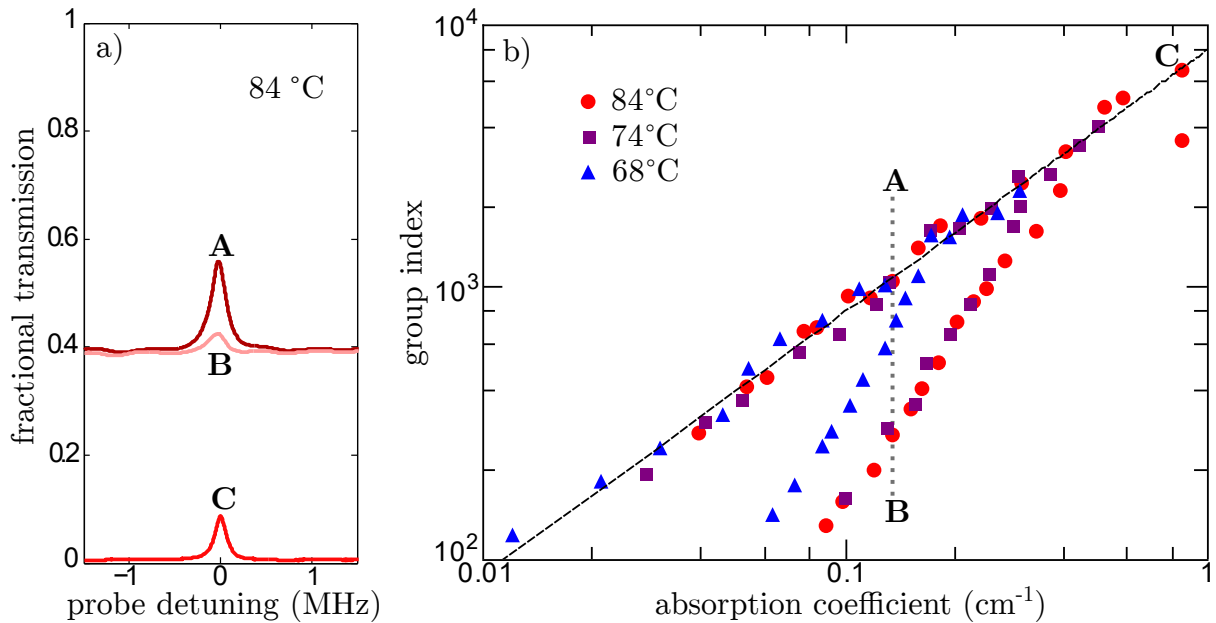


Figure 4.5: Absorption and group index. a) Fractional transmission spectra $T(\omega_p)$ for coupling (probe) power of 300 (50) μW and a cell temperature of 84°C . The background absorption coefficient is varied by coarse tuning of the laser. The linewidth of the three example EIT features are $2\pi \times (86, 88, 62)$ kHz and the amplitude (16, 3, 8) %, for the traces A, B and C, respectively. b) The effect of optical depth on the group index. For each different cell temperature, the group index is measured by varying the detuning Δ_c . This leads to varying background probe absorption (i.e. just outside the EIT resonance). The upper branches correspond to probing on the blue sides of the Doppler profile near the $F_p \rightarrow F'$ transition, and the bottom halves on the red side near $F_c \rightarrow F'$. The black dashed line shows the linear dependence expected for simple EIT.

4.4 Magneto-optical anisotropy

When a longitudinal magnetic field is applied, we observe the EIT resonance splitting into three distinct components, as can be seen in Figure 4.6. Such splitting of EIT and related features was the subject of early studies [102, 103] and interest in this phenomenon has continued [104–106]. The location of the central peak does not depend on the field magnitude, while the side peaks tune with effective magnetic moments of ± 1 Bohr magneton ($\mu_B = 2\pi\hbar \times 14 \text{ kHz}/\mu\text{T}$). This occurs as a result of the Zeeman shift that perturbs the ground states energies by $g_F m_F \mu_B B$ where m_F is the projection of F , and the Landé g -factor g_F equals $+1/2$ for the F_c manifold and $-1/2$ for F_p . It should be noted that since the EIT resonance condition is independent of the coupling beam detuning Δ_c , shifts to the excited states do not matter ($g_{F'} = \pm 1/6$ for the F' states). For linear polarisations, both probe and coupling fields can be decomposed along the B -field axis into superpositions of left- and right-handed circular polarisations. Thus, every Λ system contributing to EIT connects pairs of $\Delta m_F = 0$ or ± 2 , giving frequency shifts of 0 or $\pm \mu_B B/\hbar$.

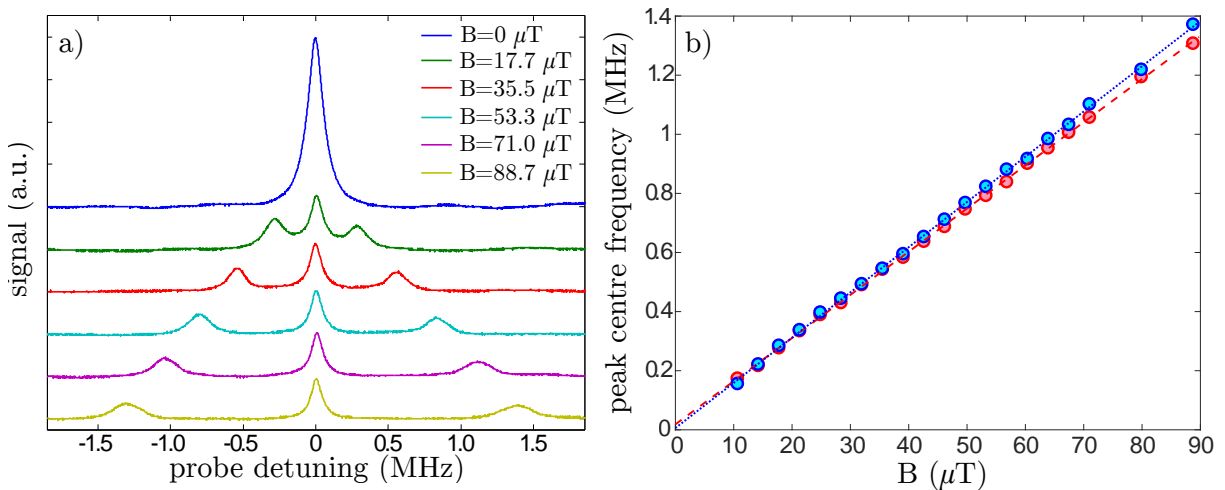


Figure 4.6: Effect of the added longitudinal magnetic field. a) The EIT resonance is split into three components. The central one is always centred at zero probe detuning ($\Delta_p = 0$) and the side peaks shift with effective magnetic moments of ± 1 Bohr magneton. Spectra have been shifted vertically for clarity. b) Left (red) and right (blue) peaks' centre frequency plotted with respect to the added magnetic field.

In addition to the shift in resonance frequency, we observe a narrower central EIT peak,

as shown in Figure 4.7. Specifically, the peak becomes as much as 1.4 times narrower when longitudinal magnetic fields of $52 \mu\text{T}$ and higher are applied. In fact, this is two orders of magnitude lower field than what was required in [106] to achieve the same 1.4 narrowing factor. The narrowing is basically a consequence of the three peaks getting completely separated from one another. Furthermore, we observed a broadening of the side peaks in our measurement that was different for the two side peaks by up to 50 kHz. We believe that the dominant reason for this effect in our system is the inhomogeneous magnetic field produced by the solenoid which is not longer than the cell.

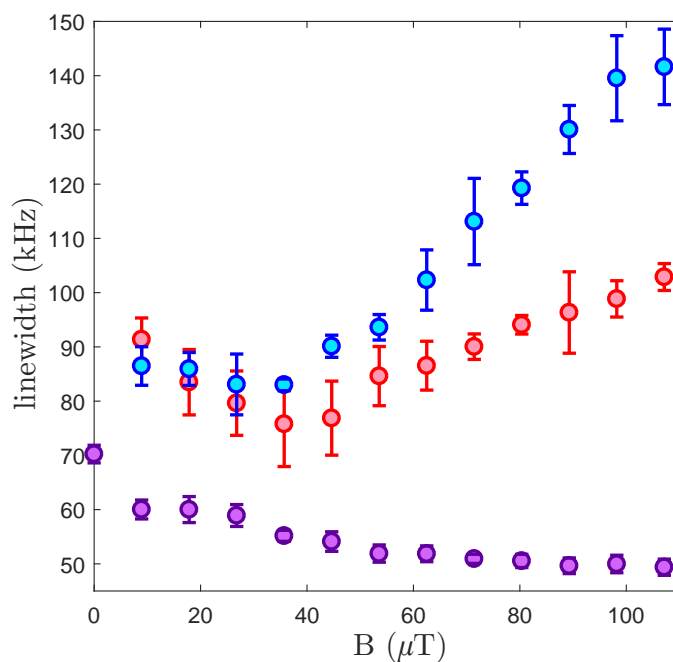


Figure 4.7: The width of the central and side EIT peaks as a function of the added longitudinal magnetic field. The central peak (purple) gets narrower as the field is being increased while the left (red) and right (blue) side peaks get broader due to the inhomogeneous field produced by the solenoid. Error bars here represent standard deviations.

We know that the central peak shows no anisotropy. However, it is interesting to ask whether the side peaks, which are not uniquely associated with either σ^\pm , exhibit circular dichroism (CD) and birefringence (BIR). We shall define the two phenomena. CD happens when the two circularly polarised components of the linear probe experience different absorption ($\Delta\alpha$), which causes the light to become elliptical after propagating through the atomic medium. On the other hand, BIR occurs when the two probe polarisation

components acquire different phase shifts ($\Delta\phi$), due to the different refractive indices they might experience, leading to the rotation of the probe polarisation plane [107]. Another question one might ask is whether the different relative polarisations of the probe and coupling beams result to a magneto-optical anisotropy of the same magnitude. This question became even more interesting for us after detecting the two beams directly after the vapour cell (i.e. before the PBS which separates horizontal from vertical polarisations – see Figure 4.1c)). As Figure 4.8 shows, the signal when the linear probe and coupling beams had perpendicular relative polarisation ($\text{lin}\perp\text{lin}$) was almost 2 times larger than when the two beams had the same relative polarisation ($\text{lin}\parallel\text{lin}$). Furthermore, the height of the three peaks as the magnetic field was being increased was very different for the two configurations. Specifically, the central peak for the $\text{lin}\perp\text{lin}$ case was constantly larger than the two side peaks while for the $\text{lin}\parallel\text{lin}$ case the central peak had almost the same height as the side peaks. Since the probe and coupling beams were overlapped using orthogonal polarisations, we added a polariser at 45° before the cell in order to obtain $\text{lin}\parallel\text{lin}$, and we increased the incident light power so that we had the same power entering the cell for both configurations. Studies of coherent control of polarisation rotation in Λ systems with and without magnetic field have been done in cold lithium [108], caesium [109], and rubidium [110] and also, in heated rubidium [111] and sodium [112] vapours.

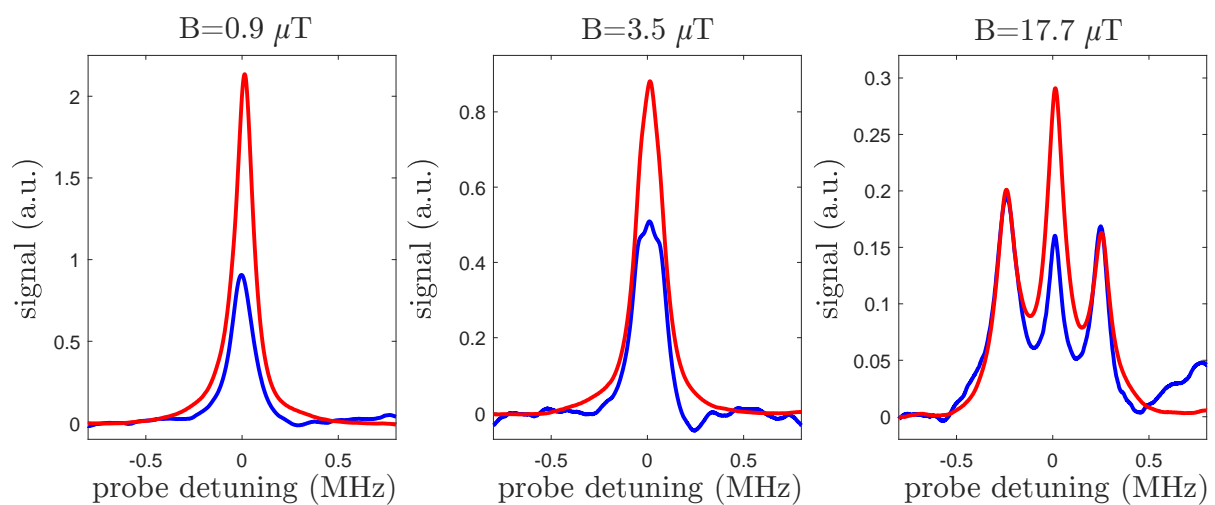


Figure 4.8: EIT signals for the $\text{lin}\parallel\text{lin}$ (blue) and $\text{lin}\perp\text{lin}$ (red) configurations for different applied magnetic fields.

In Λ systems, where the wavelengths of the probe and coupling beam are similar, polarisation rotation measurements typically require some relative misalignment of the probe and coupling beams to prevent the latter to enter the polarimeter. In the measurement we are doing here, we prefer not to sacrifice our configuration which is compact, robust, and essentially Doppler-free. Instead, we have developed a new measurement of magneto-optical activity which exploits the fact that our beams are spatially mode-matched. A simplified schematic of our detection setup is shown in Figure 4.9. A quarter-wave plate (QWP), with its fast axis at 45° from horizontal, converts right- and left-hand circular polarisations to vertical and horizontal, respectively. In the language of Jones vectors [69],

$$\begin{pmatrix} \mathbf{e}_r \\ \mathbf{e}_l \end{pmatrix} \xrightarrow{\text{QWP}} \begin{pmatrix} \mathbf{e}_v e^{-i\pi/4} \\ \mathbf{e}_h e^{i\pi/4} \end{pmatrix}, \quad (4.4)$$

where \mathbf{e}_r and \mathbf{e}_l are the basis vectors for right- and left-handed circular polarisations (RHC and LHC, respectively), which are related to horizontal (h) and vertical (v) polarisations by $\mathbf{e}_r = (\mathbf{e}_h - i\mathbf{e}_v)/\sqrt{2}$ and $\mathbf{e}_l = (\mathbf{e}_h + i\mathbf{e}_v)/\sqrt{2}$.

After the waveplate, the horizontal and vertical components of both probe and coupling beams are separated on a PBS and sent to two high-speed photodetectors⁴, biased at +5 V with bias-tees⁵. Following, the two microwave beat notes are amplified by 24 dB⁶, and then sent to the inputs of an integrated chip gain/phase detector⁷, whose outputs are described below.

In order to calculate the detected signal, we first take into consideration the propagation of the probe beam. It is assumed that the incident field takes the form $\mathbf{E}_p = \mathbf{e}_h E_p \exp(-i\omega_p t)$. After the cell,

$$\mathbf{E}_p(\text{after cell}) = \frac{E_p e^{-i\omega_p t}}{\sqrt{2}} \left(\mathbf{e}_r e^{-\alpha_r L/2} e^{i\phi_r} + \mathbf{e}_l e^{-\alpha_l L/2} e^{i\phi_l} \right), \quad (4.5)$$

⁴Hamamatsu, G1476-03.

⁵Mini-Circuits, ZFBT-4R2GW+.

⁶Mini-Circuits, ZFL-500LN+.

⁷Analog Devices, AD8302-EVALZ.

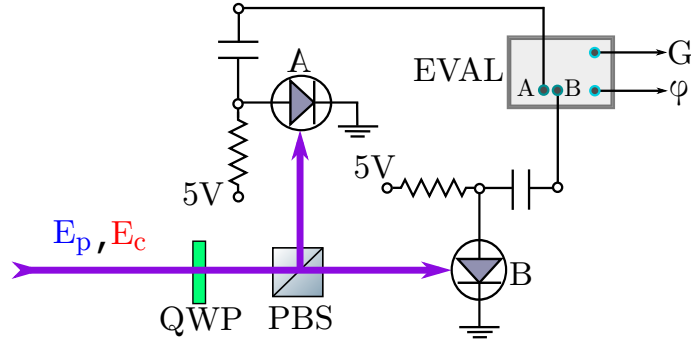


Figure 4.9: Simplified schematic for heterodyne measurements of optical anisotropy. The quarter-wave plate (QWP) and polarising beam splitter (PBS) act together as a circularly polarising beam splitter according to equation 4.4. The probe (E_p) and coupling (E_c) beam components interfere at the fast photodiodes A and B, and the resulting beat notes are used as inputs to a gain/phase detecting circuit (EVAL) as described in the text.

where the absorption coefficient for ζ -handed circular polarisation is represented by α_ζ and ϕ_ζ is the corresponding phase shift which is related to the phase index by $\phi_\zeta = kLn_\zeta$. After the QWP,

$$\mathbf{E}_p(\text{after QWP}) = \frac{E_p e^{-i\omega_p t}}{\sqrt{2}} \left[\mathbf{e}_v e^{-\alpha_r L/2} e^{i(\phi_r - \pi/4)} + \mathbf{e}_h e^{-\alpha_l L/2} e^{i(\phi_l + \pi/4)} \right] . \quad (4.6)$$

We assume the coupling beam to be of the same form as the probe, $\mathbf{E}_c = \mathbf{e}_\xi E_c \exp(-i\omega_c t)$, with polarisation ξ . The polarisation configuration of the beams when $\xi = v$, is said to be $\text{lin}\perp\text{lin}$, and $\text{lin}\parallel\text{lin}$ in the case that $\xi = h$. Since the probe and coupling beams are overlapped using orthogonal polarisations, $\text{lin}\perp\text{lin}$ is the default configuration, whilst $\text{lin}\parallel\text{lin}$ can be obtained by adding a polariser at 45° before the cell. In order to have the same power entering the cell for both configurations, we increase the incident light power. Given the relative coupling and probe beam powers, we make the assumption that both the absorption coefficient α_c and phase ϕ_c for the coupling beam do not depend on Δ_p , for a fixed value of Δ_c . We also take $\phi_c = 0$, without loss of generality. Thus,

$$\mathbf{E}_c(\text{after QWP}) = \frac{E_c e^{-i\omega_c t}}{\sqrt{2}} \left[\mathbf{e}_v e^{-\alpha_c L/2} e^{\mp i\pi/4} + \mathbf{e}_h e^{-\alpha_c L/2} e^{\pm i\pi/4} \right] , \quad (4.7)$$

where the upper (lower) symbol refers to $\text{lin}\parallel\text{lin}$ ($\text{lin}\perp\text{lin}$) configuration. After the PBS,

the beat notes which are proportional to $2\text{Re}(\mathbf{E}_p \cdot \mathbf{E}_c^*)$ are detected,

$$\text{LHC}(h \text{ after PBS}) = E_p E_c e^{-(\alpha_l + \alpha_c)L/2} \frac{\cos(\delta\omega t - \phi_l)}{\sin(\delta\omega t - \phi_l)} \quad (4.8)$$

$$\text{RHC}(v \text{ after PBS}) = \pm E_p E_c e^{-(\alpha_r + \alpha_c)L/2} \frac{\cos(\delta\omega t - \phi_r)}{\sin(\delta\omega t - \phi_r)} \quad , \quad (4.9)$$

where $\delta\omega = \omega_p - \omega_c$ is the beat note frequency. Then, the two AC signals from the photodiodes are sent to the input channels, A and B, of the gain/phase detector. Following, the board generates two voltage outputs: a) one which is linear in the logarithm of the A/B amplitudes ratio and b) one which is linear in the phase difference. More specifically,

$$\text{amplitude ratio: } V_G = 0.9V - 0.6V \left(\frac{\Delta\alpha L}{2 \ln 10} \right) \quad (4.10)$$

$$\text{phase difference: } V_\phi = 0.9V - 1.8V \left(\frac{|\Delta\phi| - \pi/2}{\pi} \right) \quad . \quad (4.11)$$

Here, $\Delta\alpha = \alpha_r - \alpha_l$ characterises CD, and $\Delta\phi = \phi_r - \phi_l$ defines BIR (as previously discussed). Equations 4.10 and 4.11 imply that our measurement produces voltages which are linear in the differential absorption as well as phase shift between circular polarisation components. Furthermore, it does not require normalising to the full transmission and since the two beams propagate together, a strong common-mode rejection of phase noise due to mechanical vibrations exists.

Figure 4.10, shows example spectra from the measurement. The detuning Δ_c and power of the coupling beam (1 mW) were specifically chosen to give maximum dichroism at large fields. The probe was once again set to 50 μW . It was found that $\Delta\phi$ was too small to be measured directly, due to the higher noise level of the output of the phase channel. Thus, in practice, we only have used equation 4.10 in our experiment and $\Delta\phi$ spectra were generated by Hilbert transforming $\Delta\alpha$, in the spirit of what we have described in the previous section.

We observe a systematically 2-3 times greater magneto-optical anisotropy of the EIT medium for the lin||lin polarisations than for the lin \perp lin. Furthermore, we see that $\Delta\alpha$ is of order $\alpha/10$ for lin||lin polarisations. This is also accompanied by a polarisation rotation

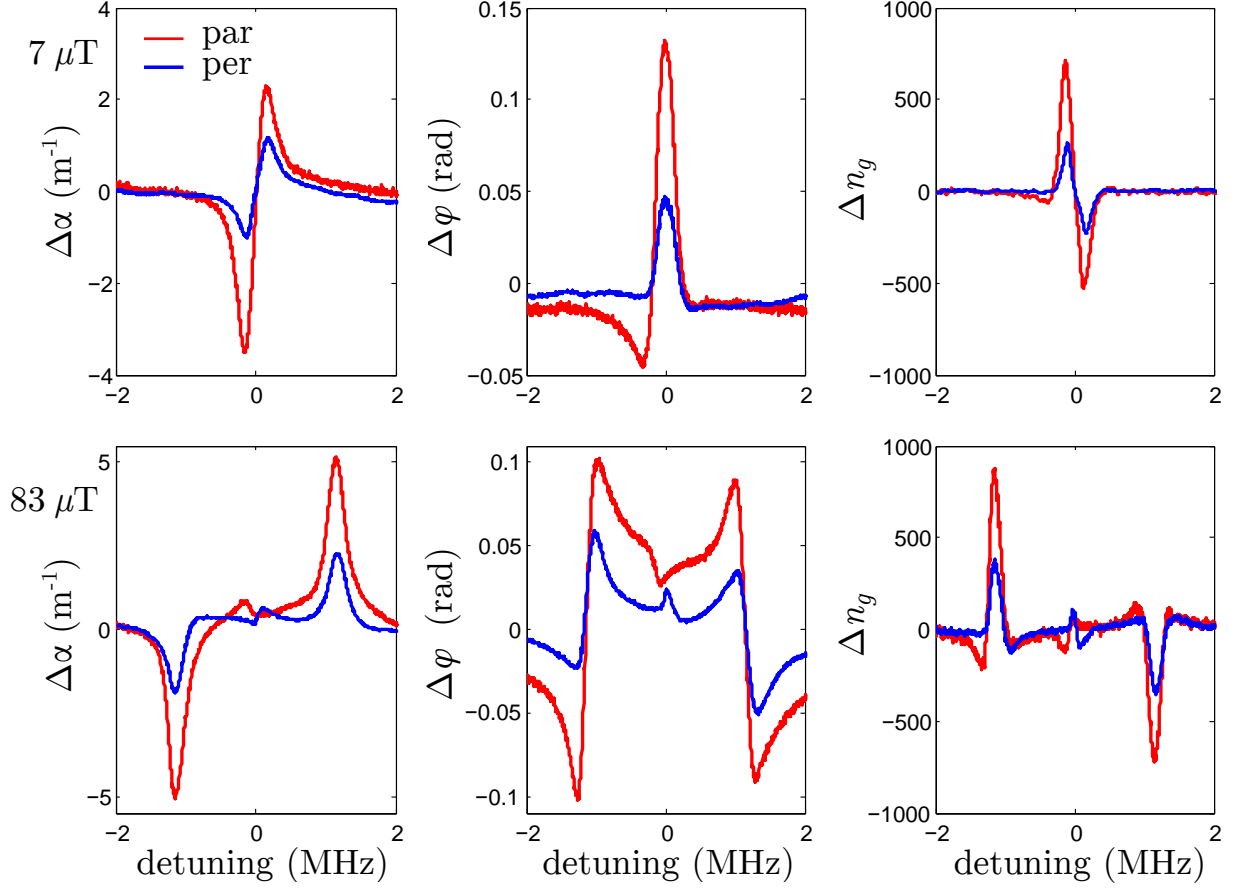


Figure 4.10: Heterodyne spectra of magneto-optically induced anisotropy. Red (blue) traces show the results for lin||lin (lin⊥lin) polarisations. The figures show the differential absorption coefficient $\Delta\alpha$, the phase difference $\Delta\phi$ (obtained by Hilbert transformation of $\Delta\alpha$), and the group index difference Δn_g (obtained by numerical differentiation of $\Delta\phi$ and then smoothed with the *sgolayfilt* filter in Matlab) as a function of the probe detuning.

angle,

$$\theta = \frac{kL}{2}\Delta n = \Delta\phi/2 \sim 70 \text{ mrad} \quad , \quad (4.12)$$

where Δn is the difference in refractive indices for right- and left-hand-circularly polarised components of the probe. From θ , we can approximate the Verdet constant \mathcal{V} , an optical constant providing a measure of the rotation of the probe polarisation plane, by [107]:

$$\mathcal{V} = \frac{1}{L} \frac{d\theta}{dB} \sim 1.5 \times 10^5 \text{ rad}/(\text{Tm}) \quad . \quad (4.13)$$

Additionally, the difference in group index implies a relative delay of $\Delta t = \Delta n_g L/c \sim 200 \text{ ns}$ between RHC and LHC components.

The measured difference between the two polarisation configurations can be attributed

to magneto-optical coherence. The probe and coupling beams, since linearly polarised, each represent RHC and LHC light superpositions. Only the relative phases of the components are different between $\text{lin}\|\text{lin}$ and $\text{lin}\perp\text{lin}$. These phases only have an important role to play in the EIT medium anisotropy if the probability amplitudes that describe scattering within individual Λ systems add coherently. It should be stressed that it is not *a priori* clear why this should actually be the case. In fact, in a previous study [102], where the splitting of coherent population trapping resonances were investigated, it was found that the total signal was an incoherent sum of the contributing subsystems. However, other EIT experiments have shown non-trivial and unexpected results ascribed to the coherence between the involved scattering channels [113–115]. Similarly, our results clearly demonstrate a dependence on the relative phase of the RHC and LHC polarisations. The results highlight the important role of coherence in the generation of magneto-optical anisotropy. This, to the best of our knowledge, has not been observed before.

4.4.1 Theory model

A very simple model was employed in order to generate theory spectra for our system. It should be noted that the purpose of this model was only to capture the essential difference between the two polarisation configurations, as shown in the experimental results, not to accurately reproduce the spectra.

To model the EIT medium, we begin with the susceptibility for a single Λ system, which can be written as [74]:

$$\chi = i \frac{\mathcal{N} d_{31}^2}{\hbar \epsilon_0} \frac{\gamma_{21} - i \Delta_p}{|\frac{1}{2} \Omega_c|^2 + (\gamma_{21} - i \Delta_p)[\gamma - i(\Delta_p + \Delta_c)]} \quad , \quad (4.14)$$

where \mathcal{N} is the number density of atoms, $\Omega_c = \mathbf{d}_{32} \cdot \mathbf{E}_c / \hbar$ is the Rabi frequency associated with the coupling beam, \mathbf{d}_{32} is the atomic dipole moment for the coupling transition, and \mathbf{d}_{31} for the probe transition. Also, in order to account for broadening of the EIT features, for instance due to variations of the magnetic field and the finite transit-time of atoms

passing through the beams, the ground state dephasing rate γ_{21} has been included.

With the quantisation axis taken along the B -field and propagation direction, the linearly polarised probe and coupling beams comprise a total of four circularly polarised components. If we also include the $F' = 1$ excited states, which are well within the Doppler-broadened profile, then we have a total of 18 interconnected Λ systems encompassing 16 Zeeman states. The systems are defined by the transitions $|F_p, m_p\rangle \xleftrightarrow{p} |F', m_p + q_p\rangle \xleftrightarrow{c} |F_c, m_p + q_p - q_c\rangle$, where the $q = \pm 1$ correspond to spherical tensor components of the probe and coupling fields (q_p and q_c can either be ± 1). We choose not to solve the full 18-level master equation but rather simply treat each Λ system individually according to equation 4.14, with d_{31} and Ω_c depending on the relevant oscillator strengths and coupling beam polarisation component, and with modified detunings:

$$\Delta_p \rightarrow \Delta_p + \mu_B B [g_{F_p} m_p - g_{F_c} (m_p + q_p - q_c)] \quad (4.15)$$

$$(\Delta_p + \Delta_c) \rightarrow (\Delta_p + \Delta_c) + \Delta_{F'} + \mu_B B [g_{F_p} m_p - g_{F'} (m_p + q_p)] \quad (4.16)$$

The additional excited state detuning $\Delta_{F'}$ is equal to $2\pi \times 55.55$ MHz for $F' = 1$, and 0 MHz for $F' = 2$ [93], and the distribution of atomic velocities are accounted for by averaging over Doppler shifted values of Δ_c weighted by a Maxwell-Boltzmann distribution. Summing over m_p and F' for fixed q_p and q_c gives a single component $\chi_{q_p}^{q_c}$, and then the total χ_{q_p} is given by a symmetric (anti-symmetric) superposition of $\chi_{q_p}^{+1}$ and $\chi_{q_p}^{-1}$ for lin||lin (lin \perp lin) polarisations. We thus finally obtain the susceptibility difference,

$$\begin{aligned} \Delta_\chi &= \chi_{-1} - \chi_{+1} \\ &= \begin{cases} (\chi_{-1}^{+1} + \chi_{-1}^{-1}) - (\chi_{+1}^{-1} + \chi_{+1}^{+1}), & \text{lin} \parallel \text{lin} \\ (\chi_{-1}^{+1} - \chi_{-1}^{-1}) - (\chi_{+1}^{-1} - \chi_{+1}^{+1}), & \text{lin} \perp \text{lin}. \end{cases} \end{aligned} \quad (4.17)$$

We show the theory spectra calculated in Figure 4.11. We can see that the main features of the data in Figure 4.10 are reproduced, in particular the greater optical anisotropy for lin||lin polarisations. Furthermore, the spectral asymmetry of Δ_ϕ due to the additional detuning $\Delta_{F'}$ of the $F' = 1$ states is also apparent for the 83 μT case. What is missing

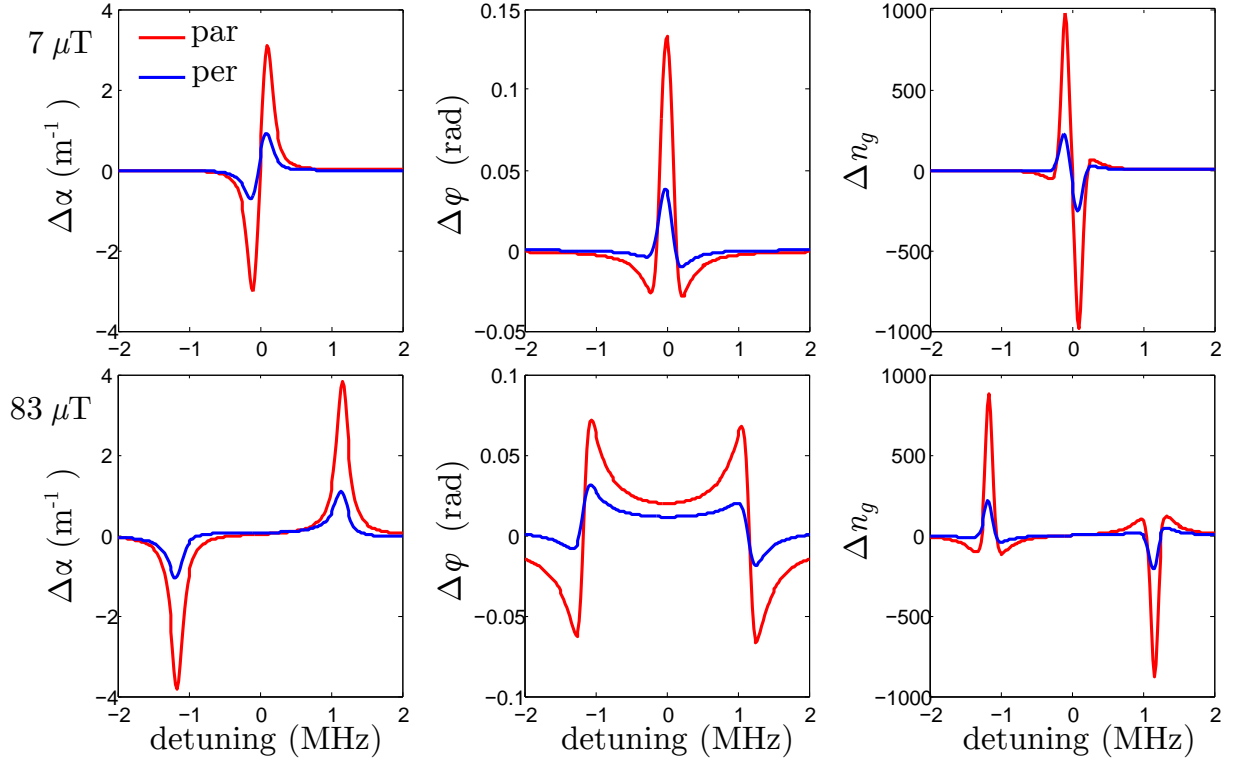


Figure 4.11: Theoretical spectra as calculated by using equation 4.14, and 4.17. Parameters are $\Delta_c = 0$, $\Omega_c = 2\pi \times 10$ MHz, $\gamma_{21} = 2\pi \times 0.18$ MHz, and $\mathcal{N} = 1.5 \times 10^{11}$ cm $^{-3}$ (for our temperature we expect $\mathcal{N} = 1.65 \times 10^{11}$ cm $^{-3}$ – see Appendix B.2).

from the simulations is the small remnant of the central EIT peak visible at higher field. This feature only vanishes under perfect balancing of the ideally equal LHC and RHC contributions. Any polarisation imperfections (for example due to the induced birefringence in the heated cell windows) or magnetic field uniformity (due to the relatively small solenoid and imperfect shielding), perturb this balance. Quantitative differences in the magnitudes and widths of the features also exist. Otherwise, the agreement between this highly simplified model and our observations is good. This suggests that other effects that have not been taken into account in our calculation are negligible for our parameters. For example, the variation of E_p and E_c throughout the cell volume has not been included, a uniform distribution of ground state populations has been implicitly assumed, and nonlinearities and higher-order coherences related to the multiply-connected network of Λ systems have been neglected. Still, the spectral shape, magnitude, and polarisation dependence of the magneto-optical anisotropy are all well captured by equations 4.14-4.17.

We should stress the fact that all the terms χ_{qp}^{qc} in equation 4.17 are the same for the two polarisation configurations; it is only the signs of their contributions which differ. The origins of these signs in the superpositions of RHC and LHC polarisations in the probe and coupling beams reveal the coherent nature of the magneto-optical anisotropy.

4.5 Discussion and conclusion

Electromagnetically induced transparency has been studied in a heated potassium vapour cell. EIT resonances with deeply sub-natural widths were obtained with only a free-running laser and an AOM. The laser did not require to be locked and the width of the EIT features was only limited by stray magnetic fields and transit-time broadening. The group index was optimised with cell temperature and group indices of several thousand were generated. Furthermore, the absorption from Doppler-shifted atoms not participating in EIT was observed. Additionally, the response of the EIT medium to a longitudinal magnetic field was studied and it was shown that it exhibits magneto-optical anisotropy for either $\text{lin}||\text{lin}$ and $\text{lin}\perp\text{lin}$ probe-coupling polarisations. A novel heterodyne measurement of the circular dichroism was demonstrated, and its results showed that the magnitude of the induced anisotropy depends on the relative polarisations. This effect highlights the role of interfering coherences among the many Λ systems that contribute to the EIT signal, as captured in a simple multilevel model.

Chapter 5

Magneto-optically trapping ^{39}K

In this chapter, the basic mechanism behind a magneto-optical trap (MOT) will be discussed. Additionally, the time-of-flight technique used in order to measure the temperature of our 3D-MOT will be explained, and results demonstrating that the typical temperature of our cold atomic cloud is on the order of ~ 1 mK will be shown. Working towards the goals of the experiment, i.e. achieving collective strong coupling and EIT in the cold in-cavity atomic cloud, it was decided to proceed with optimisations of the cloud temperature, atom number and optical depth for reasons that will be discussed later in the chapter. Results showing how the 3D-MOT temperature varies with respect to various laser beams' powers and frequencies will be presented, and lastly, the effects of the temperature of the 2D-MOT chamber and dispenser current on the 3D-MOT atom number and optical depth will be demonstrated.

5.1 Magneto-optical trap

This section starts with some historical notes about laser cooling and magneto-optical trapping. Then, the two basic mechanisms upon which a MOT relies are introduced, i.e. Doppler effect and Zeeman shift. We close the section by discussing details of our potassium MOT.

5.1.1 Historical notes

It was soon after the invention of the laser that proposals on how to cool atoms by employing the Doppler effect started emerging [116, 117]. In 1985, Doppler cooling was practically realised, resulting in atom trapping in 1D, 2D and 3D configurations [118–120]. These advancements resulted in having the atoms slowed, but never actually trapped since the force acting on them depended on their velocity, not their position. This scheme is called “optical molasses”. As described in [120], using this method it was possible to 3D cool millions of sodium atoms, and have them confined for about 0.1 s.

In order to address the issue of spatial confinement, a quadrupole magnetic field needs to be added. This was done for the first time in 1987 and resulted in the trapping of about 10^7 neutral sodium atoms, for up to 120 s [121]. This technique is called magneto-optical-trapping and nowadays is the basis of essentially all cold atom physics experiments.

5.1.2 Doppler cooling–optical molasses

We shall consider a simple two-level atom, in its ground state $|g\rangle$, and stationary with respect to the lab frame. The atom is illuminated by monochromatic light with frequency $\omega_0 = \omega_e - \omega_g$, where ω_e is the angular frequency related to the excited state of the atom $|e\rangle$. We also consider that the light travels towards the right ($+\hat{i}$) direction, to help us visualise the situation better. The atom, at some time, absorbs one photon and gets excited to $|e\rangle$. At the same time, it also gains some momentum $\mathbf{p} = \hbar k \hat{i}$, related to the photon momentum before it was absorbed.

If we consider light with low intensity (so that spontaneous emission is far more probable than stimulated emission), then at time τ after (where $\Gamma = 1/\tau$ (FWHM) is the decay rate of the atom from the excited state), the atom relaxes to its ground state and the photon is emitted. Since spontaneous emission is an event in which the photon emission has no preferential direction, after many scattering events, the net force resulting from

this mechanism averages to zero. Hence, the atom is left with some net momentum with direction towards $+\hat{\ell}$, related to the so called “scattering force” (i.e. a force related to the photon scattered by the atom).

We now add to this picture another light beam, of the same frequency and intensity as the one considered before, but travelling towards the left ($-\hat{\ell}$). Then, for a stationary atom, you would expect the forces in each direction to cancel. But what happens if the atom has some initial velocity (with direction $\pm\hat{\ell}$)? Then, immediately you expect the light beams to have less of an impact on the atom, as now neither of them is resonant with it, due to the Doppler effect. What is required now in order to slow the atom is to shift the lasers’ frequency a few linewidths Γ down to the red (i.e. lower frequency). This way, the atom preferentially absorbs photons from the beam counterpropagating to the atomic motion, as it sees this frequency shifted to the blue (i.e. higher frequency), thus becoming resonant with it.

As we can see, the force acting on the atoms depends on their velocity and does not act in a way to trap atoms to a certain position. The scattering force (from each beam) is just the scattering rate Γ_{sc} times the momentum transfer after each scattering event,

$$\mathbf{F} = \hbar\mathbf{k}\Gamma_{sc} = \hbar\mathbf{k} \times \frac{\epsilon\Gamma/2}{1 + \epsilon + [2(\delta + \omega_D)/\Gamma]^2} \quad , \quad (5.1)$$

where $\delta = \omega_L - \omega_0$ is the laser’s detuning from the atomic resonance and $\omega_D = -\mathbf{k} \cdot \mathbf{v}$ is the Doppler shift (as seen by the atoms). The ϵ term is just a ratio between the relative intensity of the laser light to the atomic saturation intensity, given by $\epsilon = I/I_s$, where $I_s = \pi\hbar c/(3\lambda^3\tau)$.

Using equation 5.1, the total force acting on atoms moving along the two counterpropagating laser beams of the same frequency can be calculated [122],

$$\mathbf{F}_{\text{OM}} \cong \frac{8\hbar k^2 \delta \epsilon \mathbf{v}}{\Gamma[1 + \epsilon + (2\delta/\Gamma)^2]^2} \equiv -\beta\mathbf{v} \quad . \quad (5.2)$$

Here, $(kv/\Gamma)^4$ and higher terms have been omitted. For small velocities, it follows that \mathbf{F}_{OM} is proportional to the atomic velocity with the damping constant β . For $\delta < 0$, the

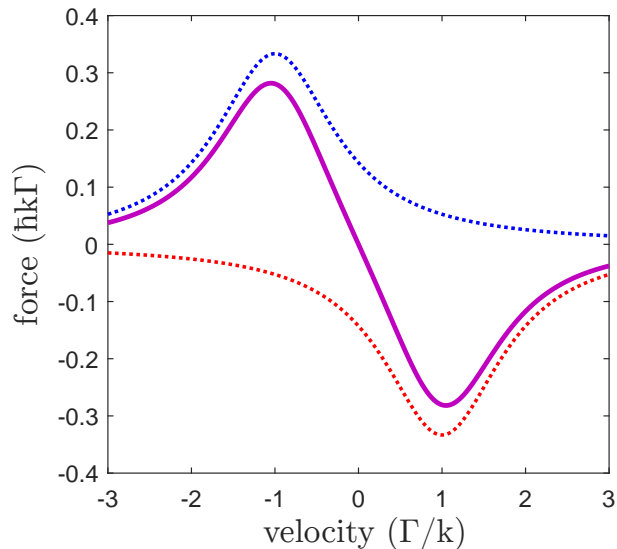


Figure 5.1: Doppler cooling force acting on atoms of different velocity classes. Dotted lines (blue and red) represent the force by each one of the counterpropagating beams involved in the interaction. Purple solid line is the total force, given by equation 5.2, for $\epsilon = 2$, $\delta = -\Gamma$.

sign of \mathbf{F}_{OM} is opposite to that of \mathbf{v} , therefore the atoms are slowed down. Figure 5.1 uses equation 5.2 to demonstrate this effect. The atomic movement is reminiscent of that in a viscous product called molasses, which is the reason this technique is commonly known as optical molasses (OM).

The equations and discussion up to here only considered laser cooling in 1D, for the sake of simplicity and easier visualisation. These considerations can easily be extended to consider atom cooling in more dimensions. For example, the inclusion of two more pairs of counterpropagating beams, orthogonal to the first pair and to each other, can result in a 3D cold atomic cloud.

The average kinetic energy of an atomic sample is what is usually used to describe its “temperature”. While the laser light damps the motion of the atoms (i.e. provides cooling), at the same time it also causes some heating. Balancing the cooling to heating rate sets the minimum achievable temperature in an OM, called the Doppler temperature T_D . More specifically, the damping force provided by \mathbf{F}_{OM} reduces the average atomic velocity to zero. But, as the mean velocity is reduced to zero, we should note that this is

not the case for the mean squared velocity, which remains finite (i.e. the variance of the atomic velocity is not zero). As \mathbf{F}_{OM} removes kinetic energy from the atom, the random nature of photon emission and absorption provides heating. Thus, we should understand that equation 5.2 only represents the average damping force acting on the atoms where the force's fluctuations produce heating [123]. The Doppler temperature has been derived in the past [122] and is equal to:

$$T_D = \frac{\hbar\Gamma}{2k_B} \quad . \quad (5.3)$$

For the D_2 line of ^{39}K , $\Gamma = 2\pi \times 6.02$ MHz [86], resulting to $T_D = 145$ μK .

The first experimental realisations of 3D-OM [120, 124] revealed that temperatures significantly lower than T_D were possible¹. This result highlighted the fact that the atomic structure is far too complex to be captured by a simple two-level model. Soon after, theoretical models accounting for the mechanisms responsible for the observed sub-Doppler temperatures were developed [123, 125]. The new models took into consideration the multi-level nature of atoms, the role of optical pumping, and how polarisation gradients created by counterpropagating laser beams can affect atomic motion. The models also re-calculate the damping constant β and show that its magnitude can be much higher than what was first calculated for the simple two-level atom case (see equation 5.2).

5.1.3 Confining the atoms

By adding a spherical quadrupole magnetic field to the three orthogonal pairs of beams considered previously, a 3D-MOT can be created. The field can be realised by making use of an anti-Helmholtz pair of coils. In order to conceive how a MOT works, we employ again a simple 1D system, which is shown in Figure 5.2. The system consists of a fictitious atom with ground state $|F = 0, m_F = 0\rangle$ and excited state $|F' = 1, m_F = -1, 0, 1\rangle$. Here, F is the sum of the electronic and nuclear angular momentum, primes indicate excited states

¹Actually, in the first 3D-OM paper [120], it was reported that the temperature of their sodium cloud had a temperature exactly at the Doppler limit. But, when a different group [124] also managed to make a 3D-OM (also sodium) and measured their cloud temperature using different techniques, they found that temperatures much lower than T_D were possible.

and m_F denotes the projection of F and F' along the axis the magnetic field is applied. Defining the x -direction to be along this axis, the centre of the trap is at $x = 0$, and the field at this position is zero. For $x \leq 0$, the field varies linearly. When the magnetic field is non-zero, the magnetic sublevels for each state are no longer degenerate due to the Zeeman effect. Thus, the different sublevels become susceptible to different light polarisation [98]. As the selection rules command, σ^+ light drives the $|F = 0, m_F = 0\rangle \rightarrow |F' = 1, m_F = 1\rangle$ transition and σ^- light drives the $|F = 0, m_F = 0\rangle \rightarrow |F' = 1, m_F = -1\rangle$ transition.

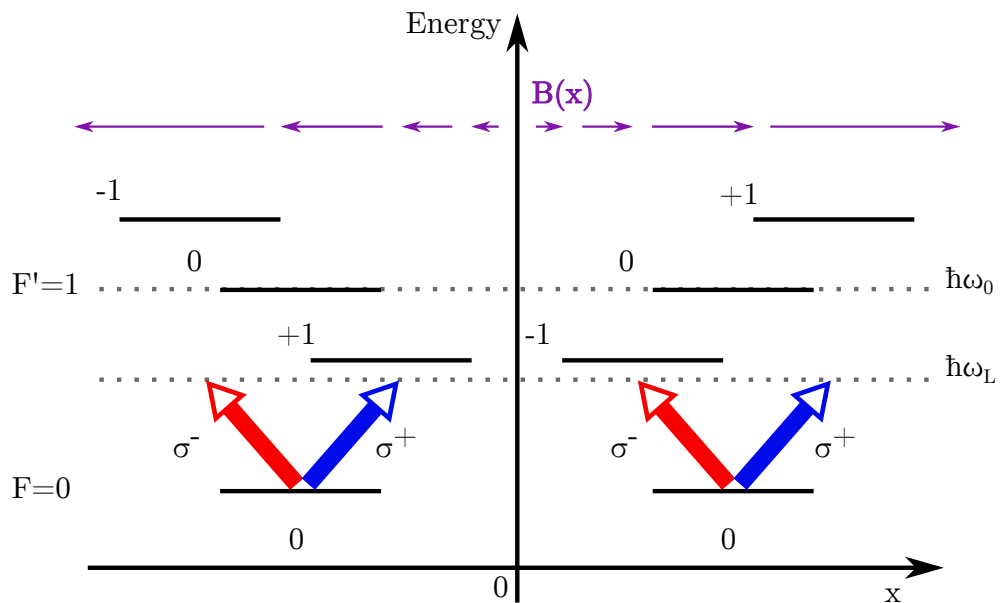


Figure 5.2: Simple illustration of the operating mechanism of a MOT with an atom with $F = 0$ and $F' = 1$ states. Here, ω_0 represents the unshifted resonant frequency of the atomic transition and ω_L stands for the frequency of the laser. The magnetic field is position dependent and varies linearly with the distance from the centre of the trap. The σ^\pm beams are absorbed and scattered by atoms at a rate which depends on their detuning $(\omega_0 - \omega_L)$, which side of x they are, and their distance from the centre of the trap (and their intensity). The Zeeman shifts shown here at either side of x are for the same absolute distance from the centre of the trap ($x = 0$).

The magnetic levels in a 1D quadrupole magnetic field tune in such a way that the transition frequencies vary along the field, depending on the distance from the centre of the trap. For $x > 0$, the Zeeman shift brings the $|F = 0, m_F = 0\rangle \leftrightarrow |F' = 1, m_F = -1(+1)\rangle$ closer (farther) to (from) resonance. Thus, if we choose the polarisation of the laser light incoming from the right to the left ($+x \rightarrow -x$) to be σ^- , then the atom is subjected to

resonant light and will frequently absorb and scatter radiation². This situation drives the atoms towards the centre of the trap, where $B = 0$. For $x < 0$, the Zeeman shift brings $|F = 0, m_F = 0\rangle \leftrightarrow |F' = 1, m'_F = +1\rangle$ closer to resonance, hence atoms preferentially scatter light with σ^+ polarisation (thus, it is sensible to use σ^+ light with direction from left to the right, i.e. $-x \rightarrow +x$). Therefore, as can be understood, the MOT mechanism differs from that of the optical molasses in the sense that it does not only have an effect in velocity space but also in the position space. Hence, in a MOT, atoms are not only slowed (cooled) but also confined.

5.1.4 Cold cloud of potassium atoms

By employing the laser system described in Chapter 3, the light addressing the required laser cooling transitions is derived. In a simple two level system, as discussed above, only one frequency of light is required in order to make a MOT. In reality though, most atoms have a far more complex structure and illuminating them with light addressing only one transition is usually not enough to realise the MOT. The energy level diagram for the D_2 line of ^{39}K is shown in Figure 5.3. The cooling transition for ^{39}K is deliberately chosen to be addressing the $F = 2 \rightarrow F' = 3$ transition, as its transition strength is large and you expect the atoms to always decay back to the $F = 2$ ground state (“closed transition”), since according to the selection rules $\Delta F = 0, \pm 1$. However, the hyperfine splitting between $F' = 3$ and $F' = 2, 1$ is on the order of the atomic linewidth (and much smaller than the initial Doppler linewidth) and as such there is a non-negligible probability for the atom to be excited to either the $F' = 2$ or even the $F' = 1$ state and consequently decay to the $F = 1$ ground state. Therefore, a second beam addressing the $F = 1 \rightarrow F' = 2$ transition is necessary in order to pump atoms back out of the $F = 1$ state and ensure that the MOT atom number does not, after a few cycles, decay to zero. The two laser beams are called “cooling” ($F = 2 \rightarrow F' = 3$) and “repump” ($F = 1 \rightarrow F' = 2$), based on their operation.

²Not only the atoms scatter σ^- light frequently but they also scatter σ^- more frequently than σ^+ .

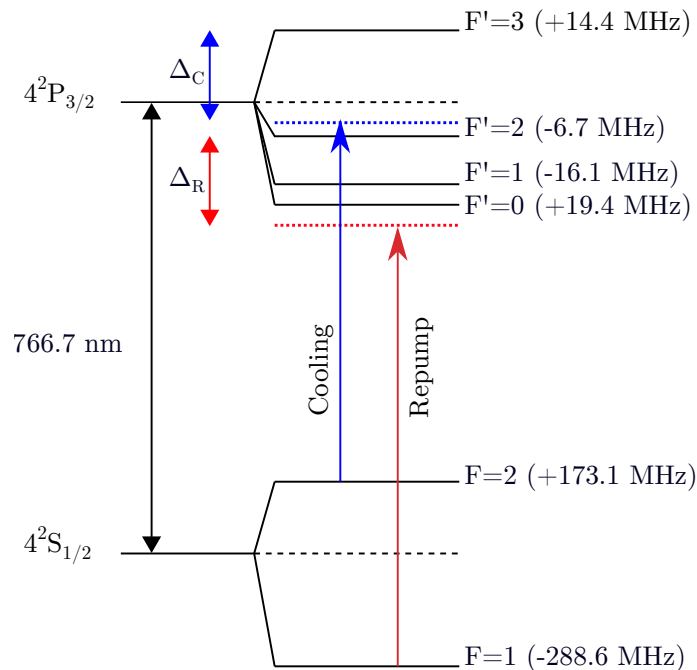


Figure 5.3: Energy level diagram showing the D_2 line of ^{39}K [93]. The two laser beams, cooling and repump, required for efficient optical cooling of potassium are shown in blue and red colour, respectively. The cooling beam was detuned from resonance by $\Delta_C = -27$ MHz and the repump beam by $\Delta_R = -18$ MHz. The detunings were specifically chosen in order to optimise the atom number in the trap.

Since the hyperfine splitting of the excited states is comparable to that of the natural linewidth, the cooling to repump ratio necessarily has to be relatively small, compared to what is usually the case for other alkali metal species, such as rubidium 87. Simulations showing this effect can be found in [80, 126]. The energy level structure of ^{39}K also makes the addressing of particular transitions more difficult, if at all possible. This complicates the application, and could lower the efficiency of some techniques, such as EIT. But, at the same time, the small splitting can also be beneficial. For instance, it can help to reduce the number of lasers in the experiment, since beams with similar frequencies can be generated by simply using AOMs.

5.2 Determining the atomic cloud parameters

Determining important parameters such as the temperature (T) of the atomic cloud, its atom number (N), RMS size (σ) and optical depth (OD) is central to this experiment. In order to do that, a camera³ imaging the MOT fluorescence is required, along with some coding lines required to analyse the images properly and extract all the useful information. The majority of the imaging part in the experiment was done by former PhD students [80, 82]. Here we are mostly going to emphasise measurements that were completed using this code, during this PhD. In the following subsections we will discuss results on the all-important parameters, T , N , σ and OD .

5.2.1 Temperature

When making measurements, it is important to have no light other than that probing the transition of interest shining on the atoms. Hence, the MOT light beams have to be switched off during measurements, such as the normal-mode splitting. Then of course, since no force acts on the atoms, the cloud starts to expand at a rate that depends on the cloud temperature. It is important to ensure that this expansion is negligible during the period of the measurement, so that a constant cloud optical depth can be assumed. In order to determine whether this is the case or not, it is essential to make a temperature measurement of the MOT.

The temperature of our atomic cloud was measured by following the release-recapture (RR) and the time-of-flight (TF) techniques. The first (RR), involves pulsing the 3D-MOT beams off for some time t before turning them back on to determine the fraction of atoms that remain captured [127]. This technique requires the capture region of the trap to be known precisely. On the other hand, TF requires both the 3D-MOT light and magnetic field to be off during the measurement. A fluorescence image of the expanding

³Allied Vision Technologies, Pike F-145B.

cloud is taken and then is used to determine the size of the MOT for different release times t . Here, we will only discuss TF measurements as RR in the experiment was solely implemented by a former PhD student [80]. The TF measurement is considered to be more reliable than RR as it does not rely on assumptions such as the spatial atomic distribution before the release [128].

As already briefly discussed, the TF method uses fluorescence images of the MOT, taken after various periods of time (t) during which the 3D-MOT light and magnetic field are off and thus the cloud is let to expand. By fitting the MOT images, the RMS size of the MOT ($\sigma_{r=x,y,z}$) can be determined and the temperature of the cloud can thus be interpreted as [129],

$$\sigma_r(t) = \sqrt{\sigma_{0r}^2 + \frac{k_B T_r}{m} t^2} . \quad (5.4)$$

Here, σ_{0r} is the initial RMS size of the cloud, T_r is the cloud temperature, and m is the atomic mass. Thus, if $\sigma_r(t)$ at different t is known, T_r can easily be determined. In principle, the cloud could have a different kinetic temperature in each axis, as the MOT is not in true thermal equilibrium.

A typical experimental sequence started with a MOT loading period of a few seconds (during which all the light beams and the magnetic field were on). Then, the 3D-MOT and pushing beams were turned off, using an RF switch controlling the 3D-MOT AOMs and a shutter respectively, and the 3D-MOT magnetic field was shut off using the relay switch (see Chapter 3). Following this, at a time t , the 3D-MOT beams were instantaneously turned on and simultaneously the camera was triggered to take a picture (exposure time ~ 1 ms). By fitting the MOT images to extract the size of the cloud, plotting σ_r as a function of t and fitting the data using equation 5.4, we were able to determine the temperature of our MOT, along the different accessible axes. By randomising the order of taking the MOT images for different expansion times, possible long-term effects from drifts that could affect the measurement were prevented. Figure 5.4 shows MOT images taken at various t . It is apparent from the images that at successive t , the cloud expands.

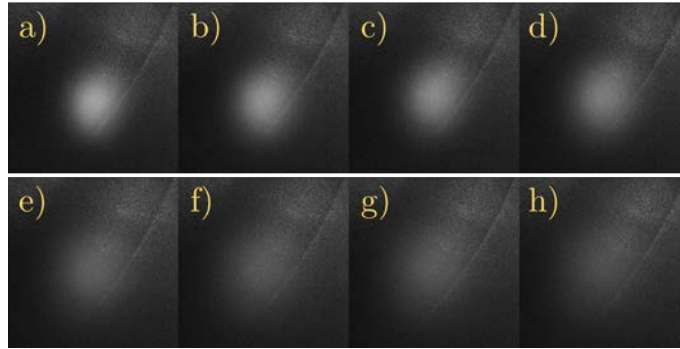


Figure 5.4: MOT images taken at multiple times, t . Here, t is successively increased from a) \rightarrow h). For a) $t = 0.2$ ms and for h) $t = 1.5$ ms.

Figure 5.5 shows TF results generated by fitting the images shown in Figure 5.4, using a 2D Gaussian fit in MATLAB. The results show that the MOT temperature for either axis (note that we can only determine the temperature of the MOT along two axes, x and y), was >1 mK. The MOT temperature is much higher than the Doppler temperature, but this is not surprising for experiments with potassium atoms [130].

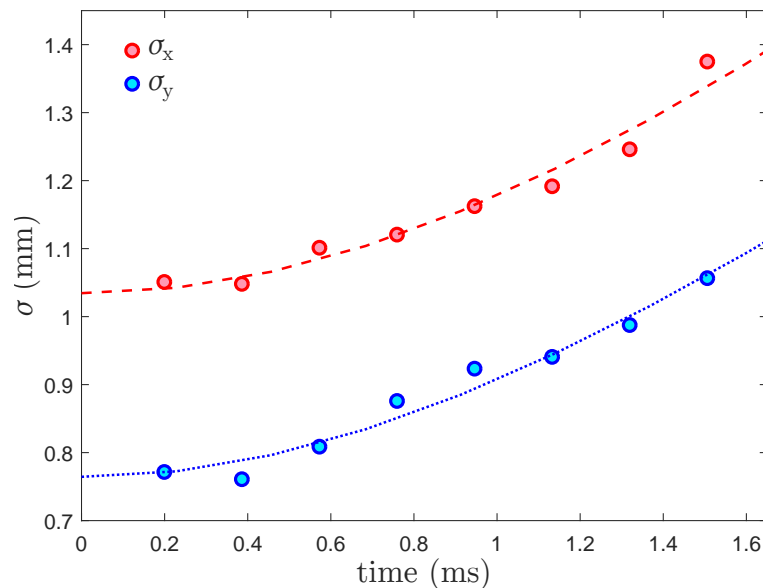


Figure 5.5: Typical time-of-flight measurement (without temperature optimisation). By fitting the data using equation 5.4, the temperature along the x and y axes were determined, giving $T_x = 1.49(12)$ mK and $T_y = 1.30(8)$ mK, respectively. Points here represent single shots and errors are just standard errors from the fits.

5.2.2 Atom number and optical depth

The 3D-MOT atom number (N) and optical depth (OD) are critical for this experiment. High N is required to study cQED and high OD is necessary for EIT investigations. While it was not very difficult to enter the collective strong coupling regime, as will be shown in Chapter 6, we later found that it was not possible to observe absorption when probing the same atomic cloud directly (not using the cavity light). The latter was necessary to study EIT with the cold atoms, as will be discussed further in Chapter 7. N and OD are intrinsically connected in our experiment. No MOT-compression techniques [131, 132] are being employed and since MOT trapping region is fixed, increasing N also leads to an increase in OD . In order to improve N and OD , we examined the MOT behaviour for different dispensers' current and temperatures of the 2D-MOT chamber.

The MOT atom number was determined by making use of a fluorescence image of the MOT (as with the RMS size of the cloud necessary for the TF measurement). This technique is fairly simple as it only requires the following: detecting the light emitted by the atoms in the MOT using a camera, taking several MOT pictures with the MOT light beams on and then off (or with the magnetic field off – this is required for background image subtraction), and associating the image pixels with photons and thus atom number. The latter can be done by figuring out the (camera)pixel-photon calibration constant, the photon detection solid angle of the camera, and the per atom fluorescence rate (R). In order to calculate R , the method described in [126] was followed, in which we have taken under consideration all six hyper-fine-structured levels of potassium. The fluorescence imaging technique was implemented in our experiment by former PhD students and is described in more detail in [80, 82].

The optical depth of an atomic cloud can be measured by probing the cloud with a light beam of frequency (ω_L) and intensity (I_0), and collecting the transmitted light of intensity I ,

$$OD = \ln\left(\frac{I_0}{I}\right) . \quad (5.5)$$

This assumes that $I_0 \ll I_s$, where $I_s = \pi \hbar c / (3\lambda^3 \tau)$ is the saturation intensity of the atom, as it has been defined earlier in the chapter. By measuring OD , we can gain insight on what the volume density $\rho(x, y, z)$ of the cloud is (and reversibly, if ρ is known we can calculate the expected value of OD from an absorption measurement).

As stated by Beer's law,

$$\frac{dI}{dz} = -\rho\sigma I = -\frac{\rho\sigma_0 I}{\left(\frac{2\Delta}{\Gamma}\right)^2 + 1} \quad , \quad (5.6)$$

where $\sigma_{(0)}$ is the (resonant) scattering cross-sectional area of the atoms which is a function of the detuning $\Delta = \omega_L - \omega_0$ from the atomic resonance (ω_0), and $\sigma_0 = \frac{3\lambda_0^2}{2\pi}$.

As follows from 5.6,

$$\int_{I_0}^I \frac{1}{I} dI = \int_{-\infty}^{\infty} -\rho\sigma dz \quad (5.7)$$

$$I = I_0 e^{-n\sigma} \quad ,$$

where $n(x, y) = \int_{-\infty}^{\infty} \rho dz$ is the integrated atomic column density per unit area [133]. By comparing equations 5.5 and 5.7, we arrive at the simple relation stating that $OD = n\sigma$.

5.3 Cloud optimisations

High atom number and optical depth, and low temperature of the atomic cloud are all beneficial for various measurements we are interested to make in the experiment. The former two enhance the strength of collective light-matter interactions and have enabled EIT investigations with cold atoms, as will be discussed in Chapter 7. On the other hand, lower temperature means that the optical depth of the cloud is preserved for longer times after the MOT light and/or magnetic field shut off, the two-photon Doppler broadening is reduced, and therefore the relative angle between the probe and coupling beams is not very important.

5.3.1 Temperature

As was shown in Section 5.2.1, the typical temperature of our MOT was around 1 mK, almost one order of magnitude higher than the Doppler-limited temperature. While this is typical in potassium, an atomic cloud of lower temperature could fundamentally improve the conditions under which measurements like EIT are made (longer probing periods and small two-photon Doppler broadening).

Background

Bosonic isotopes of potassium, such as ^{39}K have been found to be very difficult to cool down to sub-Doppler temperatures, compared to other alkali species, such as sodium, rubidium and caesium. The most profound reason for this is the fact that their natural linewidth Γ is of similar magnitude as the hyperfine splitting of their excited states [134], that can lead to heating effects such as photon reabsorption.

Sub-Doppler temperatures can be achieved if one takes advantage of the even richer atomic structure when a magnetic field is applied and Zeeman sub-levels are no longer degenerate [125]. Usually, detuning (Δ_C , see Figure 5.3) is chosen to be large compared to Γ to ensure that the photon scattering rate is kept low and thus photons which are spontaneously emitted have low probability of being reabsorbed by the atomic cloud. At the same time, Δ_C has to be small compared to the frequency splitting of the targeted state and the neighbour states (Δ). Otherwise, this could lead to addressing more than just the intended state, and optical pumping to occur, which can deeply affect the effective cooling of the atoms [135]. Since for ^{39}K , the frequency splitting between $F' = 2$ and $F' = 3$ states is approximately 3.5Γ , the previous two conditions ($\Delta > \Delta_C \gg \Gamma$) for sufficient sub-Doppler cooling are intrinsically difficult to satisfy.

On the other hand, having states very close to each other could be beneficial as atomic population depumping into dark states can naturally happen [136]. In our case, the cooling beam would pump atoms from the $F = 2$ to the $F = 1$ ground state, and the

repump ($F = 1 \rightarrow F' = 2$) would pump atoms the other way, from the $F = 1$ to the $F = 2$ state. By adjusting the intensity of either light, we are in control of the fraction of atoms in each state and the number of spontaneously emitted photons that could be reabsorbed (and cause heating) can be kept low.

Cooling procedure

A few groups in recent years have managed to sub-Doppler cool potassium [136–138], all following a similar approach. We have adopted our strategy according to their observations and results. The only major difference was that we kept the 3D-MOT magnetic field constantly on (i.e. no molasses stage). Since close to the centre of the MOT the field approaches zero, it can be assumed (up to a degree) that the atoms experience approximately the same polarisation gradient as in an OM. We chose to leave the field continuously on during this investigation since, as we have observed in Chapter 3, when switching off the field, the cavity is disturbed. Thus, there was no point in investigating if a colder cloud with the magnetic field off could be achieved while this could not be applied in the actual experiment.

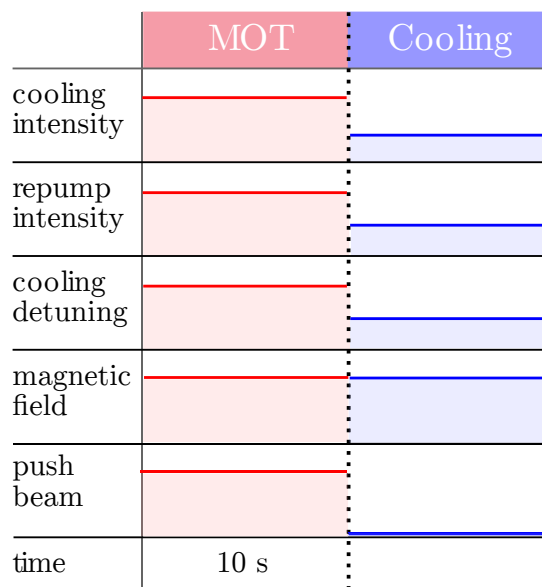


Figure 5.6: Simple schematic of the cooling procedure and the different parameters that can be varied in order to achieve a colder atomic cloud.

Figure 5.6, provides an illustration of the procedure followed in order to carry out this investigation. At the MOT stage, which lasted for as long as 10 s, the values of the different parameters were specifically chosen to optimise the MOT atom number. This investigation was done by former PhD students [80, 82]. It is generally true that in order to achieve a cloud with many atoms, the intensity of the laser beams has to be high and the detuning large, in order to have a large velocity capture range [139]. We start with 3D-MOT beams with 10 mW/cm^2 total peak intensity, each. Furthermore, the intensity ratio between the cooling and the repump beams was set to be about 3:2. The detuning of the beams was -27 MHz (i.e. $\Delta_C/\Gamma = -4.5$) for the cooling, and -18 MHz ($\Delta_R/\Gamma = -3$) for the repump. During the cooling stage, we abruptly change the values of the different parameters (as there was no availability at the time for ramping them), and except from the MOT magnetic field, which is kept constant, all of the parameters described above are varied.

Results

In this section we present measurements conducted in order to investigate how the temperature of the MOT varied for different parameters such as the detuning of the beams, their intensity, and the time for which the cooling procedure lasts. It is not a primary goal of this thesis to provide a model to account for how the cloud temperature should vary for the different parameters. Nonetheless, simple explanations will be given in order to address some of the main mechanisms at play. The temperatures shown in the following results is the geometrical mean of the temperatures along each axis, rather than the value for one specific axis.

The first parameter that was examined was the detuning of the cooling beam from resonance, Δ_C . As shown in [136], the shape of the scattering force versus atom velocity curve depends on Δ_C . More specifically, in this study they calculate this curve, and correspondingly the type of cooling it provides, for three Δ_C ranges (they cover the entire frequency range from $F' = 3$ to $F' = 2$) as it is shown in Figure 5.7. The general rule

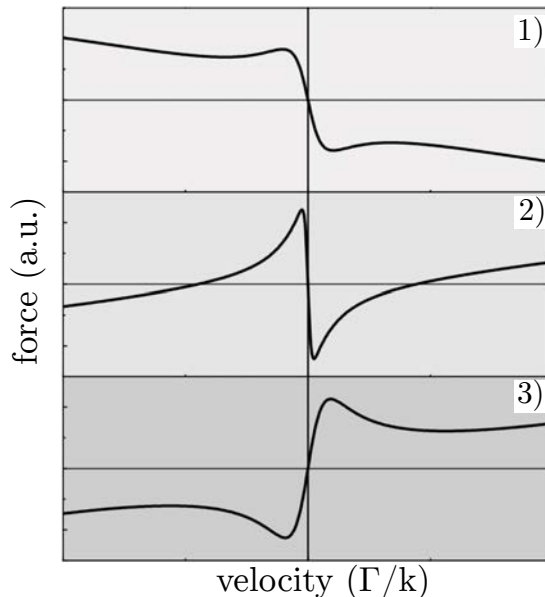


Figure 5.7: Scattering force versus atomic velocity curves as calculated by [136]. The three sub-figures (1-3) correspond to the calculated curve for different detuning ranges. Specifically, the force for a detuning within range 1 ($\Delta_C/\Gamma = 0 \rightarrow 2.2$) provides Doppler and sub-Doppler cooling. For range 2 ($\Delta_C/\Gamma = -2.2 \rightarrow -3.2$) it provides sub-Doppler cooling, and for range 3 ($\Delta_C/\Gamma = -3.2 \rightarrow -3.5$) it provides heating.

here is that when light is red-detuned from a transition, the scattering force acting on the atoms can cool them, whereas if it is blue-detuned, the scattering force heats the atoms. Further to these three ranges, they calculate that for $\Delta_C/\Gamma < -9.4$, i.e. when the cooling beam is red-detuned with respect to all the excited states, Doppler cooling is active and the capture velocity range is the largest.

In our experiment, every time Δ_C was being varied, Δ_R was simultaneously being varied as well, as no independent control of these parameters was available at the time of writing. We believe this did not play a significant role in this investigation as the cooling beam is the dominant beam controlling the effectiveness of the laser cooling, especially sub-Doppler cooling. This is mainly due to the relative transition strengths, and larger degeneracy of the involved Zeeman levels [135]. For this measurement, during the cooling stage which lasted 2 ms, the total intensity of MOT light was halved relative to the trapping stage (i.e. 5 mW/cm² for each beam) and we kept the cooling to repump ratio at 3:2.

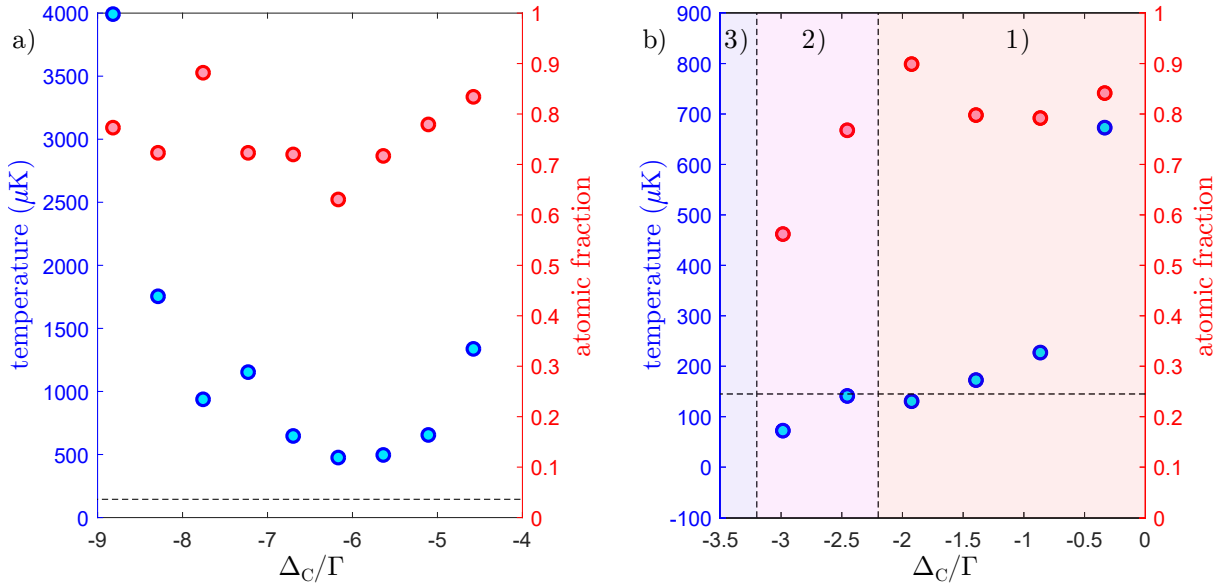


Figure 5.8: MOT temperature versus cooling detuning, Δ_C . Blue circles represent measurements of the cloud temperature using the TOF technique, whereas red circles represent the fraction of atoms left in the atomic cloud at the end of the cooling stage. Horizontal dashed black straight line indicates the Doppler limited temperature for ^{39}K . The figure has been split in a) and b) because of the big difference in the scale of the temperature axis between the two sub-figures, and also in order to give emphasis on the events happening in range 1-3. a) Shows how temperature and atomic fraction vary for Δ_C covering the frequency range between $F' = 2$ to $F' = 0$. b) Same measurement, for when Δ_C is somewhere between $F' = 3$ and $F' = 2$. The three ranges shown in Figure 5.7 are also indicated by dashed vertical lines and different colour coding. The temperature of the cloud is initially above the Doppler temperature in range 1 and becomes sub-Doppler as enters range 2. In range 3, the cloud completely disappears.

Figure 5.8 shows our results, which approximately agree with the calculation of [136]. We observe an atomic cloud with sub-Doppler temperature in range 2 and (mostly) above Doppler temperature for detunings in range 1 and $\Delta_C/\Gamma \lesssim -4.5$. We also note that the MOT disappears as we approach and enter range 3. In this range, the beam is (still) red-detuned with respect to the $F' = 3$ and blue-detuned with respect to the $F' = 2$ transition (as is also the case for range 1 and 2). Since though, the beam is closer to resonance with the $F' = 2$ transition (than $F' = 3$), the photon scattering rate is higher for transitions to $F' = 2$ rather than $F' = 3$ and the atoms experience a net heating force.

We also examined how the total intensity of the 3D-MOT beams affected the cloud temperature. The intensity ratio was kept at 3:2, $\Delta_C/\Gamma \sim -2$, and the cooling stage lasted

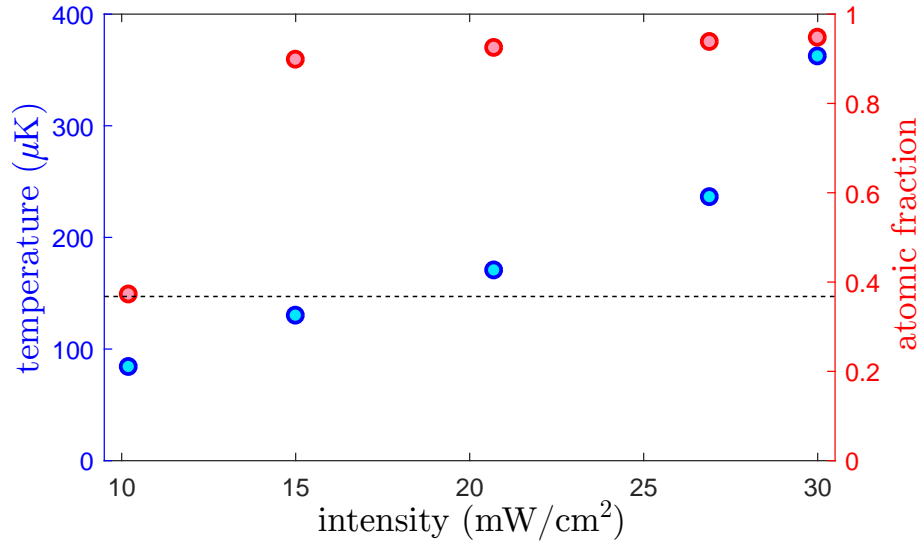


Figure 5.9: Total MOT beams' peak intensity effect on temperature and atomic fraction (deduced by single TOF measurements) of the cloud after the cooling stage. Dashed line indicates the Doppler temperature.

for 2 ms. As can be seen in Figure 5.9, the temperature did fall when the intensity was decreased, but at low enough intensities to reach sub-Doppler temperatures, the number of atoms in the cloud fell by more than 60 %. It is expected that as the intensity of the light beams is reduced, the temperature of the cloud decreases, as the slope of the cooling force also gets steeper with lower intensity. At the same time, the velocity capture range gets smaller and the number of atoms in the trap can get significantly decreased.

The last parameter we examined was the time for which the cooling stage lasted. For this measurement, $\Delta_C/\Gamma \sim -2.2$ and the total MOT peak intensity was halved (and again, the cooling to repump intensity ratio was kept the same). In [137], where they also jump the different parameters, it was found that the optimum time was $\sim 0.8 - 2$ ms. Similar behaviour was observed in our experiment as well, as shown in Figure 5.10.

We also intended to examine the effect of the cooling to repump intensity ratio on the temperature of the cloud. However, this investigation was not possible in our experiment for technical reasons⁴. According to the literature, when the intensity of the repump is

⁴The ratio can be controlled by changing the RF power driving the repump AOM (see Chapter 3), which is placed before the TA. Since in our experiment the same TA is seeded by both the cooling and the repump beam, mode competition between the two beams results in different amplification of them. Thus, measuring the power of each beam individually after the TA is not necessarily accurate. Sending the TA

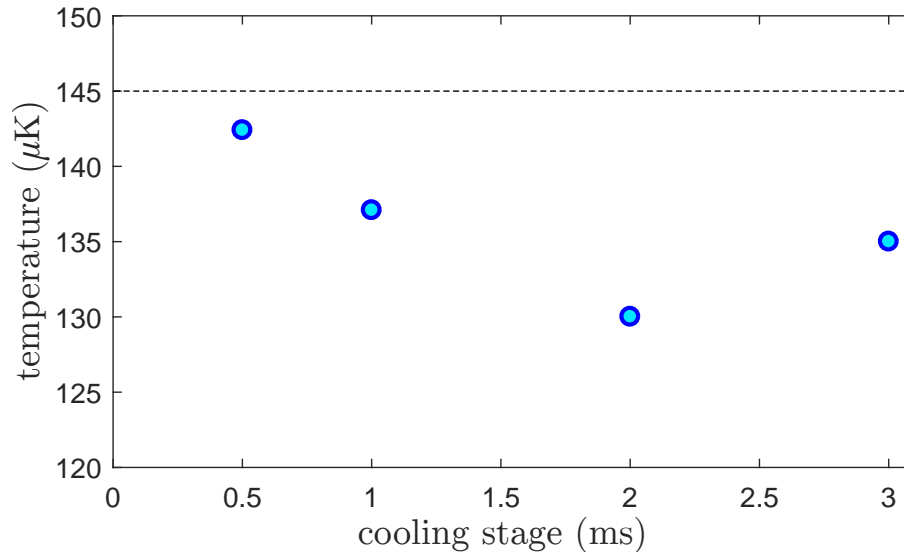


Figure 5.10: Temperature of the atomic cloud (deduced by single TOF measurements) as a function of the cooling stage time. Dashed line shows the Doppler temperature.

decreased compared to that of the cooling, the rate of scattering events that could lead to photon reabsorption (i.e. heating) should also decrease. This effect has been observed for atomic clouds with high densities [136, 137]. However, in clouds with small densities, like ours, this phenomenon is usually negligible and the temperature of the cloud should approximately remain constant. There is also a limit for how low the repump intensity can go, and if that gets exceeded, then no effective optical pumping happens and the cloud temperature increases [135].

Conclusion

Figure 5.11 shows a TOF measurement after the cooling stage. As can be seen, the rate at which the cloud expands is much slower than what it was in Figure 5.5 as a result of the lower temperature of the cloud. As discussed, this is beneficial for our experiment as measurements can be done while the MOT beams are off for longer time, without the OD of the cloud having changed by much. Additionally, it leads to reduced two-photon

output light through a cavity would have been a solution as we would just need to look at the cavity spectrum and figure out the power in each beam (it is just the power in each set of modes). However, no cavity was available at the time of the measurements. Thus, the only way to monitor this ratio would be to measure it before the beams were amplified and assume it remained the same after the TA, which would be inaccurate.

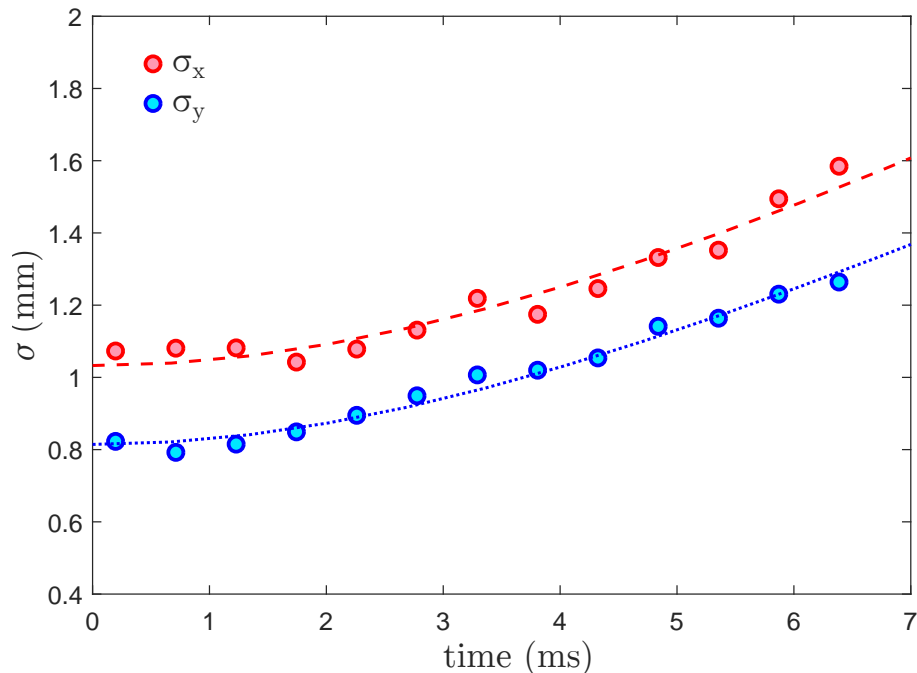


Figure 5.11: Typical time-of-flight measurement, after a cooling stage period of 2 ms. For this measurement, the total MOT peak intensity was halved to 15 mW/cm^2 , and $\Delta_C/\Gamma \sim -2$. The temperature along x was found to be $130(5) \mu\text{K}$ and $116(10) \mu\text{K}$ along the y -axis. Points here represent single shots and errors are just standard errors from the fits.

Doppler broadening which is useful for EIT.

From our investigation we observed that sub-Doppler cooling was possible even if the 3D-MOT field was kept continuously on. It is expected to be able to reach even lower temperatures once the field during the measurement is possible to be turned off without affecting the cavity. Furthermore, ramping the different parameters instead of just instantaneously jumping them should increase the fraction of atoms kept in the cloud after the cooling stage while keeping the atomic cloud very cold.

5.3.2 Atom number and optical depth

Two different approaches were followed in order to increase the MOT atom number and optical depth. Firstly, we investigated the effect of passing different currents through the dispenser as it is well known that the amount of alkali and other material which is released from a dispenser, strongly depends on the current that passes through it [140].

Secondly, we heated up the 2D-MOT chamber at various temperatures to see if that had any effect on the 3D-MOT, as potassium is known to adsorb onto surfaces when at room temperature [141]. The only part of the vacuum system being heated, up to the moment we decided to heat up the 2D-MOT chamber, was the dispensers cross. Even though the cross was directly connected to the 2D-MOT chamber, the chamber was found to be at almost room temperature. Heating the system helps to raise the vapour pressure of potassium, which is beneficial for increasing the partial pressure of potassium in the vacuum. [142].

Dispensers

The effect of firing the dispensers at various currents will be discussed here. The investigation involved monitoring the ion pump reading (indicating pressure in the chamber) for different current values and calculating the atom number 300 s after the current was turned back to 0 A.

Figure 5.12, shows the ion pump reading versus the time for which current was let to pass through the dispensers (120 s). It is evident from this measurement that the amount of material released from the dispenser does strongly depend on the current through the dispenser, as expected. It is also observed that the ion pump reading reaches a steady-state faster for higher currents. Note though that no conclusions about the real parameter of interest, which is the amount of potassium released at each current value and how this affects N and OD , can be drawn from this investigation. For this, we need to analyse the MOT images.

Before firing-up the dispensers on the day of the investigation, we found that the MOT atom number was $N = 5.65(8) \times 10^6$, resulting in an expected $OD = 0.260(4)$ and a calculated fractional absorption of only 7 % for a probe beam addressing the $F = 1 \rightarrow F' = 2$ transition of the ^{39}K D_1 line. This number was only improved when 5.4 A was passed through the dispenser, reaching $N = 1.14(6) \times 10^7$ and $OD = 0.53(3)$, giving an

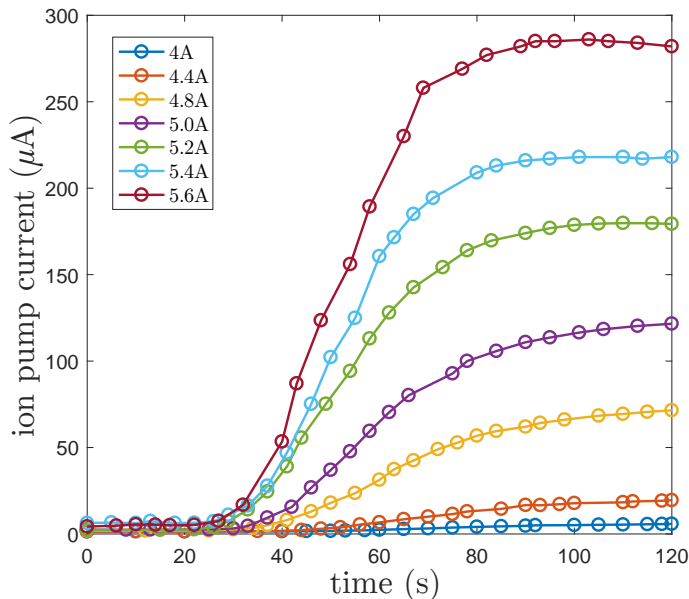


Figure 5.12: Ion pump current reading for various dispenser currents.

expected 14(1) % fractional absorption. For lower current values, we found that N and OD barely changed, or even got worse for cases between 3.0-4.8 A. After this measurement, whenever we fire-up the dispensers (once or twice a week maximum), we let 5.4 A to pass through the dispensers for slightly less than 90 s.

Heating the 2D-MOT chamber

Since the vacuum system was re-built, as described in Chapter 3, the dispensers cross has been continuously kept warm using a heating tape made out of silicon, operating at a temperature around 70°C . This was done in order to ensure that most of the released potassium would make it to the six-way cross serving as 2D-MOT chamber, before condensing. Even though the dispensers cross and the chamber were directly connected, the temperature at the centre of the chamber was found to only be $\sim 23^{\circ}\text{C}$, which was significantly lower than what was expected. We thus investigated if keeping the 2D-MOT chamber at a higher temperature would help us make a 3D-MOT with higher atom number and optical depth.

In order to heat the six-way cross, we used two heaters of the same type as the ones

used in the vapour cell experiment described in Chapter 4. The heaters were placed around two of the windows of the six-way cross, close enough to its centre. We varied the temperature of the heaters and monitored the temperature at the centre of the chamber using a thermocouple. Every time we changed the set temperature of the heaters, we waited for 30 minutes before taking pictures of the MOT, so that the system could reach thermal equilibrium.

Figure 5.13, shows the results of the measurement. We can see that the atom number almost triples as the temperature at the centre of the cross reaches $\sim 50^\circ\text{C}$ (heaters sensor at same time showed $\sim 70^\circ\text{C}$). In numbers, when the system was at 23°C , $N=4.4(4)\times 10^6$, resulting to an expected $OD = 0.19(4)$ and a calculated fractional absorption of only 5 % (again, for a probe beam addressing the $F = 1 \rightarrow F' = 2$ transition of the ^{39}K D_1 line). When at $\sim 50^\circ\text{C}$, $N=1.36(9)\times 10^7$, resulting to an expected $OD = 0.61(4)$ and a calculated fractional absorption of 16(1) %. Thus, the results were not as positive as expected, leading to some improvement of the parameters of interest but not to the desired degree.

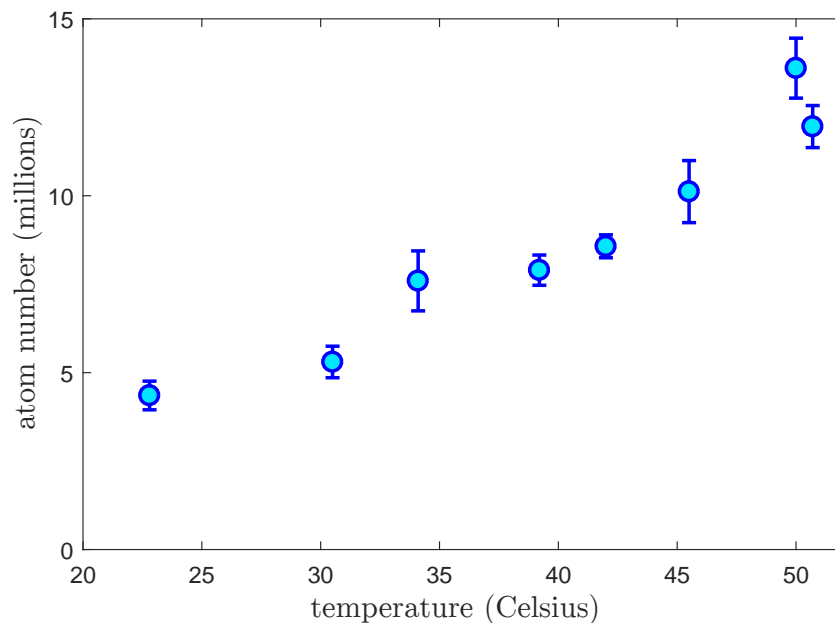


Figure 5.13: 3D-MOT atom number for different temperatures of the 2D-MOT chamber. Error bars represent standard deviations from eight different MOT pictures.

After the system was left at 50°C for 24 hours and was given time to fully heat up

and truly reach thermal equilibrium, the parameters appeared to be greatly improved. More specifically, we observed an atomic cloud with $N = 1.3(4) \times 10^8$ and $OD = 4.9(1.5)$ (fractional probe absorption 75(10) %).

Conclusion

We have investigated the effect of passing different currents through the dispenser and heating the 2D-MOT chamber at 50°C. It was the latter that significantly improved the parameters of interest for our experiment as it increased the atom number by approximately 30 times ($N_{\text{before}} = 4.4(4) \times 10^6 \rightarrow N_{\text{after}} = 1.3(4) \times 10^8$), and correspondingly the optical depth by one order of magnitude ($OD_{\text{before}} = 0.61(4) \rightarrow OD_{\text{after}} = 4.9(1.5)$).

5.4 Conclusion

This chapter discussed about magneto-optical traps, and in particular our ^{39}K MOT. Measurements and optimisations of the different cloud parameters such as the temperature, atom number and optical depth were presented. The most important results of the chapter are: first, the achievement of an atomic cloud with sub-Doppler temperature, and second, of a cloud with high atom number and optical depth. The former enables longer probing times and reduced two-photon Doppler broadening, both useful for EIT measurements. The latter, on the other hand, increases the strength of the collective light-matter interaction and is a key element for observing EIT in atom clouds.

Chapter 6

Strong light-matter interactions

The content presented here, such as figures and text, has partially been taken from [47]: R. Culver, A. Lampis, B. Megyeri, K. Pahwa, L. Mudarikwa, M. Holynski, P. W. Courteille and J. Goldwin, *Collective strong coupling of cold potassium atoms in a ring cavity*. New Journal of Physics **18** (11), 113043 (2016).

In this chapter, we study experimentally the interactions between the ring cavity light field and the cold potassium cloud intersecting with the cavity mode. The observation of splitting and avoided crossing of the normal modes, phenomena demonstrating collective strong coupling in our system, will be presented and discussed. This is the first experiment where (collective) strong coupling has been achieved with cold potassium atoms.

6.1 Experimental procedure

The experimental cycle followed in order to capture the normal-mode splitting and avoided crossing data, which will be presented shortly after, was the following: Firstly, we loaded the atoms in the MOT. The pushing beam was then blocked using a shutter and the repump beam was turned completely off for 100 μs to optically pump atoms into the $F = 1$ state. Then, the cooling beam was also turned off for another 100 μs , and simultaneously, the probe beam was turned on. The probe was then scanned across some frequency range

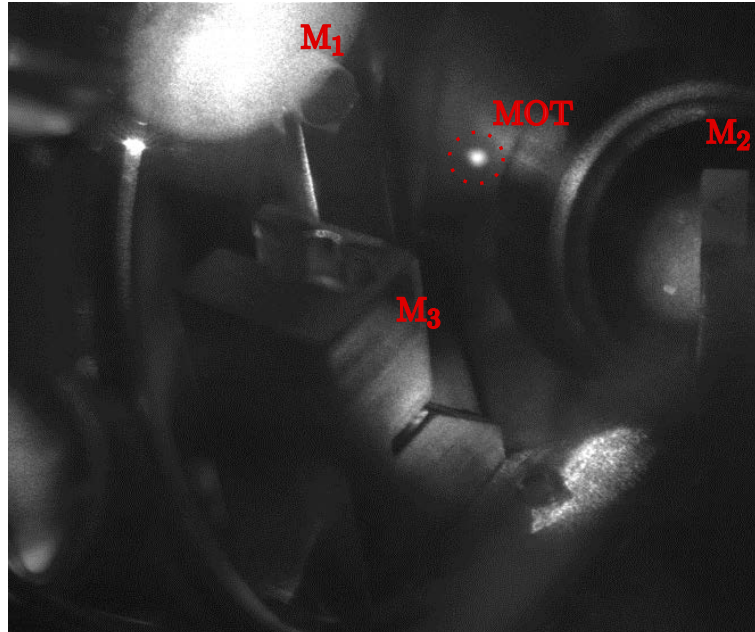


Figure 6.1: Photograph of the cavity and the MOT. By optimising the overlap between the cavity mode and the MOT it was possible to observe large normal-mode splitting.

($\delta_a = \omega_a - \omega_p$, ω_a and ω_p are the uncoupled atom's resonant frequency and the frequency of the probe beam, respectively), and was detected on an avalanche photodiode with a 3 dB bandwidth of 3 MHz¹. The probe signal was recorded on a digital oscilloscope, and the MOT and pushing beams were turned back on once the probe scan was finished.

A variable of particular importance for the experiment is δ ($\delta = \delta_c - \delta_a = \omega_c - \omega_a$, $\delta_c = \omega_c - \omega_p$, where ω_c is the resonant frequency of the bare cavity). The signature of strong coupling, the well-known normal-mode splitting, is evident when $\delta = 0$, whereas in the case δ is varied, the avoided crossing of the normal modes becomes apparent.

To ensure that the MOT and the cavity mode had a good overlap, prior to any measurements, the intensity of the probe beam was set to be high and the MOT was let to be continuously running. Also, δ was set to be close to zero. The MOT was then translated across the cavity mode using an additional magnetic field generated by a “shim” coil, placed on top of the vacuum chamber. What we were looking to see was the resonant probe light affecting the MOT (i.e. we were trying to diminish the MOT with the resonant

¹LASER COMPONENTS UK, LCSA500-03.

light), by imaging the system using cameras from different angles. An example image is shown in Figure 6.1. Once we could see the light depleting the MOT, we would then turn its intensity slightly down, and set the current passing through the shim coil to a new value, aiming to unload the MOT once more. This procedure was repeated up to the point that we could see the MOT being affected by even a very small amount of incident light. Then, the power of the probe was set to be very low (the intracavity intensity was below saturation intensity, but still detectable by the photodiode), and the experimental cycle of taking data could start.

It should be noted that the MOT coils (and the shim coil) were kept on during the entire experimental cycle. Additionally, from the time-of-flight measurements which revealed a MOT temperature of ~ 1 mK, it was found that the cloud does not expand during the first 100 μs (see for example Figure 5.5)². Therefore, we can assume that the density of the atomic cloud along the cavity mode remained almost unchanged during the measurements.

6.2 Parameters

The parameters that determine if and how much the normal-modes will ultimately split (in frequency), are the single atom Rabi frequency (g) and the number of atoms effectively interacting with the cavity mode (N), as described by the collective strong coupling parameter $G = g\sqrt{N}$. As we saw in section 3.3.2, for our experiment $g = 2\pi \times 91.5(5)$ kHz. As for N , it clearly depends on the MOT atom number (N_{TOT}), the cross-sectional area of the MOT (A_{MOT}), and that of the cavity (A_{CAV}), but also on the relative strength of the transition (ξ) under consideration. For optimal MOT positioning, $N = N_{\text{TOT}} \times \xi \times \frac{A_{\text{CAV}}}{A_{\text{MOT}}}$ [143], and as we are probing on the $F = 1 \rightarrow F' = 2$ transition of the D_1 line, $\xi = 5/18$.

²The further cooling procedure was implemented months after this measurement was made.

6.3 Results

Data captured using the experimental procedure explained above will be shown here. Two different measurements will be presented, one where $\delta = 0$ and the increment of N makes the normal-mode splitting first apparent and then larger, and yet another one where N is kept constant while δ is varied, revealing the avoided-crossing. Both measurements were done with weak probe light of ~ 1 nW incident power³.

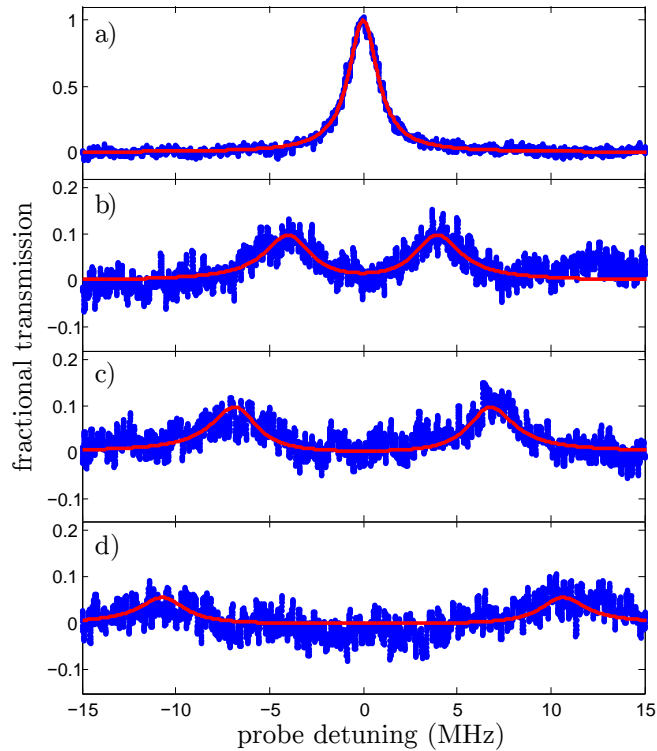


Figure 6.2: Normal-mode splitting for various effective atom number and $\delta = 0$. Spectra here are averaged 32 times before storage. a) Cavity transmission spectrum when no atoms are in the cavity mode. Red line is a Lorentzian fit to the data. b-d) The normal-mode of the cavity splits. Data are fitted to the transmission equation (equation 2.21, with g replaced by G), revealing $G = 2\pi \times [4.2(4), 6.9(1.3), 10.7(5.9)]$ MHz for b), c) and d) respectively. Uncertainties here represent standard error from the fits.

For the first measurement, N was varied by translating the MOT in and out the cavity mode using the magnetic field generated by the shim coil. Example spectra are shown in Figure 6.2.

³This power corresponds to < 1 mW/cm² intracavity intensity at the minimum waist.

Fits to equation 2.21 describing the cavity transmission for the coupled atom-cavity system give $G = 2\pi \times [4.2(4), 6.9(1.3), 10.7(5.9)]$ MHz, which translates in the language of effective atom number as $N = 2.08(2) \times 10^3, 5.67(20) \times 10^3, 1.36(42) \times 10^4$ for spectrum b), c) and d) respectively. The signal to noise ratio for these data is not great and this is the main reason the errors are not small.

For the second measurement, the cavity was detuned from the atomic resonance. Figure 6.3a) shows the transmission signal for different cavity-atom detunings δ . The spectra here are normalised to the maximum incident probe power. In order to track the position of the peaks, the spectra are fitted with simple Lorentzians. For far-detuned data, it is expected to have different fit accuracy for the two peaks since their size is vastly different; one of the peaks is easy to distinguish while the other one is barely visible. Plotting the centre frequencies of the peaks for different δ values reveals the avoided crossing of the normal modes as it is evident from Figure 6.3b).

The data here are fitted using the following equation [144]:

$$\delta_a^\pm = \frac{\delta_a - \delta_c}{2} \pm \sqrt{G^2 + \left(\frac{\delta_a - \delta_c}{2}\right)^2} . \quad (6.1)$$

This can be derived by using equation 2.13a, the fact that $\delta = \delta_c - \delta_a$, and replacing g by G (since we are considering atomic ensembles). The fit shows that $G = 2\pi \times 19.1(1.6)$ MHz, which implies that $N = 4.36(3) \times 10^4$. This was the largest splitting observed in our experiment and corresponds to a collective cooperativity $C_N = G^2/\kappa\gamma = 133(23)$.

6.4 Discussion and conclusion

The results presented in this chapter show that our system lies deeply in the collective strong coupling regime and set the foundation for studying cavity quantum electrodynamics with steep dispersion [145]. This is in fact the first time this has been achieved in potassium. A few additional notes and comments about the results follow.

The first point we should raise is the fact that independent calculation of the MOT

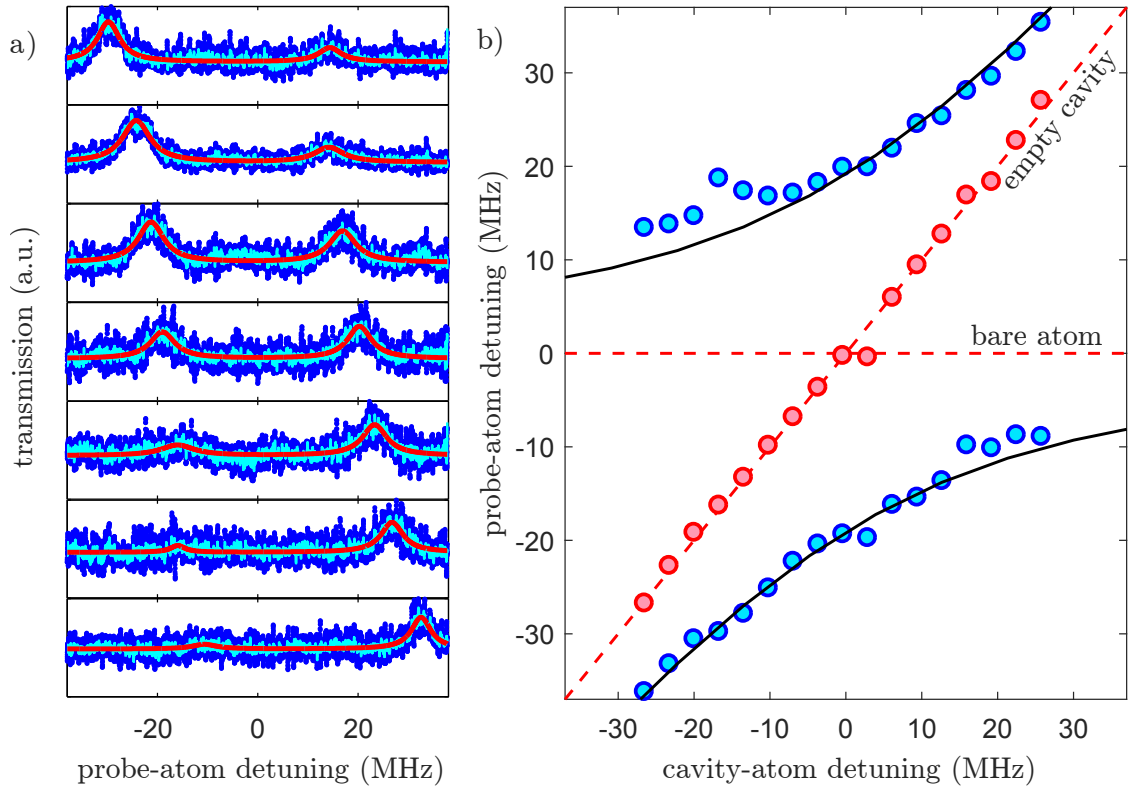


Figure 6.3: Avoided crossing of the normal modes. a) Several transmission spectra are shown for increasing cavity-atom detunings. Actual and filtered data, and Lorentzian fits to the filtered data (*sgolayfilt* was used to smooth out the data), are in blue, cyan and red, respectively. b) Blue circles represent the normal-mode resonance frequencies whereas black curves are fits to equation 6.1, showing that $G = 2\pi \times 19.1(1.6)$ MHz. Number in brackets here represents standard error arising from fits to the data. Red circles show data without atoms.

atom number by fluorescence image analysis always suggests fewer atoms in our trap than what the observed normal-mode splitting implies. We can only speculate the reasons that could lead to this discrepancy. One reason could be the assumption we made in our image analysis that the full aperture of the imaging lens contributes to the MOT light collection. This would lead to an underestimation of the calculated atom number. Another reason could be that ξ (the transition strength) is not exactly $5/18$ as it was assumed to be in our calculations. The $5/18$ value results after averaging the oscillator strength over all of the $F = 1 \rightarrow F' = 2$ transitions. In order to completely understand why this discrepancy appears, further experimental and theoretical work should be carried out, which is beyond the scope of this thesis.

Furthermore, we should note that the probe intensity is not the same all along the frequency scan. This is obvious from Figure 6.3a) where one of the peaks almost vanishes when δ is no longer zero. Of course, this difference between the height of the peaks is expected when the cavity is detuned from the uncoupled atomic resonance (see Chapter 2) but in our case this is more pronounced. The reason we observe this is the finite AOM tuning bandwidth. We plan on building an active feedback control system in the future in order to equalise the probe intensity across the range of the frequency scan.

Additionally, as it can be seen from Figure 6.3a) and b) the Lorentzian fits to the data are more accurate when the detuning is close to zero. When this is not the case, it is obvious that the Lorentzian fit only manages to accurately determine the centre frequency for one of the peaks (with the greater amplitude) and at the same time struggles to determine the other's (with the smaller amplitude). This is reflected by the fits of the extracted normal-mode resonance frequencies using equation 6.1.

Finally, the results presented in this chapter were generated long before it was decided to heat the 2D-MOT chamber and further cool the atomic cloud. At that time, the atom number was lower than what it has been since the chamber has been kept at higher temperatures, and the cloud temperature was about one order of magnitude higher. Since then, the typical number of atoms in our trap is $\sim 10^8$ which in combination with an RMS size of $\sigma \sim 1$ mm would have resulted to $N \approx 8 \times 10^4$, hence $G \approx 2\pi \times 26$ MHz and $C_N \approx 240$. Unfortunately, as our priority at the time was to achieve EIT in the cold, in-cavity atoms, no data showing normal-mode splitting with this atom number were actually collected.

Chapter 7

Towards controllable dispersion with cold in-cavity atoms

After achieving strong light-matter interactions, we now move our focus in controlling the group index of refraction (n_g) of the cold, in-cavity, atomic medium. We implement the EIT technique on the atom cloud, present our measurements and discuss possible limitations they reveal about the system.

7.1 Setting the scene

The achievement of collective strong coupling sets the foundations for realising a system with controllable n_g . In such a system, when the cavity and atom are at resonance and probed by a weak beam, the normal-mode of the cavity splits, and at zero probe detuning the cavity transmission goes to zero (as we have seen in Chapter 6). When an intense coupling beam, forming a Λ -system with the probe, is also shone on the cloud of atoms, transparency at zero detuning can be attained. This modification of the medium's optical thickness (as seen by the probe) arises from the coherent interaction between the probe and the coupling beam (as discussed and explained in Chapter 2, and experimentally shown in a vapour cell in Chapter 4). The real part of the system's susceptibility has a

feature with peak to peak amplitude and slope that depends on the height and the width of the transparency peak, respectively. For instance, a peak which is tall and narrow can lead to very high group indices.

Ideally, one could realise EIT in the cold in-cavity potassium cloud simply by applying the experimental procedure followed to observe strong light-matter coupling and turning on the coupling beam. However, it has proved to be much more complicated in practice. As such, after several unsuccessful attempts, it was decided to try to observe EIT by probing the cold atoms from the “side” (i.e. probing the atoms directly, from the side of the cavity) before moving towards the ultimate goal of achieving EIT with the atoms in the cavity. Probe transmission measurements through the atom cloud, with the added coupling beam turned on, are next presented.

7.2 Probing the cold cloud of atoms

An essential requirement to observe EIT is having probe absorption at resonance (in the absence of the coupling beam), and as we know, the amount of probe absorption in an atom cloud depends on its optical depth (OD^1). For the measurements we are going to present in this chapter, the optical depth of the cloud was approximately 3 (and its temperature near $130 \mu\text{K}$; both a result of the optimisations discussed in Chapter 5). This OD translates to a greater than 55 % fractional absorption of a weak resonant probe beam addressing the $F = 1 \rightarrow F' = 2$ transition of the D_1 potassium line.

7.2.1 Experimental details

The experimental procedure followed in order to capture EIT spectra was nearly identical to that described in Chapter 6 (followed to capture the normal-mode splitting). The few differences were that it did not include locking and probing the ring cavity (since we did

¹As discussed in Chapter 5, $OD = \ln\left(\frac{I_0}{I}\right)$, where I_0 is the intensity of the a light beam prior entering the atomic medium and I is the intensity of the transmitted light.

not use the cavity for this measurement), the inclusion of the MOT cooling stage, and the addition of the strong coupling beam resonant with the $F = 2 \rightarrow F' = 2$ transition (beams involved to form the EIT system have identical frequencies to those used in the vapour cell experiment in Chapter 4) during the probe frequency scan².

More specifically, we firstly load $\sim 10^8$ atoms in our MOT. We then block the push beam and abruptly jump parameters such as the total MOT beams' peak intensity, and the detuning of the cooling beam for 2 ms, which is the duration of the cooling stage described in Chapter 5. Then, for 100 μ s we turn off the repump beam in order to optically pump the atoms into the $F = 1$ state. Immediately afterwards, the cooling beam is also turned off and instantaneously the probe and coupling beams are turned on for typically 100 μ s. During this period we scan the probe across a ~ 30 MHz range around resonance. We then collect the probe light using an avalanche photodiode³, specified with 50 MHz bandwidth. The repetition rate of the experiment is 5 Hz which allows enough time for the MOT to load before each measurement. The 3D-MOT magnetic field was kept continuously on during the entire experimental cycle, for three reasons. First, because the issue with the cavity oscillations whenever the 3D-MOT coils were being switched on/off (discussed in Chapter 3) was not solved, and we ultimately wanted to apply this technique in the main experiment. Secondly, because whenever the field was switched off, the cloud was shifted away from the probe beam. This shifting was caused by stray magnetic fields, for example the Earth's, which at the time of these measurements we had no attempt to cancel. This meant that the OD and absorption experienced by the probe was reduced. Thirdly, even if we ignored the issue with the cloud shifting, since the temperature of the cloud (after the cooling stage) was optimised with the 3D-MOT magnetic field being on, then, in order to have a sub-Doppler cooled atomic cloud, the temperature optimisation should be re-done (this time with the field off). EIT experiments where the magnetic field is kept on during measurements are not uncommon and have been studied in the past [146].

²The shim coil previously used to optimise the MOT overlap with the cavity mode was also not used here.

³Thorlabs, APD110A.

Probe and coupling beams

The probe and coupling beams had $1/e^2$ intensity diameters of ~ 2.0 mm and ~ 7.5 mm, respectively. Furthermore, the probe beam intensity was set to be well below atomic saturation, but still giving a spectrum with good signal to noise ratio. The two beams had $\text{lin}\perp\text{lin}$ polarisation (combined on a PBS) and were aligned to approximately co-propagate (they had a small relative misalignment so that the coupling beam was not being collected by the photodetector). As the two beams co-propagate (as in Chapter 4), and we consider cold atoms, we expect Doppler effects to be insignificant for our system. The polarisation of the beams was chosen to be linear, which is required for when we ultimately apply this technique to the ring cavity experiment. For the $\text{lin}\perp\text{lin}$ configuration we expect EIT features with high transparency.

In order to understand why $\text{lin}\perp\text{lin}$ should result in high attainable transparency we have to take into consideration the different Λ sub-systems that contribute to the EIT process. We choose the quantisation axis to be the same as the polarisation of the probe beam. This is a natural choice here as the magnetic field of the 3D-MOT changes direction throughout the atomic cloud and the atoms are not polarised. Then we can choose the coupling to have parallel or perpendicular polarisation with respect to the probe. If the former is the case, both the probe and the coupling beams address π transitions. As can be seen in Figure 7.1a), this results to an EIT system which is not closed. More specifically, the probe beam addressing the $|F = 1, m_F = 0\rangle \rightarrow |F' = 2, m_F = 0\rangle$ transition does not have a coupling counterpart (as $|F = 2, m_F = 0\rangle \rightarrow |F' = 2, m_F = 0\rangle$ is not allowed by selection rules considerations). Hence, we effectively have a system composed of three- and two-level subsystems, where the resulting EIT signal is a Lorentzian shaped absorption profile with an EIT profile on top [146]. On the other hand, if we consider the $\text{lin}\perp\text{lin}$ configuration, as in Figure 7.1b), we have a linear coupling beam, which can be seen as the coherent sum of σ_+ and σ_- polarised light. This leads to a system composed by a number of Λ -subsystems which are all closed, since all the transitions addressed by the

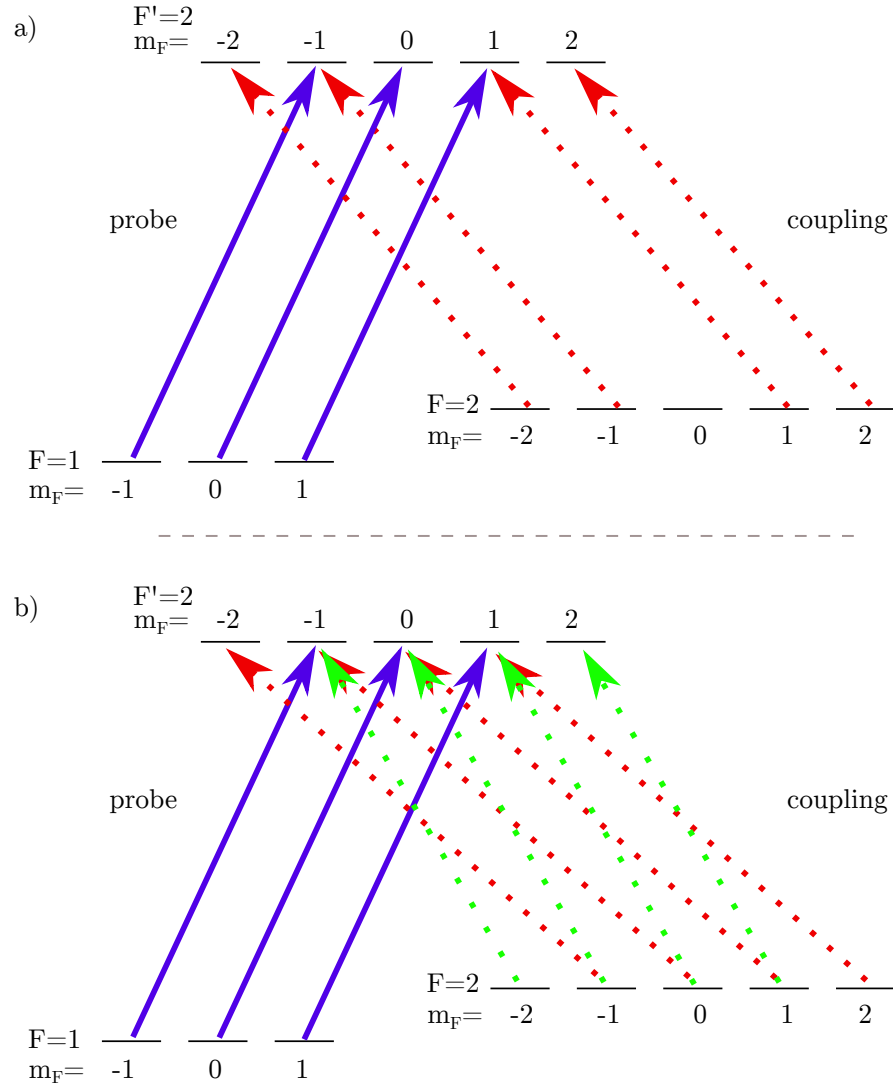


Figure 7.1: A sub-systems for different probe-coupling polarisation configurations. a) The probe and coupling beams both have π polarisation. b) The probe and coupling have π and σ_{\pm} polarisation, respectively; green(red) arrows indicate $\sigma_{+}(\sigma_{-})$ polarisation.

probe beam also have a coupling counterpart. This should lead to an EIT signal with high transparency⁴.

7.2.2 Results and discussion

Example spectra for different powers of the coupling beam are shown in Figure 7.2a). For these spectra, OD was ~ 3 , and the cloud temperature was $\sim 130 \mu\text{K}$ (as aforementioned).

⁴For the case that the coupling beam was chosen to have circular polarisation with respect to the linear probe, then the coupling would be a combination of σ_{\pm} and π light, which once again results to a

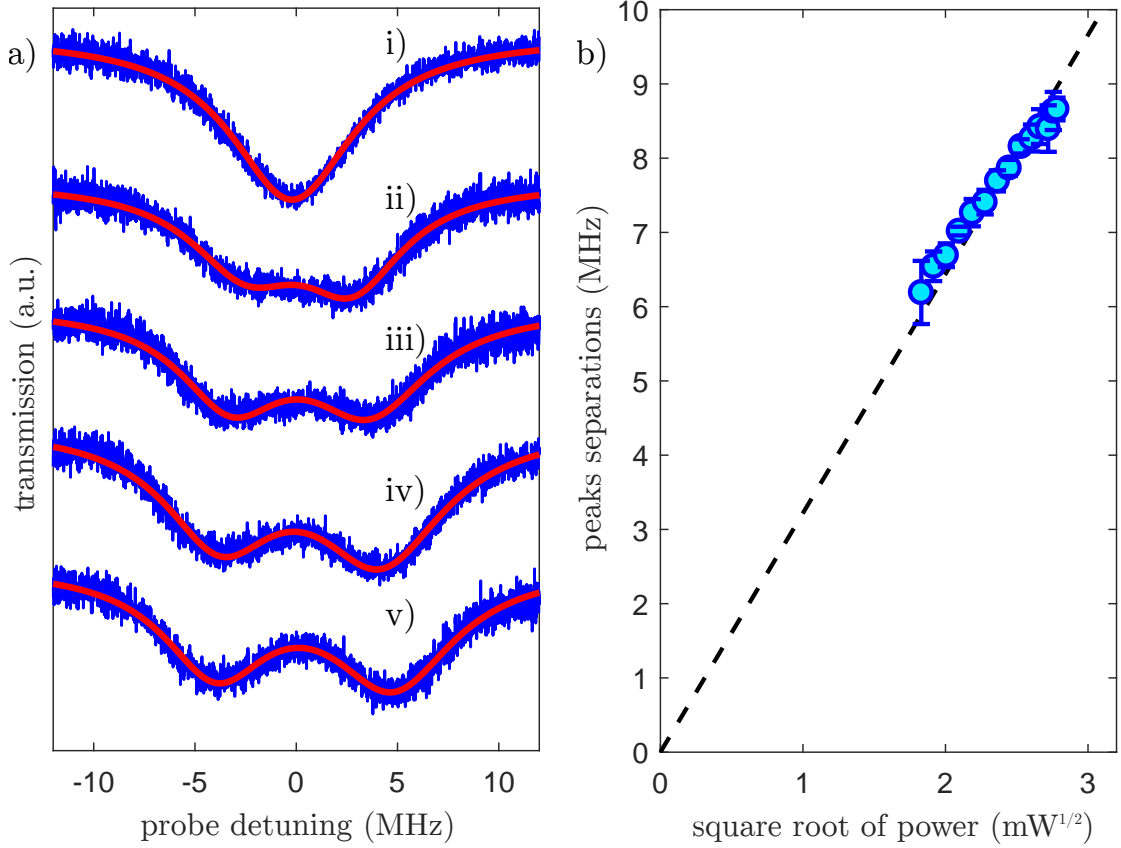


Figure 7.2: Absorption line splitting. a) Probe transmission spectra. As the coupling power increases from i) to v) a peak (or splitting of the absorption line) at zero probe detuning becomes more pronounced. Data are fitted using a function which is the sum of two Lorentzians. The square root of coupling power for spectra i), to v) is (0, 1.4, 2.0, 2.4, 2.8) $\text{mW}^{1/2}$, respectively. b) Absorption peaks' separation as a function of the square root of coupling power. Each blue circle represents the average of three fitted spectra, at a certain coupling power. Error bars here represent standard deviation. Dashed black line is a linear fit with intercept forced as 0 to the blue data giving a slope of $3.22(3) \text{ MHz}/\text{mW}^{1/2}$, where the number in the parenthesis is the standard error from the fit.

Fitting the spectrum for which no coupling beam is present (spectrum i)) to a Lorentzian, it was found that the FWHM linewidth of the absorption peak was $6.93(11) \text{ MHz}$, which is broader than the natural line width of D_1 line of ^{39}K ($\Gamma = 5.96 \text{ MHz}$) [86] by approximately 1 MHz. This is not unexpected for a number of reasons we discuss below. First and most important parameter contributing to the broadening of the observed absorption line is the inhomogeneity of the magnetic field across the cloud, since the field was left on during the measurement. The maximum variation of the Zeeman shift (Δ_Z) across an effectively closed system.

the cloud was calculated. We know that the different levels tune by $g_F m_F \mu_B B$ (where g_F is the Landé g -factor, m_F is the projection of F , $\mu_B = 2\pi\hbar \times 1.4 \text{ MHz/G}$ is the Bohr magneton, and B is the magnetic field, as also discussed in Chapter 4), and g_F for the $F = 1(2)$ ground state is $-1/2(1/2)$ and for the $F' = 1(2)$ excited state is $-1/6(1/6)$. Our probe beam has π polarisation, thus we calculate the maximum Zeeman shift corresponding to the $|F, m_F = 1(-1)\rangle \rightarrow |F', m_F = 1(-1)\rangle$ transition to be $\Delta_Z/B = 0.93 \text{ MHz/G}$. Since the gradient of the 3D-MOT field is 8 G/cm , meaning 0.8 G variation over the 1 mm long atomic cloud, we estimate $\sim 0.75 \text{ MHz}$ excess broadening due to the field being on during the measurement. Here, we have assumed the Earth's magnetic field gradient to be uniform along the cloud and therefore not contributing to the overall dephasing of the system. But, we should note that as long as we do not eliminate it, then we should expect it to always contribute to the value of the observed linewidth as it perturbs the energies of the involved states (just like when we used the solenoid to split the EIT peak into three peaks in Chapter 4). Furthermore, we calculate the single-photon Doppler broadening (Δ_D) for the $130 \mu\text{K}$ cloud to be 0.51 MHz (and 1.42 MHz for a 1 mK cloud) and accordingly adding $\sim 0.1 \text{ MHz}$ to the observed linewidth of the absorption curve. Lastly, we can also ascribe up to $\sim 0.3 \text{ MHz}$ broadening due to the (specified) linewidth of the probe laser (Δ_L).

When the coupling beam power was set to be non-zero, but still low, no EIT resonance was observed. As the coupling power (P_c) was increased, a transparency feature appeared at resonance. However, one could claim that the observed spectra look more closely related to Autler-Townes splitting (ATS), which is a splitting of the absorption line [78], rather than an induced transparency caused by EIT (a phenomenon that should be observable no matter how weak the coupling beam is; see for instance Figure 4.3 in Chapter 4). ATS happens when an intense beam with Rabi frequency Ω_c , where $\Omega_c \gg \Gamma$ (Γ is the FWHM atomic linewidth), is applied on the atoms, and causes the absorption profile of an atomic transition to split; it does not require the probe and coupling beams to coherently interact. It has been a matter of great discussion of how to distinguish between EIT

and ATS related features [147], especially when we also consider dephasing (γ_{21}) between the states addressed by the probe and coupling fields. For the purposes of this thesis we should limit this discussion to one condition: if $\Gamma \gg \Omega_c \gg \sqrt{\Gamma \times \gamma_{21}}$ [74], then we should be able to observe transparency features which are caused by EIT (i.e. narrow resonances at weak coupling beam powers). However, if $\gamma_{21} \geq \Gamma$, then it is only possible to observe features associated with ATS.

Doppler shift contributions to EIT features when the probe and coupling beams co-propagate are almost zero⁵. In combination with our observations and calculations for the spectrum where the coupling beam is absent, we come to the conclusion that γ_{21} should be approximately 1 MHz due to contributions from the Zeeman shifts Δ_Z and the laser linewidth Δ_L . Therefore, our observed transparency features should satisfy the EIT condition and it should have been possible to observe EIT features for our system. The reason we do not observe induced transparency at low coupling powers remains unclear.

The FWHM linewidth of the transmission peak, for $\sqrt{P_c} = 2.8 \text{ mW}^{1/2}$ (example spectrum v)) was found to be equal to 5.73(20) MHz, and its fractional transmission⁶ $T = 59(4) \%$, after fitting it to a Lorentzian⁷. Even though Ω_c is high and the polarisation of the beams since they are overlapped on a PBS, almost perfectly perpendicular, the attained transparency is far from 100 %. This implies that decoherence strongly affects our system.

We fitted the spectra shown in Figure 7.2a), using the sum of two Lorentzian functions. Then, we determined the separation of the absorption peaks and plotted them as a function of the square root of the coupling beam power, as shown in Figure 7.2b). As can be seen from this figure, it was only possible to fit the spectra and get a value for the peaks' separation when the separation got larger than Γ . The separation of the peaks should correspond to the Rabi frequency of the coupling beam (Ω_c), in ATS related phenomena.

⁵We calculate a very small broadening of 0.6 Hz for a cloud with 130 μK temperature and 1.7 Hz for 1 mK.

⁶Defined as the ratio of change in absorption of a weak probe beam when a coupling beam is also present, to the absorption of the probe when no coupling beam is present, as in Chapter 4.

⁷These values are the average of three spectra and numbers in brackets represent standard deviations.

In general, the Rabi frequency can be defined as [148],

$$\Omega = \sqrt{\frac{I}{2I_s}} \Gamma \quad , \quad (7.1)$$

where I is the light intensity and I_s is the saturation intensity of the atom (taking into account the transition strengths). From that we calculate $\Omega_c/\sqrt{P_c} = 3.614 \text{ MHz/mW}^{1/2}$. Fitting the experimental data with a straight line with an intercept forced as 0, a slightly shallower slope of $3.22(6) \text{ MHz/mW}^{1/2}$ is obtained.

The experiment was repeated for the case that the further cooling stage was not included in the experimental sequence (i.e. the MOT temperature was $\sim 1 \text{ mK}$, but the optical depth was higher; $OD \sim 4.5$), and for the case that the 3D-MOT coils were shut off during the probe scan (this resulted in lower but still visible probe absorption). Both, failed to improve our results. Furthermore, in order to investigate the possibility of something going wrong with the laser system, we shone the probe and coupling beams on the heated potassium vapour cell, instead of on the MOT. When the cell was magnetically shielded, EIT features with similar width and transparency to those described in Chapter 4, were reproduced. When the cell was left unshielded, the width of the features was found to be almost five times broader. More specifically, for a coupling beam with power $P_c = 1.2 \text{ mW}$, the EIT width (HWHM) for the shielded and unshielded cell was found to be $154(14) \text{ kHz}$ and $710(52) \text{ kHz}$, respectively. The observed broadening is a consequence of the earth's magnetic field which partially splits the EIT peak (again, as seen in Chapter 4).

7.3 Getting to EIT with cold in-cavity atoms

The results presented in this chapter highlight the need of eliminating decoherence in our system in order to achieve our ultimate goal of intracavity EIT with cold atoms. Towards this goal, most importantly the issue of the 3D-MOT field which could not be shut off during the probing period, should be addressed. Furthermore, the stray

magnetic fields should be compensated. It has already been mentioned in Chapter 3 that efforts towards eliminating the effects of the coils' shut-off on the ring cavity, that will allow us to effectively do the former, have been made. Regarding the stray fields' proper compensation, the PhD students currently working on the experiment have built a cage composed of six coils, a pair of coils in each direction, dedicated to do that. Once we overcome those two issues, we expect to see narrower EIT resonances with higher fractional transmission than those we have observed in the EIT vapour cell experiment (Chapter 4). The reason we should expect narrower resonances is the fact that transit-time broadening that was limiting us in the vapour cell should now be negligible. Furthermore, higher fractional transmission is expected since in the cold atoms experiment the Doppler shifts are largely suppressed and the majority of the atoms participate in the formation of an effectively closed Λ system with no residual probe absorption. This was not possible in the vapour cell experiment, where the Doppler broadening was on the order of the ground-state splitting and unavoidably the number of atoms forming closed Λ sub-systems drops.

Chapter 8

Conclusions and outlook

In summary, this thesis has described work in an experiment set up in a Cold Atoms' laboratory at the University of Birmingham, where studies of cQED and EIT in a system composed of cold potassium atoms and a ring cavity were combined. Both, cQED and EIT rely on the coherence of light-matter interaction to be observed.

The thesis began by outlining the fundamental background theory required to understand the different experiments and measurements presented in the rest of the chapters. The experimental apparatus was also described with particular focus on the ring cavity and other work that took place during the period of this PhD. Then, the thesis split into a discussion of two experiments; first a “hot atoms” experiment and then the (main) cold atoms experiment.

In the first experiment, the EIT technique was applied in a heated potassium vapour cell. Studying EIT in an atomic vapour proved to be very useful to understand the underlying mechanism of the technique and its relevant experimental requirements prior applying it in the main experiment. EIT resonances with deeply sub-natural linewidths were generated for which group indices (n_g) as large as 6330(160) were calculated. Additionally, by using a longitudinal magnetic field to split the EIT feature into different components, we demonstrated that both $\text{lin}\parallel\text{lin}$ and $\text{lin}\perp\text{lin}$ probe-coupling beam polarisations exhibit magneto-optical anisotropy. Using a novel heterodyne measurement of the

circular dichroism we also showed that the relative probe-coupling polarisation results in an induced anisotropy of different magnitude.

After the description of the vapour cell experiment, the thesis moved to the cold atoms part and discussed the details of our ^{39}K MOT. Results showing that sub-Doppler temperatures can be achieved even when the 3D-MOT field is kept constantly on during the experiment were presented. Furthermore, the dependence of the physical properties of the 3D-MOT, such as optical depth (OD) and atom number (N), on the temperature of the 2D-MOT chamber was clearly shown. The optimisations described in this chapter not only lowered the MOT temperature by one order of magnitude, but also increased its atom number and optical depth by approximately one order of magnitude. A MOT with $N = 10^8$ and $OD = 3$ at $130 \mu\text{K}$, was typical for our experiment after the optimisations described in this chapter were done.

Following, the first demonstration of collective strong coupling with potassium atoms was presented. The footprint of the experiment lying in this regime was the observation of the normal-mode splitting and avoided crossing of the normal modes with $G = 2\pi \times 19.1(1.6)$ MHz, implying $4.36(3) \times 10^4$ atoms interacting collectively with the mode of the ring cavity. These results were taken prior to the further optimisations in the atom number in the MOT, which would have resulted to $G \sim 2\pi \times 26$ MHz.

In the last chapter of the thesis, work towards achieving EIT in the strongly coupled system was discussed. By directly addressing the cold atoms with the EIT beams, no induced transparency features were observed for low coupling beam powers. However, for high power coupling beams $\Omega_c > \Gamma$ (Ω_c is the Rabi frequency associated with the coupling beam and Γ is the natural linewidth), the absorption line was found to split. This suggests that decoherence strongly affects our system. We ascribe this decoherence to mainly arise from the 3D-MOT magnetic field which was kept on during measurements. Therefore, it should be made possible to switch off the 3D-MOT magnetic field during measurements (without causing mechanical oscillations in the cavity frame), in order to observe EIT resonances in the experiment. As such, since my departure from the lab, intensive work

to resolve this issue has been done.

After EIT is observed in the ^{39}K MOT, the experiment should be repeated by probing the atomic cloud with the cavity light. We plan to use the same polarisation configuration as in Chapter 7 (i.e. $\text{lin}\perp\text{lin}$), with the coupling beam set to almost co-propagate with the probe beam. The modification of the group index of the atomic medium should then be evident by cavity ring-down measurements. This is the immediate, next goal of this experiment. As it has been predicted [149] and demonstrated [150], the photon lifetime (τ_c) in a cavity is governed by the group velocity and as such we expect τ_c to be increased by n_g .

List of publications

- A. Lampis, R. Culver, B. Megyeri and J. Goldwin, *Coherent control of group index and magneto-optical anisotropy in a multilevel atomic vapor*. Optics Express **24** (14), 15494–15505 (2016).
- R. Culver, A. Lampis, B. Megyeri, K. Pahwa, L. Mudarikwa, M. Holynski, P. W. Courteille and J. Goldwin, *Collective strong coupling of cold potassium atoms in a ring cavity*. New Journal of Physics **18** (11), 113043 (2016).
- A. Lampis, R. Culver, B. Megyeri, G. Harvie and J. Goldwin, *Strong light-matter coupling with cold potassium atoms in a ring cavity*, in Quantum Information and Measurement (QIM) 2017, Optical Society of America, QT2A.1 (2017).
- B. Megyeri[‡], A. Lampis[‡], G. Harvie, R. Culver and J. Goldwin, *Why material slow light does not improve cavity-enhanced atom detection*. Journal of Modern Optics **65** (2), 185–191 (2017).

[‡]Equal contribution.

Appendix A

Derivations

Reproducing equations from physics books is often non-trivial. Here, a number of equations that have been used in this thesis will be derived in an attempt to make everything more transparent to the reader.

A.1 Unitary transformation

The step between equation 2.9 and 2.10 in Chapter 2, requires a unitary transformation where $U = e^{-iH_A t/\hbar} = |e\rangle\langle e| e^{-i\omega_a t} + |g\rangle\langle g|$. Here, we show how the operator can be written in the latter form. The derivation follows:

$$U = e^{-i\omega_a |e\rangle\langle e| t} \quad (\text{A.1a})$$

$$= \sum_{n=0}^{\infty} \frac{(-i\omega_a |e\rangle\langle e| t)^n}{n!} \quad (\text{A.1b})$$

$$= 1 + \sum_{n=1}^{\infty} |e\rangle\langle e| \frac{(-i\omega_a t)^n}{n!} \quad (\text{A.1c})$$

$$= 1 + (|e\rangle\langle e| - |e\rangle\langle e|) + \sum_{n=1}^{\infty} |e\rangle\langle e| \frac{(-i\omega_a t)^n}{n!} \quad (\text{A.1d})$$

$$= \underbrace{1 - |e\rangle\langle e|}_{|g\rangle\langle g|} + \underbrace{|e\rangle\langle e| + \sum_{n=1}^{\infty} |e\rangle\langle e| \frac{(-i\omega_a t)^n}{n!}}_{|e\rangle\langle e| \left(1 + \sum_{n=1}^{\infty} \frac{(-i\omega_a t)^n}{n!}\right)} \quad (\text{A.1e})$$

$$= |g\rangle\langle g| + |e\rangle\langle e| \left(1 + \sum_{n=1}^{\infty} \frac{(-i\omega_a t)^n}{n!}\right) \quad (\text{A.1f})$$

$$= |g\rangle\langle g| + |e\rangle\langle e| e^{-i\omega_a t} \quad (\text{A.1g})$$

As it is obvious, for this derivation we Taylor expanded (A.1b), “added zero” (A.1d) and used the completion relation (A.1f) in order to get the equation to the form we require.

A.2 Schrödinger equation in the rotating basis

Here, the steps followed in order to derive equation 2.52 will be shown in detail. Our starting point will be the Schrödinger equation:

$$\tilde{H}_{EIT} |\tilde{n}\rangle = i\hbar \frac{\partial}{\partial t} |\tilde{n}\rangle \quad (\text{A.2a})$$

$$= i\hbar \frac{\partial}{\partial t} (\tilde{U} |n\rangle) \quad (\text{A.2b})$$

$$= i\hbar \left(\frac{\partial \tilde{U}}{\partial t} |n\rangle + \tilde{U} \frac{\partial |n\rangle}{\partial t} \right) \quad (\text{A.2c})$$

$$= i\hbar \left(\frac{\partial \tilde{U}}{\partial t} |n\rangle - \frac{i}{\hbar} \tilde{U} H_{EIT} |n\rangle \right) \quad (\text{A.2d})$$

$$= i\hbar \left(\frac{\partial \tilde{U}}{\partial t} \tilde{U}^\dagger \tilde{U} |n\rangle - \frac{i}{\hbar} \tilde{U} H_{EIT} \tilde{U}^\dagger \tilde{U} |n\rangle \right) \quad (\text{A.2e})$$

$$= \left(i\hbar \frac{\partial \tilde{U}}{\partial t} \tilde{U}^\dagger + \tilde{U} H_{EIT} \tilde{U}^\dagger \right) \tilde{U} |n\rangle \quad (\text{A.2f})$$

$$= \left(i\hbar \frac{\partial \tilde{U}}{\partial t} \tilde{U}^\dagger + \tilde{U} H_{EIT} \tilde{U}^\dagger \right) |\tilde{n}\rangle \quad (\text{A.2g})$$

$$\implies \tilde{H}_{EIT} = i\hbar \frac{\partial \tilde{U}}{\partial t} \tilde{U}^\dagger + \tilde{U} H_{EIT} \tilde{U}^\dagger \quad (\text{A.2h})$$

The steps are more or less self-explanatory. We substitute $|\tilde{n}\rangle = \tilde{U} |n\rangle$ in (A.2a) in order to get to (A.2b). Then, we get from (A.2c) to (A.2d) by using that $\frac{\partial |n\rangle}{\partial t} = \frac{H_{EIT} |n\rangle}{i\hbar}$. We multiply the terms by the unitary operator $\tilde{U}^\dagger \tilde{U}$ in (A.2e) and from there it is trivial to get to the relationship stated in (A.2h).

Appendix B

Calculations

A couple of calculations used in this thesis are shown and explained here.

B.1 Transit-time broadening

In order to calculate the contribution of transit-time broadening (TB) to the total linewidth of the EIT resonance, we employ the equation derived by [99]:

$$TB \text{ (HWHM)} = \frac{\ln(2)u}{2\pi w} = \frac{\ln(2)}{2\pi w} \sqrt{\frac{2k_B T}{M}} \quad , \quad (\text{B.1})$$

where u stands for the atoms' thermal speed, w is the $1/e^2$ intensity radius of the beams (here, the two beams have the same size), k_B is the Boltzmann constant and M is the mass of the atoms (i.e. $M = 38.96370668(20) \times$ atomic mass unit [134]).

This formula was derived by making the assumptions that: a) the ground states are almost degenerate (this holds as long as the frequency splitting of the states is small compared to the transition frequency from either ground state to the excited state) and b) the lifetime of the excited state is short, and the lifetime of the ground states long, compared to TB . For our system, both of these assumptions seem to hold.

B.2 Number density

We calculate the number density \mathcal{N} in our potassium cell, containing 93.3 % of ^{39}K and 6.7 % of ^{41}K by firstly using the following simple equations to calculate the vapour pressure in either the solid or liquid state [142],

$$\log(p/\text{Pa}) = 9.967 - 4646 \times T^{-1} \quad (\text{solid}) \quad (\text{B.2})$$

$$\log(p/\text{Pa}) = 9.408 - 4453 \times T^{-1} \quad (\text{liquid}) \quad . \quad (\text{B.3})$$

The melting point of potassium is 63.65 °C [134], so depending on what temperature the cell is, we should make use of the appropriate equation. For instance, for the particular case that our cell is heated at 84 °C we should make use of equation B.3.

After calculating p , it is trivial to calculate \mathcal{N} ,

$$\mathcal{N} = \frac{p}{k_B T} \quad . \quad (\text{B.4})$$

Thus, for the two isotopes in the cell, we find number densities as,

$$\mathcal{N}_{39} = 0.933 \times \mathcal{N} \quad (\text{B.5})$$

$$\mathcal{N}_{41} = 0.067 \times \mathcal{N} \quad . \quad (\text{B.6})$$

Bibliography

- [1] G. Leuchs and M. Sondermann, *Light–matter interaction in free space*, Journal of modern optics **60** (1), 36–42 (2013).
- [2] M. Stobińska, G. Alber and G. Leuchs, *Perfect excitation of a matter qubit by a single photon in free space*, EPL (Europhysics Letters) **86** (1), 14007 (2009).
- [3] D. Csontos, *Light-matter interaction: Perfect reflections*, Nature Physics **4** (12), 908–908 (2008).
- [4] C. Sheppard and P. Török, *Electromagnetic field in the focal region of an electric dipole wave*, Optik-Stuttgart **104** 175–177 (1997).
- [5] G. Zumofen, N. Mojarad, V. Sandoghdar and M. Agio, *Perfect reflection of light by an oscillating dipole*, Physical Review Letters **101** (18), 180404 (2008).
- [6] M. K. Tey, Z. Chen, S. A. Aljunid, B. Chng, F. Huber, G. Maslennikov and C. Kurtsiefer, *Strong interaction between light and a single trapped atom without the need for a cavity*, Nature Physics **4** (12), 924–927 (2008).
- [7] M. Fischer, M. Bader, R. Maiwald, A. Golla, M. Sondermann and G. Leuchs, *Efficient saturation of an ion in free space*, Applied Physics B **117** (3), 797–801 (2014).
- [8] H. Mabuchi and A. Doherty, *Cavity quantum electrodynamics: coherence in context*, Science **298** (5597), 1372–1377 (2002).

- [9] A. Reiserer and G. Rempe, *Cavity-based quantum networks with single atoms and optical photons*, *Reviews of Modern Physics* **87** (4), 1379 (2015).
- [10] P. A. Dirac, *The quantum theory of the emission and absorption of radiation*, in *Proceedings of the Royal Society of London A: Mathematical, Physical and Engineering Sciences*, vol. 114, 243–265, The Royal Society (1927).
- [11] E. Fermi, *Nuclear physics: a course given by Enrico Fermi at the University of Chicago*. University of Chicago Press (1950).
- [12] R. H. Dicke, *Coherence in Spontaneous Radiation Processes*, *Physical Review* **93** 99–110 (1954).
- [13] M. Tavis and F. W. Cummings, *Approximate Solutions for an N -Molecule-Radiation-Field Hamiltonian*, *Physical Reviews* **188** 692–695 (1969).
- [14] M. Raizen, R. Thompson, R. Brecha, H. Kimble and H. Carmichael, *Normal-mode splitting and linewidth averaging for two-state atoms in an optical cavity*, *Physical Review Letters* **63** (3), 240 (1989).
- [15] C. von Cube, S. Slama, M. Kohler, C. Zimmermann and P. W. Courteille, *Creating and probing long-range order in atomic clouds*, *Fortschritte der Physik* **54** (8-10), 726–745 (2006).
- [16] H. Ritsch, P. Domokos, F. Brennecke and T. Esslinger, *Cold atoms in cavity-generated dynamical optical potentials*, *Reviews of Modern Physics* **85** (2), 553 (2013).
- [17] J. Zhang, X. Wei, G. Hernandez and Y. Zhu, *White-light cavity based on coherent raman scattering via normal modes of a coupled cavity-and-atom system*, *Physical Review A* **81** (3), 033804 (2010).
- [18] A. Wickenbrock, M. Hemmerling, G. R. Robb, C. Emary and F. Renzoni,

- Collective strong coupling in multimode cavity QED*, Physical Review A **87** (4), 043817 (2013).
- [19] K. J. Arnold, M. P. Baden and M. D. Barrett, *Collective cavity quantum electrodynamics with multiple atomic levels*, Physical Review A **84** (3), 033843 (2011).
- [20] E. E. Mikhailov, V. A. Sautenkov, I. Novikova and G. R. Welch, *Large negative and positive delay of optical pulses in coherently prepared dense Rb vapor with buffer gas*, Physical Review A **69** (6), 063808 (2004).
- [21] A. Dogariu, A. Kuzmich and L. Wang, *Transparent anomalous dispersion and superluminal light-pulse propagation at a negative group velocity*, Physical Review A **63** (5), 053806 (2001).
- [22] S. E. Harris, J. Field and A. Imamoglu, *Nonlinear optical processes using electromagnetically induced transparency*, Physical Review Letters **64** (10), 1107 (1990).
- [23] L. V. Hau, S. E. Harris, Z. Dutton and C. H. Behroozi, *Light speed reduction to 17 metres per second in an ultracold atomic gas*, Nature **397** (6720), 594 (1999).
- [24] D. Budker, D. Kimball, S. Rochester and V. Yashchuk, *Nonlinear magneto-optics and reduced group velocity of light in atomic vapor with slow ground state relaxation*, Physical Review Letters **83** (9), 1767 (1999).
- [25] M. Mücke, E. Figueroa, J. Bochmann, C. Hahn, K. Murr, S. Ritter, C. J. Villas-Boas and G. Rempe, *Electromagnetically induced transparency with single atoms in a cavity*, Nature **465** (7299), 755–758 (2010).
- [26] T. Kampschulte, W. Alt, S. Brakhane, M. Eckstein, R. Reimann, A. Widera and D. Meschede, *Optical control of the refractive index of a single atom*, Physical Review Letters **105** (15), 153603 (2010).

- [27] M. Lukin, *Colloquium: Trapping and manipulating photon states in atomic ensembles*, Reviews of Modern Physics **75** (2), 457 (2003).
- [28] L. Wang, A. Kuzmich and A. Dogariu, *Gain-assisted superluminal light propagation*, Nature **406** 277–279 (2000).
- [29] R. W. Boyd, *Slow and fast light: fundamentals and applications*, Journal of Modern Optics **56** (18-19), 1908–1915 (2009).
- [30] M. D. Lukin, M. Fleischhauer, M. O. Scully and V. L. Velichansky, *Intracavity electromagnetically induced transparency*, Optics Letters **23** (4), 295–297 (1998).
- [31] Z. Shi, R. W. Boyd, R. M. Camacho, P. K. Vudyasetu and J. C. Howell, *Slow-light Fourier transform interferometer*, Physical Review Letters **99** (24), 240801 (2007).
- [32] Z. Shi and R. W. Boyd, *Slow-light interferometry: practical limitations to spectroscopic performance*, JOSA B **25** (12), C136–C143 (2008).
- [33] M. Shahriar, G. Pati, R. Tripathi, V. Gopal, M. Messall and K. Salit, *Ultrahigh enhancement in absolute and relative rotation sensing using fast and slow light*, Physical Review A **75** (5), 053807 (2007).
- [34] F. Brennecke, T. Donner, S. Ritter, T. Bourdel, M. Kohl and T. Esslinger, *Cavity QED with a Bose-Einstein condensate*, Nature **450** (7167), 268–271 (2007).
- [35] T. Aoki, A. Parkins, D. Alton, C. Regal, B. Dayan, E. Ostby, K. J. Vahala and H. Kimble, *Efficient routing of single photons by one atom and a microtoroidal cavity*, Physical Review Letters **102** (8), 083601 (2009).
- [36] X.-H. Bao, A. Reingruber, P. Dietrich, J. Rui, A. Dück, T. Strassel, L. Li, N.-L. Liu, B. Zhao and J.-W. Pan, *Efficient and long-lived quantum memory with cold atoms inside a ring cavity*, Nature Physics **8** (7), 517–521 (2012).

- [37] H. Wang, D. Goorskey, W. Burkett and M. Xiao, *Cavity-linewidth narrowing by means of electromagnetically induced transparency*, Optics Letters **25** (23), 1732–1734 (2000).
- [38] D. Goorskey, H. Wang, W. Burkett and M. Xiao, *Effects of a highly dispersive atomic medium inside an optical ring cavity*, Journal of Modern Optics **49** (1-2), 305–317 (2002).
- [39] H. Yum, M. Salit, J. Yablon, K. Salit, Y. Wang and M. Shahriar, *Superluminal ring laser for hypersensitive sensing*, Optics Express **18** (17), 17658–17665 (2010).
- [40] J. Scheuer and S. M. Shahriar, *Lasing dynamics of super and sub luminal lasers*, Optics Express **23** (25), 32350–32366 (2015).
- [41] K. U. Schreiber and J.-P. R. Wells, *Invited review article: Large ring lasers for rotation sensing*, Review of Scientific Instruments **84** (4), 041101 (2013).
- [42] A. L. Schawlow and C. H. Townes, *Infrared and optical masers*, Physical Review **112** (6), 1940 (1958).
- [43] S. Kuppens, M. Van Exter and J. Woerdman, *Quantum-limited linewidth of a bad-cavity laser*, Physical Review Letters **72** (24), 3815 (1994).
- [44] J. G. Bohnet, Z. Chen, J. M. Weiner, D. Meiser, M. J. Holland and J. K. Thompson, *A steady-state superradiant laser with less than one intracavity photon*, Nature **484** (7392), 78 (2012).
- [45] M. A. Norcia and J. K. Thompson, *Cold-strontium laser in the superradiant crossover regime*, Physical Review X **6** (1), 011025 (2016).
- [46] J. Chen, *Active optical clock*, Chinese Science Bulletin **54** (3), 348–352 (2009).
- [47] R. Culver, A. Lampis, B. Megyeri, K. Pahwa, L. Mudarikwa, M. Holynski, P. W. Courteille and J. Goldwin, *Collective strong coupling of cold potassium atoms in a ring cavity*, New Journal of Physics **18** (11), 113043 (2016).

- [48] S. Gozzini, S. Cartaleva, A. Lucchesini, C. Marinelli, L. Marmugi, D. Slavov and T. Karaulanov, *Coherent population trapping and strong electromagnetically induced transparency resonances on the line of potassium*, The European Physical Journal D-Atomic, Molecular, Optical and Plasma Physics **53** (2), 153–161 (2009).
- [49] K. Nasyrov, S. Gozzini, A. Lucchesini, C. Marinelli, S. Gateva, S. Cartaleva and L. Marmugi, *Antirelaxation coatings in coherent spectroscopy: Theoretical investigation and experimental test*, Physical Review A **92** (4), 043803 (2015).
- [50] W. Xu and B. DeMarco, *Velocity-selective electromagnetically-induced-transparency measurements of potassium Rydberg states*, Physical Review A **93** (1), 011801 (2016).
- [51] T. Kishimoto, J. Kobayashi, K. Noda, K. Aikawa, M. Ueda and S. Inouye, *Direct evaporative cooling of $K\ 41$ into a Bose-Einstein condensate*, Physical Review A **79** (3), 031602 (2009).
- [52] K. Birnbaum, A. Parkins and H. Kimble, *Cavity QED with multiple hyperfine levels*, Physical Review A **74** (6), 063802 (2006).
- [53] M. Fox, *Quantum optics: an introduction*, vol. 15. OUP Oxford (2006).
- [54] E. T. Jaynes and F. W. Cummings, *Comparison of quantum and semiclassical radiation theories with application to the beam maser*, Proceedings of the IEEE **51** (1), 89–109 (1963).
- [55] M. O. Scully and M. S. Zubairy, *Quantum Optics*, (1999).
- [56] D. F. Walls and G. J. Milburn, *Quantum Optics*. Springer Science & Business Media (2007).
- [57] C. Gerry and P. Knight, *Introductory Quantum Optics*. Cambridge University Press (2005).

- [58] P. Meystre and M. Sargent, *Elements of Quantum Optics*. Springer Science & Business Media (2013).
- [59] C. Cohen-Tannoudji, B. Diu and F. Laloe, *Quantum Mechanics, Volume 1*. Wiley (1977).
- [60] R. Brecha, L. Orozco, M. Raizen, M. Xiao and H. Kimble, *Observation of oscillatory energy exchange in a coupled-atom-cavity system*, JOSA B **12** (12), 2329–2339 (1995).
- [61] A. Kuhn and G. Rempe, *Optical cavity QED: Fundamentals and application as a single-photon light source*, in *International School of Physics " Enrico Fermi" Course CXLVIII*, 37–66, IOS Press (2002).
- [62] E. M. Purcell, *Spontaneous emission probabilities at radio frequencies*, in *Confined Electrons and Photons*, 839–839. Springer (1995).
- [63] H. Tanji-Suzuki, I. D. Leroux, M. H. Schleier-Smith, M. Cetina, A. T. Grier, J. Simon and V. Vuletic, *Chapter 4-interaction between atomic ensembles and optical resonators: Classical description*, *Advances in Atomic, Molecular, and Optical Physics* **60** 201–237.
- [64] H. J. Kimble, *Strong interactions of single atoms and photons in cavity QED*, *Physica Scripta* **1998** (T76), 127 (1998).
- [65] Y.-H. Lien, G. Barontini, M. Scheucher, M. Mergenthaler, J. Goldwin and E. Hinds, *Observing coherence effects in an overdamped quantum system*, *Nature Communications* **7** (2016).
- [66] B. M. Garraway, *The Dicke model in quantum optics: Dicke model revisited*, *Philosophical Transactions of the Royal Society of London A: Mathematical, Physical and Engineering Sciences* **369** (1939), 1137–1155 (2011).

- [67] R. L. Smith, *The velocities of light*, American Journal of Physics **38** (8), 978–984 (1970).
- [68] L. Brillouin, *Wave propagation and group velocity*, vol. 8. Academic Press (2013).
- [69] D. A. Steck, *Classical and Modern Optics*. <http://steck.us/teaching>. (revision 1.4, 3 May 2008).
- [70] M. D. Stenner, D. J. Gauthier and M. A. Neifeld, *The speed of information in a 'fast-light' optical medium*, Nature **425** (6959), 695 (2003).
- [71] R. P. Feynman, *Feynman lectures on physics. Volume 2: Mainly electromagnetism and matter*, Reading, Ma.: Addison-Wesley, 1964, edited by Feynman, Richard P.; Leighton, Robert B.; Sands, Matthew (1964).
- [72] J. O. Weatherall, *Quantum control of linear susceptibility in five level atoms via dressed interacting ground states, with a focus on group velocity control*. Ph.D. thesis, Stevens Institute of Technology (2009).
- [73] W. W. Erickson, *Electromagnetically Induced Transparency*. Ph.D. thesis, Reed College (2012).
- [74] M. Fleischhauer, A. Imamoglu and J. P. Marangos, *Electromagnetically induced transparency: Optics in coherent media*, Reviews of Modern Physics **77** (2), 633 (2005).
- [75] M. Fleischhauer and M. D. Lukin, *Dark-state polaritons in electromagnetically induced transparency*, Physical Review Letters **84** (22), 5094 (2000).
- [76] H. Carmichael, *An open systems approach to quantum optics: lectures presented at the Université Libre de Bruxelles, October 28 to November 4, 1991*, vol. 18. Springer Science & Business Media (2009).

- [77] C. A. Gonano, R. E. Zich and M. Mussetta, *Definition for Polarization P and Magnetization M Fully Consistent with Maxwell's Equations*, Progress In Electromagnetics Research B **64** 83–101 (2015).
- [78] S. H. Autler and C. H. Townes, *Stark effect in rapidly varying fields*, Physical Review **100** (2), 703 (1955).
- [79] J. Johansson, P. Nation and F. Nori, *QuTiP: An open-source Python framework for the dynamics of open quantum systems*, Computer Physics Communications **183** (8), 1760–1772 (2012).
- [80] R. Culver, *Collective strong coupling of cold potassium atoms in an optical ring cavity*. Ph.D. thesis, University of Birmingham (2017).
- [81] L. Mudarikwa, *Cold atoms in a ring cavity*. Ph.D. thesis, University of Birmingham (2015).
- [82] K. Pahwa, *Magneto optical trapping of potassium-39 in a ring cavity*. Ph.D. thesis, University of Birmingham (2014).
- [83] S. Chapman and T. G. Cowling, *The mathematical theory of non-uniform gases: an account of the kinetic theory of viscosity, thermal conduction and diffusion in gases*. Cambridge University Press (1970).
- [84] S. B. Papp, *Experiments with a two-species Bose-Einstein condensate utilizing widely tunable interparticle interactions*. Ph.D. thesis (2001).
- [85] K. Pahwa, L. Mudarikwa and J. Goldwin, *Polarization spectroscopy and magnetically-induced dichroism of the potassium $D2$ lines*, Optics Express **20** (16), 17456–17466 (2012).
- [86] H. Wang, P. Gould and W. Stwalley, *Long-range interaction of $39\text{ K } (4s)+39\text{ K } (4p)$ asymptote by photoassociative spectroscopy*, in *The Journal of Chemical Physics*, vol. 106, 7899–7912 (1997).

- [87] G. Ritt, G. Cennini, C. Geckeler and M. Weitz, *Laser frequency offset locking using a side of filter technique*, Applied Physics B: Lasers and Optics **79** (3), 363–365 (2004).
- [88] T. Udem, J. Reichert, T. Hänsch and M. Kourogi, *Absolute optical frequency measurement of the cesium D2 line*, Physical Review A **62** (3), 031801 (2000).
- [89] R. Drever, J. L. Hall, F. Kowalski, J. Hough, G. Ford, A. Munley and H. Ward, *Laser phase and frequency stabilization using an optical resonator*, Applied Physics B **31** (2), 97–105 (1983).
- [90] E. D. Black, *An introduction to Pound–Drever–Hall laser frequency stabilization*, American Journal of Physics **69** (1), 79–87 (2001).
- [91] L. Mudarikwa, K. Pahwa and J. Goldwin, *Sub-Doppler modulation spectroscopy of potassium for laser stabilization*, Journal of Physics B: Atomic, Molecular and Optical Physics **45** (6), 065002 (2012).
- [92] D. Budker, S. M. Rochester and V. V. Yashchuk, *Obtaining frequency markers of variable separation with a spherical mirror Fabry-Perot interferometer*, Review of Scientific Instruments **71** (8), 2984–2987 (2000).
- [93] S. Falke, E. Tiemann, C. Lisdat, H. Schnatz and G. Grosche, *Transition frequencies of the D lines of ^{39}K , ^{40}K , and ^{41}K measured with a femtosecond laser frequency comb*, Physical Review A **74** 032503 (2006).
- [94] W. Nagourney, *Quantum Electronics for Atomic Physics*. Oxford University Press (2010).
- [95] S. Zhang, J. Chen, C. Liu, S. Zhou, M. Loy, G. K. L. Wong and S. Du, *A dark-line two-dimensional magneto-optical trap of 85Rb atoms with high optical depth*, Review of Scientific Instruments **83** (7), 073102 (2012).

- [96] A. Lampis, R. Culver, B. Megyeri and J. Goldwin, *Coherent control of group index and magneto-optical anisotropy in a multilevel atomic vapor*, Optics Express **24** (14), 15494–15505 (2016).
- [97] M. Bason et al., *Coherent atom-light interactions in multi-level systems*. Ph.D. thesis, Durham University (2009).
- [98] C. J. Foot, *Atomic physics*, vol. 7. Oxford University Press (2005).
- [99] J. Thomas and W. Quivers Jr, *Transit-time effects in optically pumped coupled three-level systems*, Physical Review A **22** (5), 2115 (1980).
- [100] E. Figueroa, F. Vewinger, J. Appel and A. Lvovsky, *Decoherence of electromagnetically induced transparency in atomic vapor*, Optics Letters **31** (17), 2625–2627 (2006).
- [101] K. A. Whittaker, J. Keaveney, I. G. Hughes and C. S. Adams, *Hilbert transform: Applications to atomic spectra*, Physical Review A **91** (3), 032513 (2015).
- [102] O. Schmidt, R. Wynands, Z. Hussein and D. Meschede, *Steep dispersion and group velocity below $c/3000$ in coherent population trapping*, Physical Review A **53** (1), R27 (1996).
- [103] R. Wynands, A. Nagel, S. Brandt, D. Meschede and A. Weis, *Selection rules and line strengths of Zeeman-split dark resonances*, Physical Review A **58** (1), 196 (1998).
- [104] A. Sargsyan, P. Petrov, T. Vartanyan and D. Sarkisyan, *Electromagnetically induced transparency in potassium vapors: features and restrictions*, Optics and Spectroscopy **120** (3), 339–344 (2016).
- [105] X.-G. Wei, J.-H. Wu, G.-X. Sun, Z. Shao, Z.-H. Kang, Y. Jiang and J.-Y. Gao, *Splitting of an electromagnetically induced transparency window of rubidium atoms in a static magnetic field*, Physical Review A **72** (2), 023806 (2005).

- [106] S. Iftiqar and V. Natarajan, *Line narrowing of electromagnetically induced transparency in Rb with a longitudinal magnetic field*, Physical Review A **79** (1), 013808 (2009).
- [107] D. Budker, W. Gawlik, D. Kimball, S. Rochester, V. Yashchuk and A. Weis, *Resonant nonlinear magneto-optical effects in atoms*, Reviews of Modern Physics **74** (4), 1153 (2002).
- [108] S. Franke-Arnold, M. Arndt and A. Zeilinger, *Magneto-optical effects with cold lithium atoms*, Journal of Physics B: Atomic, Molecular and Optical Physics **34** (12), 2527 (2001).
- [109] J. M. Choi, J. M. Kim, Q.-H. Park and D. Cho, *Optically induced Faraday effect in a Λ configuration of spin-polarized cold cesium atoms*, Physical Review A **75** (1), 013815 (2007).
- [110] A. Wojciechowski, E. Corsini, J. Zachorowski and W. Gawlik, *Nonlinear Faraday rotation and detection of superposition states in cold atoms*, Physical Review A **81** (5), 053420 (2010).
- [111] B. Wang, S. Li, J. Ma, H. Wang, K. Peng and M. Xiao, *Controlling the polarization rotation of an optical field via asymmetry in electromagnetically induced transparency*, Physical Review A **73** (5), 051801 (2006).
- [112] N. Hombo, S. Taniguchi, S. Sugimura, K. Fujita and M. Mitsunaga, *Electromagnetically induced polarization rotation in Na vapor*, JOSA B **29** (7), 1717–1721 (2012).
- [113] Y.-C. Chen, C.-W. Lin and A. Y. Ite, *Roles of degenerate Zeeman levels in electromagnetically induced transparency*, Physical Review A **61** (5), 053805 (2000).

- [114] K. Li, L. Deng and M. G. Payne, *Realization of a single and closed Λ -system in a room-temperature three-level coherently prepared resonant medium with narrow D 1 hyperfine splittings*, Applied Physics Letters **95** (22), 221103 (2009).
- [115] O. Mishina, M. Scherman, P. Lombardi, J. Ortalo, D. Felinto, A. Sheremet, A. Bramati, D. Kupriyanov, J. Laurat and E. Giacobino, *Electromagnetically induced transparency in an inhomogeneously broadened Λ transition with multiple excited levels*, Physical Review A **83** (5), 053809 (2011).
- [116] T. W. Hänsch and A. L. Schawlow, *Cooling of gases by laser radiation*, Optics Communications **13** (1), 68–69 (1975).
- [117] D. J. Wineland and W. M. Itano, *Laser cooling of atoms*, Physical Review A **20** (4), 1521 (1979).
- [118] J. Prodan, A. Migdall, W. D. Phillips, I. So, H. Metcalf and J. Dalibard, *Stopping atoms with laser light*, Physical Review Letters **54** (10), 992 (1985).
- [119] V. Balykin, V. Letokhov, V. Minogin, Y. V. Rozhdestvensky and A. Sidorov, *Radiative collimation of atomic beams through two-dimensional cooling of atoms by laser-radiation pressure*, JOSA B **2** (11), 1776–1783 (1985).
- [120] S. Chu, L. Hollberg, J. E. Bjorkholm, A. Cable and A. Ashkin, *Three-dimensional viscous confinement and cooling of atoms by resonance radiation pressure*, Physical Review Letters **55** (1), 48 (1985).
- [121] E. Raab, M. Prentiss, A. Cable, S. Chu and D. E. Pritchard, *Trapping of neutral sodium atoms with radiation pressure*, Physical Review Letters **59** (23), 2631 (1987).
- [122] H. J. Metcalf and P. van der Straten, *Laser cooling and trapping of atoms*, JOSA B **20** (5), 887–908 (2003).

- [123] P. D. Lett, W. D. Phillips, S. Rolston, C. E. Tanner, R. Watts and C. Westbrook, *Optical molasses*, JOSA B **6** (11), 2084–2107 (1989).
- [124] P. D. Lett, R. N. Watts, C. I. Westbrook, W. D. Phillips, P. L. Gould and H. J. Metcalf, *Observation of atoms laser cooled below the Doppler limit*, Physical Review Letters **61** (2), 169 (1988).
- [125] J. Dalibard and C. Cohen-Tannoudji, *Laser cooling below the Doppler limit by polarization gradients: simple theoretical models*, JOSA B **6** (11), 2023–2045 (1989).
- [126] R. S. Williamson III, *Magneto-optical trapping of potassium isotopes*. Ph.D. thesis, University of Wisconsin–Madison (1997).
- [127] L. Russell, R. Kumar, V. Tiwari and S. N. Chormaic, *Measurements on release–recapture of cold 85 Rb atoms using an optical nanofibre in a magneto-optical trap*, Optics Communications **309** 313–317 (2013).
- [128] P. D. Lett, W. D. Phillips, S. Rolston, C. E. Tanner, R. Watts and C. Westbrook, *Optical molasses*, JOSA B **6** (11), 2084–2107 (1989).
- [129] K. J. Weatherill, *A CO_2 laser lattice experiment for cold atoms*. Ph.D. thesis, Durham University (2007).
- [130] D. Nath, R. K. Easwaran, G. Rajalakshmi and C. Unnikrishnan, *Accelerated thermalization of $39K$ atoms in a magnetic trap with superimposed optical potential*, Journal of Physics B: Atomic, Molecular and Optical Physics **46** (15), 155303 (2013).
- [131] G. Salomon, L. Fouché, P. Wang, A. Aspect, P. Bouyer and T. Bourdel, *Gray-molasses cooling of $39K$ to a high phase-space density*, EPL (Europhysics Letters) **104** (6), 63002 (2014).

- [132] W. Ketterle, K. B. Davis, M. A. Joffe, A. Martin and D. E. Pritchard, *High densities of cold atoms in a dark spontaneous-force optical trap*, Physical Review Letters **70** (15), 2253 (1993).
- [133] G. D. McDonald, *Detecting Atomic Shot Noise On Ultra-cold Atom Clouds*. Ph.D. thesis, Australian National University (2009).
- [134] T. Tiecke, *Properties of potassium*, University of Amsterdam, The Netherlands, Thesis 12–14 (2010).
- [135] C. Fort, A. Bambini, L. Cacciapuoti, F. Cataliotti, M. Prevedelli, G. Tino and M. Inguscio, *Cooling mechanisms in potassium magneto-optical traps*, The European Physical Journal D-Atomic, Molecular, Optical and Plasma Physics **3** (2), 113–118 (1998).
- [136] M. Landini, S. Roy, L. Carcagní, D. Trypogeorgos, M. Fattori, M. Inguscio and G. Modugno, *Sub-Doppler laser cooling of potassium atoms*, Physical Review A **84** (4), 043432 (2011).
- [137] V. Gokhroo, G. Rajalakshmi, R. K. Easwaran and C. Unnikrishnan, *Sub-Doppler deep-cooled bosonic and fermionic isotopes of potassium in a compact 2D+–3D MOT set-up*, Journal of Physics B: Atomic, Molecular and Optical Physics **44** (11), 115307 (2011).
- [138] B. S. Marangoni, C. R. Menegatti and L. G. Marcassa, *Loading a 39K crossed optical dipole trap from a magneto-optical trap*, Journal of Physics B: Atomic, Molecular and Optical Physics **45** (17), 175301 (2012).
- [139] H. J. Metcalf and P. Van der Straten, *Laser cooling and trapping*. Springer Science & Business Media (2012).
- [140] P. P. Della, C. Emily and S. J. Helier, *Alkali metal generation and gas evolution*

- from alkali metal dispensers. https://www.saesgetters.com/sites/default/files/AMD%20Generation%20and%20Gas%20Evolution_0.pdf. Technical report.
- [141] R. K. Hanley, P. D. Gregory, I. G. Hughes and S. L. Cornish, *Absolute absorption on the potassium D lines: theory and experiment*, Journal of Physics B: Atomic, Molecular and Optical Physics **48** (19), 195004 (2015).
- [142] C. Alcock, V. Itkin and M. Horrigan, *Vapour pressure equations for the metallic elements: 298–2500K*, Canadian Metallurgical Quarterly **23** (3), 309–313 (1984).
- [143] H. J. Carmichael and B. C. Sanders, *Multiatom effects in cavity QED with atomic beams*, Physical Review A **60** 2497–2504 (1999).
- [144] G. S. Agarwal, *Vacuum-Field Rabi Splittings in Microwave Absorption by Rydberg Atoms in a Cavity*, Physical Review Letters **53** 1732–1734 (1984).
- [145] A. Lampis, R. Culver, B. Megyeri, G. Harvey and J. Goldwin, *Strong Light-Matter Coupling with Cold Potassium Atoms in a Ring Cavity*, in *Quantum Information and Measurement (QIM) 2017*, QT2A.1. Optical Society of America (2017).
- [146] V. Tiwari, S. Singh, H. Rawat, M. P. Singh and S. Mehendale, *Electromagnetically induced transparency in cold 85Rb atoms trapped in the ground hyperfine $F=2$ state*, Journal of Physics B: Atomic, Molecular and Optical Physics **43** (9), 095503 (2010).
- [147] P. M. Anisimov, J. P. Dowling and B. C. Sanders, *Objectively Discerning Autler-Townes Splitting from Electromagnetically Induced Transparency*, Physical Review Letters **107** 163604 (2011).
- [148] D. A. Steck, *Rubidium 87 D Line Data*. <http://steck.us/alkalidata>. (revision 2.1.5, 13 January 2015).
- [149] B. Megyeri, A. Lampis, G. Harvie, R. Culver and J. Goldwin, *Why material slow*

light does not improve cavity-enhanced atom detection, Journal of Modern Optics **65** (2), 185–191 (2017).

- [150] T. Lauprêtre, C. Proux, R. Ghosh, S. Schwartz, F. Goldfarb and F. Bretenaker, *Photon lifetime in a cavity containing a slow-light medium*, Optics Letters **36** (9), 1551–1553 (2011).